DESIGN OF TEM MODE AND TE MODE FILTERS USING 2-D AND 3-D FIELD SIMULATORS

A Thesis

Submitted to the College of Graduate Studies and Research

In Partial Fulfillment of the Requirements

For the Degree of

Master of Science

In the Department of Electrical Engineering

University of Saskatchewan

Saskatoon

By

Shi Yin

May 2000

PERMISSION TO USE

In presenting this thesis in partial fulfillment of the requirements for a Postgraduate degree from the University of Saskatchewan, I agree that libraries of this university may make it freely available for inspection. I further agree that permission for copying of this thesis in any manner, in whole or in part, for scholarly purposes may be granted by the professor or professors who supervised my thesis work or, in their absence, by the Head of Department or the Dean of the College in which my thesis work was done. It is understood that any copying or publication or use of this thesis or part thereof for financial gain shall be given to me and to the University of Saskatchewan in any scholarly use which may be made of any material in my thesis.

Request for permission to copy or to make other use of material in this thesis in whole or part should be addressed to:

Head of the Department of Electrical Engineering
University of Saskatchewan
57 Campus Drive
Saskatoon, Saskatchewan, Canada
S7N 5A9

ABSTRACT

Due to the explosive growth in modern wireless communication technology and satellite communication systems, the demand for research in microwave filter engineering has increased dramatically in the recent past. Traditionally, microwave filters were designed empirically using approximate models and needed significant post-production tuning. Over the last two decades, a number of numerical methods have been generated for microwave applications. This thesis presents the generalized filter design method of Levy & Rhodes that is based on two dimensional and three dimensional electromagnetic analysis and discontinuity modeling using commercially available full-wave electromagnetic simulators. It shows how to design waveguide filters accurately, using modern electromagnetic field solvers based on the Finite Element Method, the Finite Difference Method and the Transmission Line Matrix analysis method. This is the first time that some design curves and equations are presented for ceramic block slab-line filters and post and iris coupled waveguide filters. This thesis also demonstrates the generality of the method. It can be applied to many other types of microwave lowpass and bandpass filters.

ACKNOWLEDGEMENT

The author would like to express his sincere gratitude to his supervisor, Dr. Protap Pramanick, for his guidance, encouragement and financial support during the course of this work. His advice and assistance in the preparation of this thesis is highly appreciated.

The author expresses his sincere gratitude to Motorola, USA, for financial support and experimental results. The author is also grateful to Microwave Development Co., Salem, NH, USA, for experimental results.

Finally, the author would like to thank his family and all his friends for their patience, encouragement and moral support.

DEDICATION

This thesis is dedicated to the author's wife, Lei Shen, and their daughter, Yue Yin, for their love, care, patience and constant support.

LIST OF TABLES

LIST OF FIGURES

LIST OF SYMBOLS AND ABBREVIATIONS

1. Greek and non-Latin Symbols

α	Scaling parameter
β_n	Propagation phase constant
ε	Dielectric permittivity of the medium
ε_0	Permittivity of free space
ε_p	Factor determining the passband ripple level of the filter
ε_r	Relative dielectric constant
$\varepsilon_{r,e}$	Effective dielectric constant of even mode
$\varepsilon_{r,o}$	Effective dielectric constant of odd mode
$\varepsilon_{r,eff}$	Effective dielectric constant
η	Free space wave impedance
λ	Wavelength of electromagnetic radiation
λ_0	Free space wavelength
λ_c	Cut-off wavelength
λ_g	waveguide wavelength
λ_{g0}	Mid-band guide wavelength
λ_{gH}	Guide wavelength at the upper cut-off frequency
λ_{gL}	Guide wavelength at the lower cut-off frequency
θ_n	Electrical phase shift
ρ_v	Volume charge density

Δf	Ripple bandwidth
Δf_i	Isolation bandwidth
Φ_1	Potential on one of the rods
Φ_2	Potential on another of the rods
∇	Del operator

2. Latin Symbols and Abbreviations

2-D	Two dimensional
3-D	Three dimensional
a	Waveguide width
b	Waveguide height
c	Speed of light
dB	Decibel
f	Frequency of electromagnetic wave
f_0	Central frequency
$f_{0,e}$	Resonant frequency of the even mode
$f_{0,o}$	Resonant frequency of the odd mode
g_n	Low-pass prototype element values
$k'_{n,n+1}$	Impedance inverter value
l_n	Distance between two terminal planes
m	Integer determining the propagation mode in waveguide
n	Integer determining the propagation mode in waveguide
r_i	Radius of the inner conductor
r_o	Radius of the outer conductor
t_n	Terminal plane
v^a	Velocity of light in free space
A_m	Amplitude of the ripple

C	Capacitance
C_e	Capacitance of even mode
C_e^a	Capacitance of even mode when dielectrics are replaced by free space
C_g	Self capacitance
C_{in}	Input capacitive coupling
C_m	Mutual capacitance
C_o	Capacitance of odd mode
C_o^a	Capacitance of odd mode when dielectrics are replaced by free space
C_{out}	Output capacitive coupling
D	Electric flux density
E	Electric field intensity
EM	Electromagnetics
FDM	Finite Difference Method
FEM	Finite Element Method
GHz	10^9 Hz
IL	Insertion loss
IL_0	Insertion loss at central frequency
J	Admittance inverter value
$J_{n,n+1}$	Unnormalized J-inverters
$\overline{J}_{n,n+1}$	Normalized J-inverters
K	Impedance inverter value
K^c	Coupling coefficient
$K_{n,n+1}$	Normalized K-inverter value
LA	Stop band isolation
L_{ak}	Inductance
L_{ij}	Coupling inductance
MHz	10^6 Hz
N	Order of the filter

P_A	Power admitted to the filter
P_{in}	Incident power from the generator
P_L	Power transmitted to the load
P_R	Power reflected towards the generator
PDE	Partial differential equation
Q	Unloaded quality factor
R_a	Resistance at one end
R_b	Resistance at another end
RL	Return loss
S_{mn}	Elements of *S*-parameter
TE	Transverse Electric
TM	Transverse Magnetic
TEM	Transverse Electro-Magnetic
TLM	Transmission Line Matrix Method
V	Electric potential
W_e	Energy per unit length
$X_{j,j+1}$	Shunt reactance
Y_a	Admittance at generator end
Y_b	Admittance at load end
Z_0	Characteristic impedance
Z_a	Impedance at generator end
Z_b	Impedance at load end
Z_e	Characteristic impedance of even modes
Z_o	Characteristic impedance of odd modes

Chapter 1 Introduction

Microwaves have been a significant part of our lives. Television programs are transmitted by satellites using microwaves. Telephone and data signals are transmitted by microwave relay. Cellular phone communication is by microwave. Missiles, airplanes and ships are guided and controlled by microwave radar and navigation systems. Microwaves are also used to cook food and treat cancer patients.

The term *microwaves* is used to describe electromagnetic waves with wavelengths ranging from 1 *cm* to 1 *m*. The corresponding frequency range is 0.3 *GHz* to 30 *GHz*. At these wavelengths, the components of conventional electronic circuits tend to behave like individual antenna, dissipating their electrical signals as radiation. Different techniques are necessary to handle electrical signals in the microwave frequency range, leading to different techniques of analysis. The short wavelength and fairly wide frequency spectrum give microwaves obvious advantages for their application, especially in communications system.

In all modern communication systems, small size and low cost radio equipment are required. Transmitting and receiving filters in a radio equipment occupy considerable amount of volume of the equipment. This research is concerned with the design of microwave filters using modern commercially available simulation tools.

In the following sections, a number of useful concepts related to microwave filters are introduced.

1.1 Transmission lines and waveguides

Microwaves propagate either in open space such as in radar and satellite communications, or as a guided wave in a transmission line or a waveguide. The plane wave, which is the fundamental form of wave propagating in a uniform medium of infinite extent, cannot exist when there are any boundaries to space. In practice, at microwave frequencies these conditions are not even approximately true and the effect of boundaries has to be considered. It is often necessary to control the electromagnetic radiation and to channel it from one point to another without allowing it to escape as radiation into the surrounding space. It is found that under certain conditions the electromagnetic radiation will propagate freely along the inside of a hollow metal pipe. The pipe used for this purpose is called a waveguide. Microwaves propagate in a waveguide due to multiple reflections from the inner walls of the waveguide. A dielectric is sometimes used in between conducting walls as either a support or as a method of improving the propagation.

Waves propagate along a waveguide in a series of modes, which are designated as TEM (Transverse Electro-Magnetic), TM (Transverse Magnetic), and TE (Transverse Electric) modes. TEM modes exist at all frequencies starting from zero. TM and TE modes have cut-off frequencies below which they cannot travel along the waveguide. In certain types of microwave waveguide, the TEM mode cannot exist so that there is a cutoff frequency below which no power will propagate.

1.1.1 Coaxial cable

Coaxial cable is used for interconnecting microwave components at lower frequencies, usually below 20 *GHz*. In Figure 1.1, r_i is the radius of the inner conductor and r_o is the radius of the outer conductor. Coaxial cable can support TEM mode. Its characteristic impedance is

$$Z_0 = \frac{\eta}{2\pi\sqrt{\varepsilon_r}} \ln\left(\frac{r_o}{r_i}\right), \tag{1.1}$$

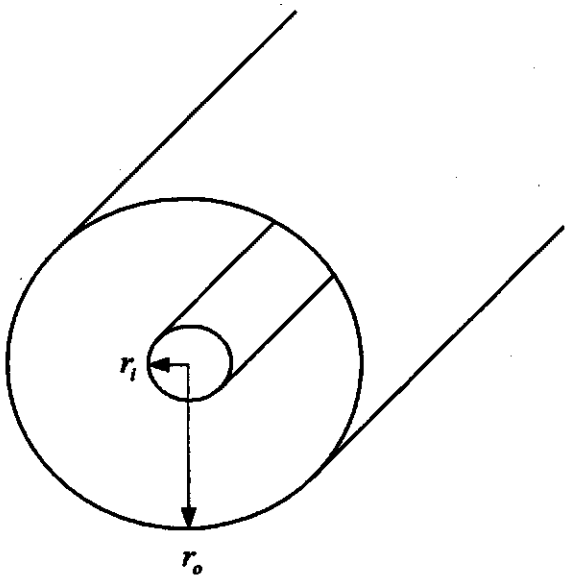

Figure 1.1 Coaxial Line

where ε_r is the relative dielectric constant of the dielectric material entirely filling the space between the conductors, and η is the free space wave impedance. Most coaxial cables for use in microwaves have a characteristic impedance of approximately $50\,\Omega$.

1.1.2 Rectangular waveguide

A rectangular waveguide is widely used for the transmission of signals at higher microwave frequencies. It consists of a hollow conducting tube of rectangular cross-section that is made to precise dimensions. There are a number of factors that make a rectangular waveguide a good transmission system: It is completely enclosed, so that there is no interference problem; waveguides have very large power handling capability; the fields of the dominant mode are linearly polarized so it is easy to excite and detect.

Set against these advantages is the disadvantage that no TEM mode can propagate along a rectangular waveguide. Consequently, the cross-section of a rectangular waveguide must be related to the wavelength of operation, in contrast to a coaxial cable, which can be made very small by comparison with the wavelength of operation.

The geometry of a rectangular waveguide is shown in Figure 1.2, where a and b are the waveguide width and height (in all applications $a > b$). The waveguide may also be filled with a dielectric medium of dielectric constant ε_r. The rectangular waveguide is the basic building block of many microwave components, such as directional couplers, magic Tees, filters, phase shifters, antennas, etc.

The cut-off wavelengths of various modes in a rectangular waveguide are given by

$$\lambda_c = \frac{1}{\sqrt{\left(\frac{m}{2a}\right)^2 + \left(\frac{n}{2b}\right)^2}}, \qquad (1.2)$$

where m and n are integers which may take any value. Each different combination of m and n constitutes a separate solution to Maxwell's equations for the given boundary

conditions. Each solution is said to give rise to a different mode of propagation in the waveguide.

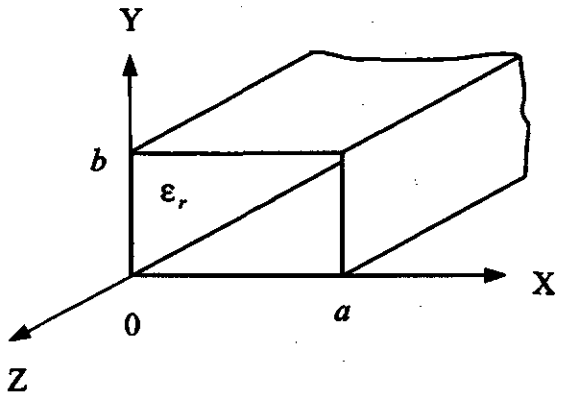

Figure 1.2 Rectangular Waveguide

A propagating wave in a waveguide will have a wavelength that is different from the characteristic wavelength of a plane wave. It is called waveguide wavelength,

$$\lambda_g = \frac{\lambda_0}{\sqrt{1-\left(\frac{\lambda_0}{\lambda_c}\right)^2}}, \tag{1.3a}$$

where λ_0 is the free-space wavelength of a plane wave. If the waveguide is filled with dielectric medium of dielectric constant ε_r, the waveguide wavelength is given by

$$\lambda_g = \frac{\lambda_0}{\sqrt{\varepsilon_r-\left(\frac{\lambda_0}{\lambda_c}\right)^2}}. \tag{1.3b}$$

1.1.3 Slab-line

The design of many UHF and microwave filters is based on electrically coupling objects located between parallel ground planes [1]. These objects include rectangular bars, and circular cylindrical rods.

The geometry of the periodic circular cylindrical rods between parallel ground planes and the dimensional notation are shown in Figure 1.3. The circular rods have diameter d and are spaced periodically at a distance c. The ground planes are separated at distance b. The spacing between adjacent rod surfaces is denoted by s and is given by

$$s = c - d . \tag{1.4}$$

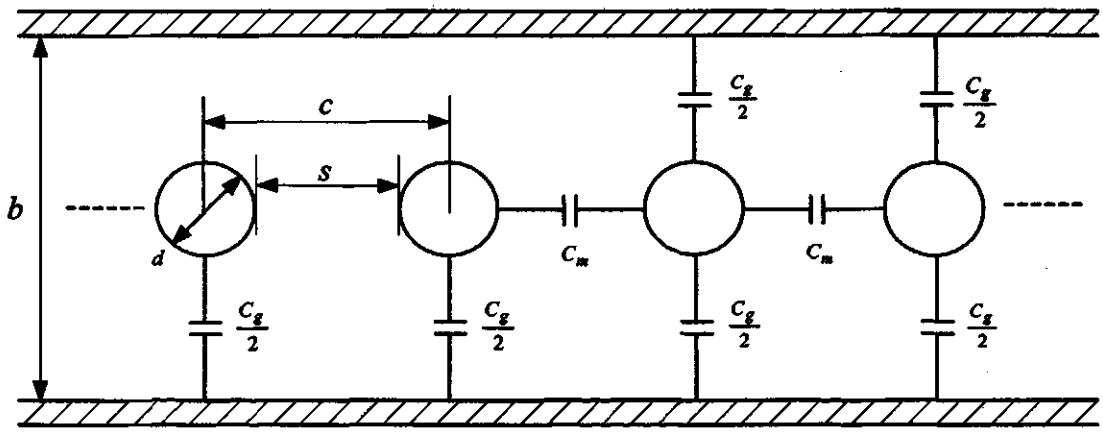

Figure 1.3 Coupled circular cylindrical rods between parallel ground planes

C_m are the mutual capacitances between successive rods and C_g is the self capacitance of each rod.

If fringing capacitances beyond nearest neighbors are neglected, it is possible to describe TEM propagation along the structure in terms of two orthogonal modes, which

have been designated as the even mode and the odd mode [1]. In the even mode, all center conductors are at the same potential as shown in Figure 1.4a. While in the odd mode successive center conductors are at equal but opposite signed potentials with respect to the ground planes as shown in Figure 1.4b. The electric field configurations for these two modes of excitation are illustrated schematically in Figure 1.4. In these illustrations, the normal component of the electric field at the plane of symmetry is zero for the even mode excitation, whereas the tangential component is zero for the odd mode excitation. This is equivalent to placing a "magnetic wall" and an "electric wall" for the even-mode and odd-mode, respectively. In terms of the potential function $\varphi(x, y)$, $\varphi = 0$ at an electric boundary, and $\partial\varphi/\partial n = 0$ at the magnetic boundary.

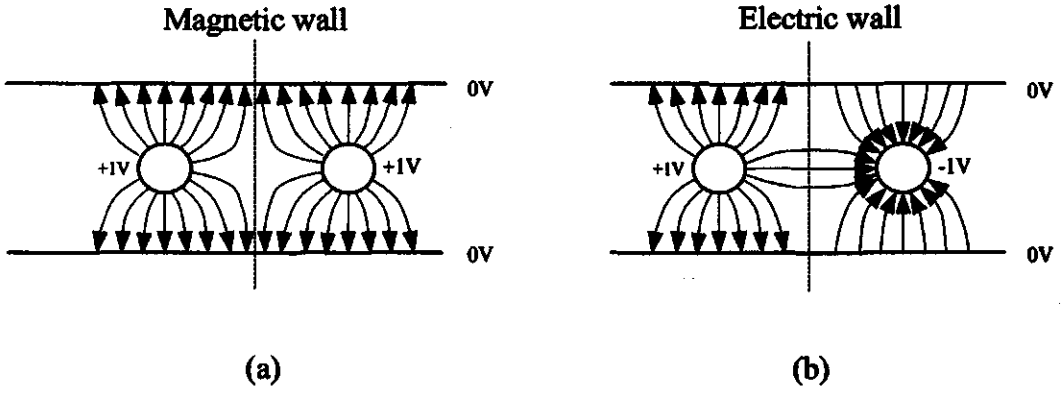

Figure 1.4 Two orthogonal modes of the electric fields: (a) Even mode, (b) Odd mode

These two TEM modes have different characteristic impedances that are intimately related to the total static capacitances of the rods to ground when in one or the other mode. The total static capacitances are related to C_m and C_g. A consideration of Figure 1.3 shows that the total capacitance measured between one rod and ground when the rods are driven in the odd mode is

$$C_o = C_g + 4C_m, \tag{1.5}$$

and the total capacitance measured between one rod and ground when the rods are driven in the even mode is

$$C_e = C_g. \tag{1.6}$$

Substituting (1.6) into (1.5) gives

$$C_m = \frac{C_o - C_e}{4}. \tag{1.7}$$

The two modes have different impedances, but they propagate with the same phase velocity if the mode is pure TEM. If the medium is inhomogeneous, as would result when different dielectric constants are used, pure TEM mode can not propagate. However, if the transverse dimensions are small in comparison with the half-wavelength in the structure, the dominant mode can be represented as quasi-TEM [2]. In such structures, the two normal modes that are supported by a pair of coupled rods propagate with different phase velocities.

Two characteristic impedances of the structure are designated as Z_e and Z_o where the subscripts e and o represent the even- and odd-modes, respectively. Under the quasi-static approximation, the even- and odd-mode impedances can be expressed in terms of the line capacitances as [2]

$$Z_e = \frac{1}{v^a \sqrt{C_e C_e^a}}, \tag{1.8}$$

and

$$Z_o = \frac{1}{v^a \sqrt{C_o C_o^a}}, \tag{1.9}$$

where v^a is the velocity of light in free space, C_e and C_o are the even- and odd-mode capacitances of the coupled line, and C_e^a and C_o^a are the even- and odd-mode capacitances of the coupled line when all dielectrics are replaced by free space. Similarly, the effective dielectric constants for the even- and odd-modes represented as ε_{fe} and ε_{fo}, respectively, can be expressed in terms of the capacitances as

$$\varepsilon_{fe} = \frac{C_e}{C_e^a}, \tag{1.10a}$$

and

$$\varepsilon_{fo} = \frac{C_o}{C_o^a}. \tag{1.10b}$$

The even- or odd-mode capacitance can be calculated as [3]:

$$C = \frac{\iint \varepsilon_r(x,y)\left|\nabla\varphi(x,y)\right|^2 dxdy}{(\Phi_2 - \Phi_1)^2}, \tag{1.11}$$

where Φ_1 and Φ_2 are the potentials.

1.2 Filters

Filters are devices that are used for the rejection of unwanted signal frequencies while permitting good transmission of wanted frequencies [4]. Filters are usually classified as lowpass, highpass, bandpass and bandstop filters, according to their frequency responses as shown in Figure 1.5. A lowpass filter, shown in Figure 1.5a, passes all frequencies up to a certain frequency and then attenuates all higher frequencies. A high-pass filter, on the other hand, illustrated in Figure 1.5b, allows no signals to pass until a certain frequency is reached, and then passes all higher frequencies. A bandpass

filter, Figure 1.5c, passes signals only in a specified frequency band; above or below this band, the microwave signal is attenuated. In contrast, a bandstop filter, Figure 1.5d, passes microwave signals at almost all frequencies, except in a narrow range where it stops or prevents the signals from passing.

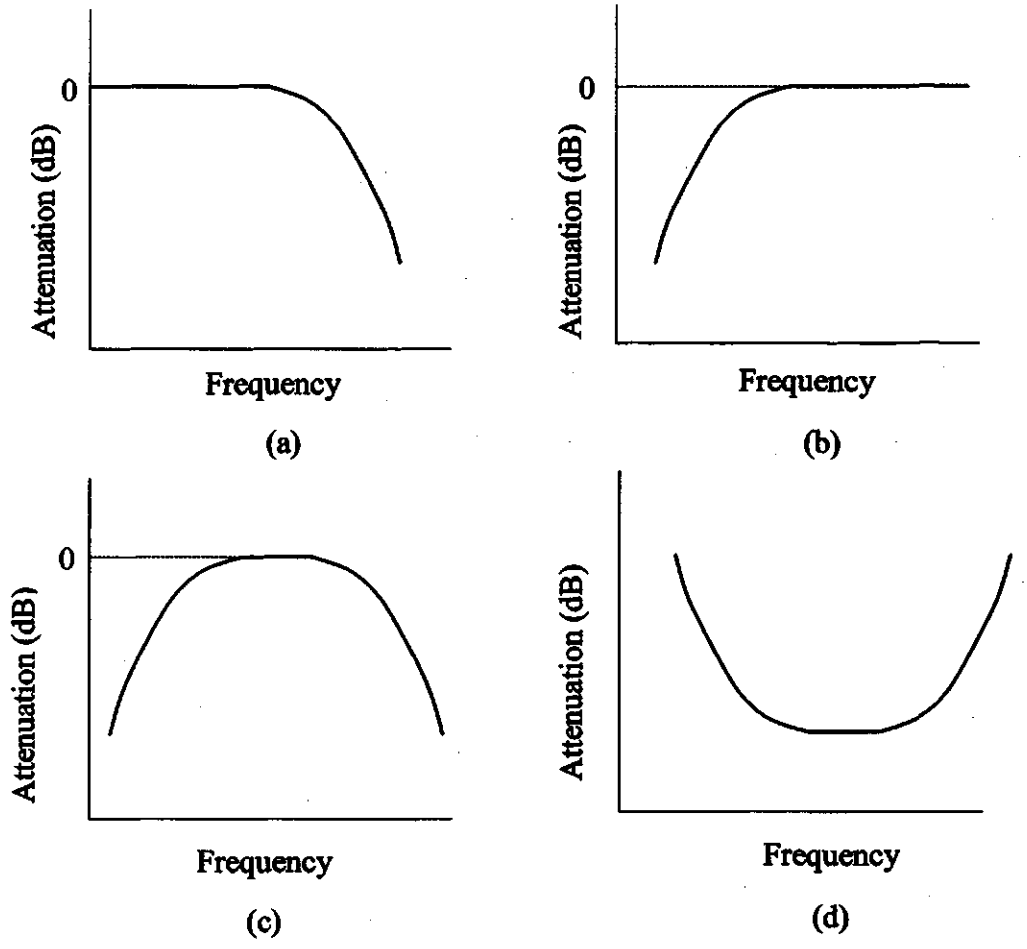

Figure 1.5 Basic types of filters: (a) Low pass, (b) High pass, (c) Bandpass, (d) Bandstop

Filters can also be classified into Butterworth, Chebyshev and elliptic filters by the shape of the ripples in the passband and the stopband as well as frequency response characteristics, as shown in Figure 1.6.

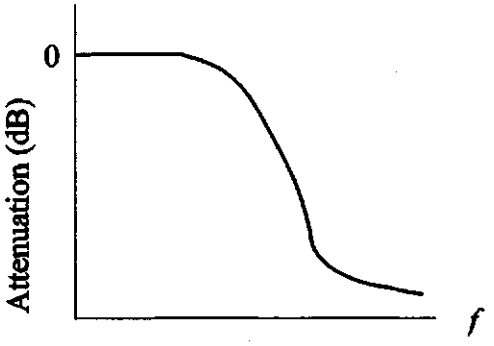

(a)

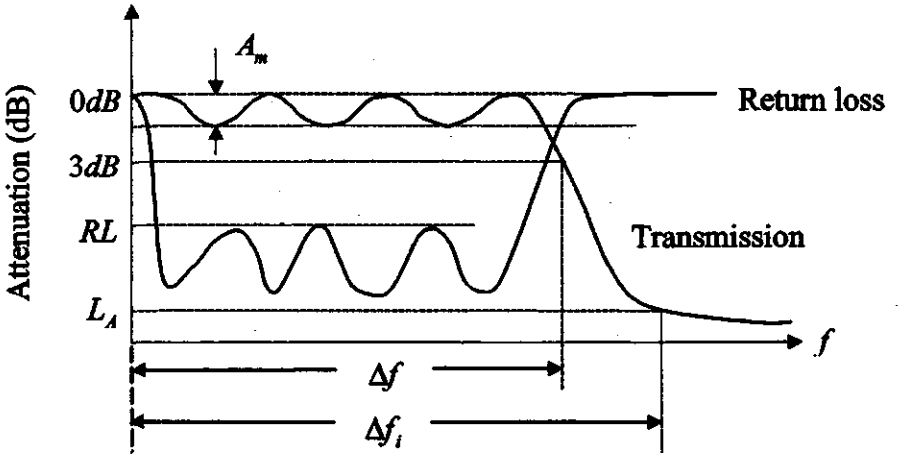

(b)

(c)

Figure 1.6 Different types of frequency response: (a) Butterworth, (b) Chebyshev, (c) Elliptic

Butterworth filters have flat passband response, Chebyshev filters have equal-ripple characteristics in the passband and elliptic filters exhibit equal-ripple characteristics in both the passband and stopband. In the waveguide filter, a Chebyshev filter is usually used, as it has sharper cutoff than a Butterworth filter and is more easily designed than an elliptic filter. In Figure 1.6(b), A_m is the amplitude of the ripple, Δf is the ripple bandwidth, Δf_i is the isolation bandwidth, RL is the passband return loss, and L_A is the stop band isolation of the filter.

Figure 1.7 shows the general representation of a filter in a microwave network. P_{in} is the incident power from the generator; P_R is the power reflected towards the generator; P_A is the power admitted to the filter and P_L the power transmitted to the load in the network.

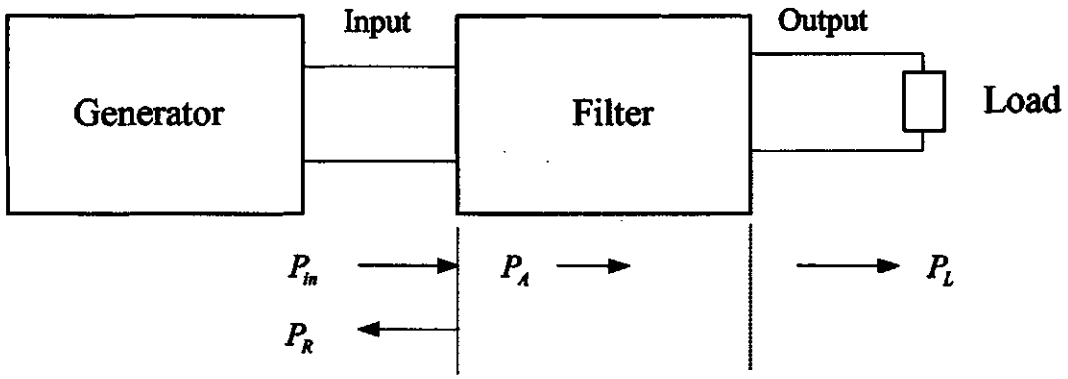

Figure 1.7 General representation of a filter network

If $P_L = P_A$, the filter is lossless. When $P_L = P_{in}$, there are no power reflections. The insertion loss (IL) and return loss (RL) at a particular frequency is defined as

$$IL = -10 log \frac{P_L}{P_{in}}, \qquad (1.12)$$

$$RL = -10 log \frac{P_R}{P_{in}}. \quad (1.13)$$

The units for both *IL* and *RL* are decibels (*dB*). Ideally, the passband insertion loss should be 0 *dB* and the stopband insertion loss should be $-\infty$. Filters in practice have a frequency response deviating from the ideal filter response, since there is a high-frequency limit for any given practical filter structure above which its characteristics will deteriorate due to junction effects, resonances within the elements, etc [5].

Microwave filters are different from conventional filters in that conventional filters use lumped elements while microwave filters use either distributed elements or a combination of both elements, according to network theory.

At low frequencies, lumped elements (capacitors or inductors) can be used to realize filters, since the phase variation of the signal over the largest dimension of the element is negligible. It is possible to synthesize accurately a lumped element filter from the required filter response by following procedures based on network theory. While at microwave frequencies, electric and magnetic fields have to be considered in the design of filters using distributed elements, rather than the voltage and current as in the case of lumped elements. Thus designing filters using distributed elements is more complicated, as will be shown in the following chapters.

1.3 Commercial simulation tools

1.3.1 Micro-Stripes

Micro-Stripes [6] is a powerful suite of programs ideal for the analysis of waveguide components, planar and non-planar circuit structures, transitions and a variety of antennas. It provides 3D electromagnetic analyses of arbitrary geometries, yielding

results in both the time-domain and frequency-domain. The software is based on the well-established Transmission Line Matrix Method (TLM) that guarantees short computation times and efficient use of memory. Micro-Stripes calculates the impulse response of a device and a comprehensive range of post-processing programs are available for generating other results, including S-parameters and far-field radiation patterns. The software, featuring a window-based graphical user interface, is easy to use.

1.3.2 FullWave

FullWave software [7], based on the Finite Element Method, uses powerful field solution methods together with an easy-to-use interface to generate full-wave solutions of 3D high frequency structures. With three solvers in one package, FullWave generates S-Parameters, resonance solutions and port solutions, and displays numeric and graphical information including 3D field animations.

1.3.3 PDEase2

PDEase2 [8] is a powerful and flexible software package for obtaining numerical solutions of static and time-dependent systems of linear and nonlinear partial differential equations by the 2D Finite Element Method. It is designed for scientists, engineers, and mathematicians who as part of their work encounter boundary value problems involving partial differential equations and who want to solve them without spending too much time learning computer programming.

1.4 Research objectives

The main objective of the research described in this thesis is to show that the existing electromagnetic field analysis tools can be used successfully to synthesize microwave bandpass and lowpass filters over a wide frequency band. The research objectives consist of the following parts:

(1) To design TEM mode based ceramic block bandpass filters using the inter-resonator coupling database, generated by the Finite Element Method and the Finite Difference Method, and thereby, to prove the validity of the 2-D simulator based design approach.

(2a) To develop a wide range of design databases for all types of round rod coupled waveguide bandpass filters, using commercially available 3-D microwave time domain analysis packages.

(2b) To design round rod coupled waveguide bandpass filters using the design databases in Part (2a) and to verify the results by the Mode Matching Method and the Finite Element Method.

(3a) To generate an accurate wide-range design databases for capacitive iris coupled waveguide low-pass filters using commercially available 3-D simulators.

(3b) To design capacitive iris coupled waveguide low-pass filters using the databases developed in Part (3a), and to verify the computed results by experimental results.

1.5 Thesis overview

Chapter 2 of the thesis begins with a detailed discussion about the background of this research and a literature review. It then discusses the concepts of K- and J-inverters, waveguide discontinuities and scattering matrix.

Chapter 3 is devoted to a brief discussion of numerical techniques used in electromagnetics and microwaves.

Chapter 4 is devoted to TEM and TE mode bandpass and TE mode low-pass filter synthesis.

Chapter 5 presents and discusses the results.

Chapter 6 concludes the thesis with recommendations for future research in this area.

1.6 Chapter summary

This chapter introduces the fundamental concepts of microwaves. Several waveguide configurations including coaxial cable, rectangular waveguide, and slab-line are also introduced in this chapter. It also discusses the definitions associated with and classifications of microwave filters. These concepts are very important for the design of the filters discussed in the following chapters. Several commercial simulation tools are introduced. Finally, the research objectives and thesis overview are stated.

Chapter 2 Literature Review and Background

2.1 Literature survey

In modern communication systems, the demand for hand-held cellular mobile communication sets has increased tremendously in recent years. In these systems, compact size and low cost radio equipment have significant importance. Since microwave filters are the most common passive components in any microwave network, and transmitting and receiving filters form a large part of the equipment, it is desirable to reduce filter size and cost to achieve the foregoing requirements.

Modern filters can be traced back to 1915, when Wagner in Germany and Campbell in the United States, working independently, proposed the filter [4, 9-12]. Previously, selectivity was provided by a single series or shunt resonator. In 1923, Zobel at Bell Laboratories published a method for filter design using simple mathematics. His approximate "image parameter" technique was the only practical filter design method used for decades.

Around 1940, Darlington [13] published theories on the exact synthesis of networks to prescribed transfer functions. Due to heavy computational requirements, these methods remained primarily academic until digital computers were used to synthesize low-pass "prototypes". Over the last several decades, modern filter theory has been significantly embellished by many contributors [4, 14-15].

Work on microwave filters commenced prior to the war, with a particularly significant early paper being published in 1937 by W. P. Mason and R. A. Sykes[16]. Mason and Sykes used A, B, C, and D parameters, although not in matrix form, to derive the image impedance and image phase and attenuation functions of a rather large variety of useful filter sections.

Major advances and applications, mainly using image parameters, were made at various laboratories in the United States during the World War II years of 1941 to 1945. At the M.I.T. Radiation Laboratory, emphasis was on waveguide cavity filters, while at the Radio Research Laboratory, work was concentrated on broad-band low-pass, bandpass, and high-pass coaxial filters and also on narrow-band tunable coaxial resonator filters for search receivers. Much of this work is described in the M.I.T. Radiation Laboratory Series by Fano and Lawson [17]. The scientists and engineers who worked in the Radiation Laboratory and in associated microwave laboratories both in the U.S.A. and in the U.K. were among the best in the world, including such well-known names as H. A. Bethe, N. Marcuvitz, E. M. Purcell, and J. Schwinger. Some of their work at this time is still unsurpassed, particularly in the area of field theory. The chapter on the theory of microwave filters in [17] is superb, and remains one of the clearest introductions to the topic to this day. Network theory was probably the most advanced topic in engineering at that time, S. Darlington having published his famous cascade synthesis theory as far back as 1939 [13]. Fano and Lawson [17] succeeded in writing a very clear and concise summary of Darlington's theory.

Chapter 10 of [17] on the design of microwave filters contains some surprisingly modern designs, e.g., describing filters with finite frequency attenuation poles and dual-

mode cavities. In the case of the direct-coupled filter, the Fano and Lawson theory was based on a low-pass prototype, but the implementation was far from obvious, requiring a difficult synthesis procedure. The main problem was the lack of specific formulas for the low-pass prototype element values. Such formulas, at least for the important Chebyshev case, did not appear until several years later [18-19]. A short time later, the first really comprehensive theory appeared, supplying the "missing parts" of the Fano and Lawson theory [20]. This paper also extended the range of applicability to much broader bandwidths, i.e., about 20 percent in terms of guide wavelength, and the bandwidth was exceptionally easy to apply by any engineering specialist, requiring only the solution of very simple specific equations.

A good account of various synthesis techniques for microwave filters can be obtained from the famous book, Microwave Filters, Impedance-Matching Networks, and Coupling Structures by Matthaei, Young and Jones [4], considered to be the bible of microwave passive circuit design. The book was first published in the 1960s and it presents the design method for various types of microwave filters, using the circuit and transmission line theory. Physical implementation of all those methods invariably requires post production tuning because the circuit theory approach cannot always take into consideration the second order parasitic effects, which in many cases have some effects to the performance of the designed filters. Consequently, with the steady advancement of computer technology and the availability of cheaper computer power, designers have recourse to the field theory approach to microwave filter design. As a result, Computer Aided Design (CAD) of microwave filters has become a very important area of research and development during the last few decades. During the past few

decades many articles have appeared in the literature showing the analysis optimization methods for the synthesis of waveguide cavity filters [21]. Such methods need stand alone computer programs for the design of each type of filter and invariably require large computer speed and memory.

In the last decade, the world of CAD of microwave circuits has witnessed the appearance of much 2-D and 3-D analysis based computer software for the design and analysis of passive microwave circuits. The software is based on the complete 2-D or 3-D electromagnetic solution of Maxwell's Equations for the particular structure to be analyzed or synthesized. The methods use the Transmission Line Matrix (TLM) [6] or the Finite Difference Time Domain (FDTD) [22] method for analysis in the time domain and the Finite Element Method (FEM) [7, 23], the Finite Difference Method (FDM) or the Moment Method (MM) [24-26] for analysis in the frequency domain. All these software packages are quite versatile and can accurately analyze any electromagnetic structure that does not involve any active device.

This thesis shows how to make use of these general-purpose software to design successfully any coupled cavity type microwave bandpass or low-pass filters. Almost all versions of the most commonly used slab-line, round rod or iris coupled resonator waveguide filters are chosen.

2.2 K- and J-inverters

In this section K- and J-inverters will be introduced. They are used in the design of filters in the following chapters.

In deriving design equations for certain types of lowpass or bandpass filters, it is desirable to convert the prototype shown in Figure 2.1 which uses both inductances and capacitances to equivalent forms which use only inductances or only capacitances [4]. This can be done with the aid of the idealized inverters that are shown in Figure 2.2.

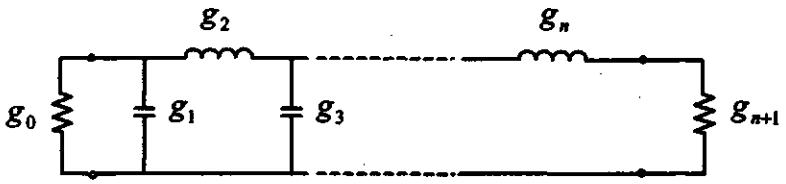

Figure 2.1 One prototype low-pass filter circuit

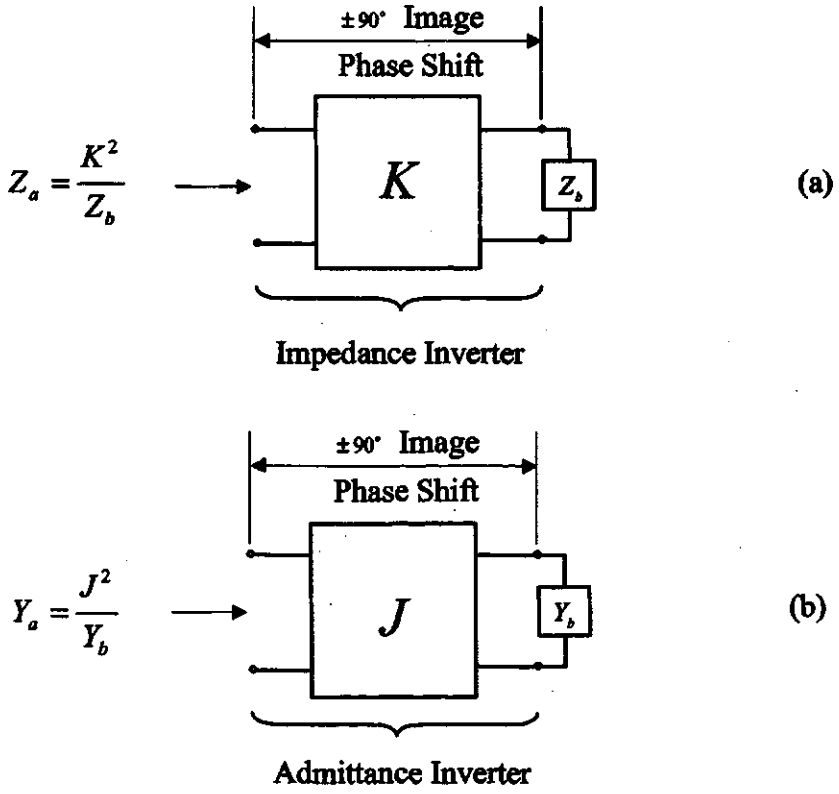

Figure 2.2 Definition of impedance inverter and admittance inverter

An idealized impedance inverter operates like a quarter-wavelength line of characteristic impedance K at all frequencies. Therefore, if it is terminated in an impedance Z_b on one end, the impedance Z_a seen looking in at the other end is

$$Z_a = \frac{K^2}{Z_b} . \tag{2.1}$$

An idealized admittance inverter as defined herein is the admittance representation of the same thing, i.e., it operates like a quarter-wavelength line of characteristic admittance J at all frequencies. Thus, if an admittance Y_b is attached at one end, the admittance Y_a seen looking in the other end is

$$Y_a = \frac{J^2}{Y_b} . \tag{2.2}$$

As indicated in Figure 2.2, an inverter may have an image phase shift of either $\pm 90°$ degrees or an odd multiple thereof.

Because of the inverting action indicated by Equations (2.1) and (2.2) a series inductance with an impedance inverter on each side looks like a shunt capacitance from its exterior terminals. Likewise, a shunt capacitance with an admittance inverter on both sides looks like a series inductance from its external terminals. Making use of this property, the prototype circuit in Figure 2.1 can be converted to either of the equivalent forms in Figure 2.3 which have identical transmission characteristics to the prototype in Figure 2.1.

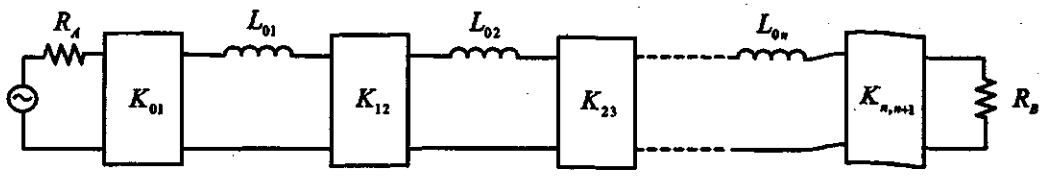

$$K_{01} = \sqrt{\frac{R_A\, L_{01}}{g_0\, g_1}}, \qquad K_{k,k+1}\Big|_{\text{for } k=1 \text{ to } n-1} = \sqrt{\frac{L_{0k}\, L_{0(k+1)}}{g_k\, g_{k+1}}}, \qquad K_{n,n+1} = \sqrt{\frac{L_{0n}\, R_B}{g_n\, g_{n+1}}}$$

(a) Modified prototype using impedance inverters

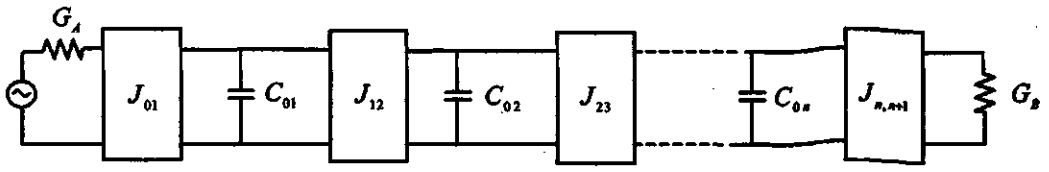

$$J_{01} = \sqrt{\frac{G_A\, C_{01}}{g_0\, g_1}}, \qquad J_{k,k+1}\Big|_{\text{for } k=1 \text{ to } n-1} = \sqrt{\frac{C_{0k}\, C_{0(k+1)}}{g_k\, g_{k+1}}}, \qquad J_{n,n+1} = \sqrt{\frac{C_{0n}\, G_B}{g_n\, g_{n+1}}}$$

(b) Modified prototype using admittance inverters

Figure 2.3 Low-pass prototypes modified to include impedance inverters or admittance inverters

As can be seen from Equations (2.1) and (2.2), inverters have the ability to shift impedance or admittance levels depending on the choice of the K or J parameters. For this reason, in Figure 2.3(a) the sizes of R_A, R_B, and the inductances L_{0k} may be chosen arbitrarily and the response will be identical to that of the original prototype as in Figure 2.1 provided that the inverter parameters $K_{k,k+1}$ ($k = 0$ to n) are specified as indicated by the equations in Figure 2.3(a). The same holds for the circuit in Figure 2.3(b), only on the dual basis.

2.3 Waveguide discontinuities

In order to realize the different kinds of filter responses shown in Figure 1.5, or in other words, to change the frequency response of an uniform waveguide, some waveguide discontinuities have to be put in the waveguide to disturb the electric and magnetic fields of an otherwise uniform waveguide. Such discontinuities give rise to inductive and capacitive effects in the circuit. However unlike true lumped inductors and capacitors, they are frequency dependent. In microwave transmission line circuits it is rare to come across any line without some discontinuities of one type or another.

2.3.1 Step junctions

Usually there are three kinds of step discontinuities in a rectangular waveguide as shown in Figure 2.4. An E-plane step is a junction of two rectangular waveguides with equal widths but unequal heights, as shown in Figure 2.4a. An H-plane step is a junction of two rectangular waveguides with unequal widths but equal heights, as shown in Figure 2.4b; and an EH-plane step is a junction of two rectangular waveguides with unequal widths and unequal heights as in Figure 2.4c. All three discontinuities shown in Figure 2.4 are symmetric, but they can be asymmetric.

2.3.2 Iris

When two E-plane step junctions (*A* and *B*) are connected back to back with a small waveguide section of length t, an E-plane iris is formed as shown in Figure 2.5. In an E-plane iris, the width of the waveguide remains constant while the height of the waveguide changes. Similarly, two H-plane step junctions or two EH-plane step junctions

can be connected back to back with a smaller waveguide section between them, to form an H-plane or an EH-plane iris, respectively.

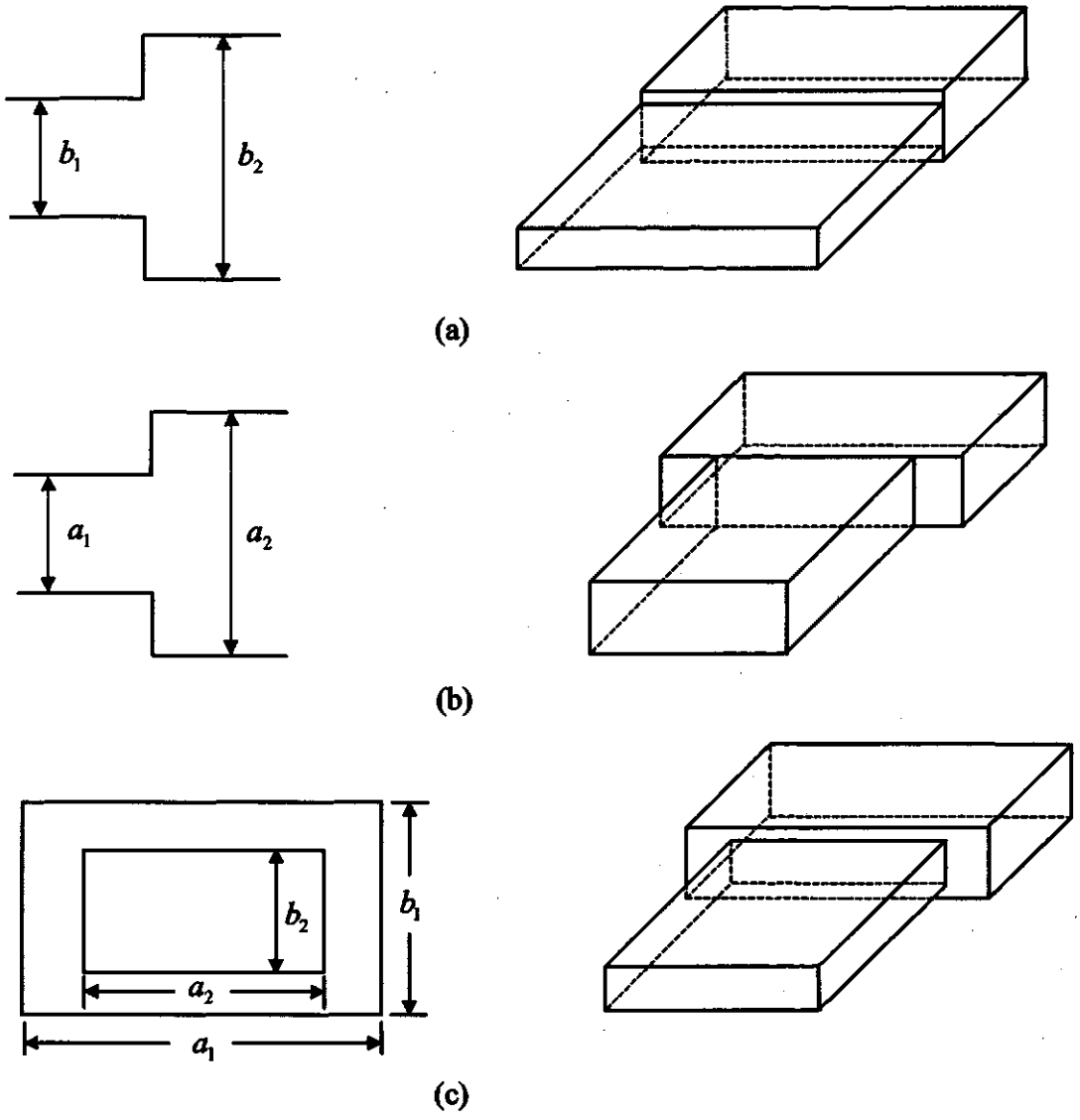

Figure 2.4 Step discontinuities in rectangular waveguide: (a) E-plane, (b) H-plane, (c) EH-plane

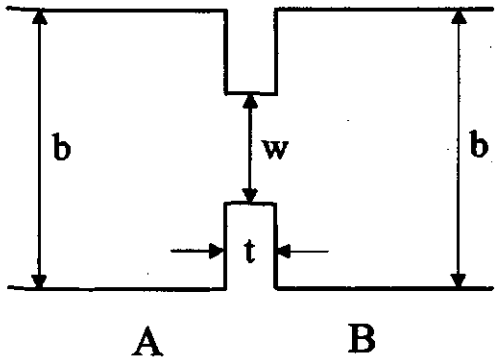

Figure 2.5 E-plane iris in a rectangular waveguide

2.3.3 Round rod

An inductive post is realized by using a metallic round rod placed across the rectangular waveguide, parallel to the narrow walls and therefore parallel to the electric field of the TE_{10} mode [9-10]. A configuration for this discontinuity is shown in Figure 2.6a. The post can be centered, or off-centered. Sometimes two or more posts are used as waveguide discontinuities as shown in Figure 2.6b [10].

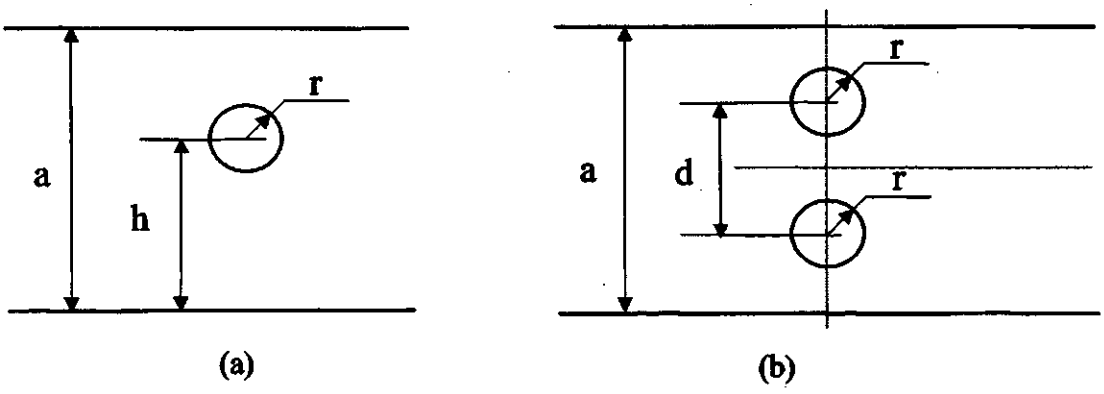

Figure 2.6 Round rod discontinuities in a waveguide: (a) One rod, (b) Two rods

A capacitive post can also be obtained by placing a metallic round rod across the rectangular waveguide, parallel to the wider walls and therefore with its axis perpendicular to the electric field [9].

2.4 Scattering matrix

At lower frequencies, electric networks are characterized invariably in terms of voltages and currents at various ports. Since the voltage, currents, and impedances cannot be measured in a direct manner at microwave frequencies, the quantities must therefore be regarded as secondary, or derived, quantities. The directly measurable quantities are the amplitudes and phase angles of the waves reflected, or scattered, from a junction relative to the incident-wave. Again, in view of the linearity of the field equations and most microwave devices, the scattered-wave amplitudes are linearly related to the incident-wave amplitudes. The matrix describing this linear relationship is called the scattering matrix.

Consider the *N*-port junction of Figure 2.7. If a wave with an associated equivalent voltage V_1^+ is incident on the junction at terminal plane t_1, a reflected wave $S_{11}V_1^+ = V_1^-$ will be produced in line 1, where S_{11} is the reflection coefficient, or scattering coefficient, for line 1, with a wave incident on line 1. Waves will also be transmitted, or scattered, out of the other junctions and will have amplitudes proportional to V_1^+. These amplitudes can be expressed as $V_n^- = S_{n1}V_1^+$, $n = 2, 3, \ldots, N$, where S_{n1} is a transmission coefficient on line n from line 1. When waves are incident in all lines, the scattered wave in each line has contributions arising from all the incident waves. Thus, in general, it can be written as

$$\begin{bmatrix} V_1^- \\ V_2^- \\ \cdots \\ V_N^- \end{bmatrix} = \begin{bmatrix} S_{11} & S_{12} & S_{13} & \cdots & S_{1N} \\ S_{21} & S_{22} & S_{23} & \cdots & S_{2N} \\ \cdots & \cdots & \cdots & \cdots & \cdots \\ S_{N1} & S_{N2} & S_{N3} & \cdots & S_{NN} \end{bmatrix} \begin{bmatrix} V_1^+ \\ V_2^+ \\ \cdots \\ V_N^+ \end{bmatrix}, \tag{2.3a}$$

or

$$[V^-] = [S][V^+], \tag{2.3b}$$

where $[S]$ is called the scattering matrix.

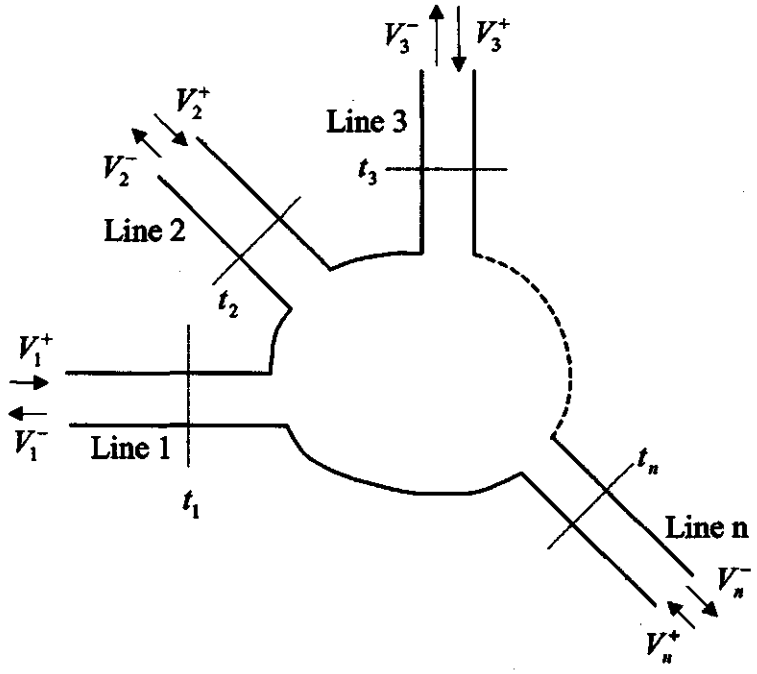

Figure 2.7 An *N*-port junction illustrating scattering waves

At any particular frequency and for a given location of the terminal planes, the scattering-matrix elements S_{nm} have definite values. If the frequency is changed, these elements change values also, in a manner not readily deduced analytically in general. However, at a fixed frequency the change in the scattering-matrix elements arising from a shift in the terminal-plane location is readily found.

Suppose letting terminal plane t_n be shifted outward an amount l_n corresponding to an electrical phase shift of $\theta_n = \beta_n l_n$, where β_n is the propagation phase constant for the nth line. If the incident-wave voltage is still denoted by V_n^+ at this new terminal plane, all the transmission coefficients S_{mn}, $m \neq n$, for transmission into line m from line n must be multiplied by $e^{-j\theta_n}$, to account for the additional path length over which the waves must travel. The reflected wave in line n has traveled a distance $2l_n$ more relative to the incident wave at the new terminal plane. Thus the new value of S_{nn} is $e^{-2j\theta_n} S_{nn}$. Likewise, waves traveling from line m to line n must travel a distance l_n farther, and thus S_{nm} is changed to $e^{-j\theta_n} S_{nm}$. These results are readily expressed in the general case by the following transformation of the $[S]$ matrix into the new $[S']$ matrix:

$$[S'] = \begin{bmatrix} e^{-j\theta_1} & & & \\ & e^{-j\theta_2} & & \\ & & \ddots & \\ & & & e^{-j\theta_N} \end{bmatrix} \begin{bmatrix} S_{11} & S_{12} & S_{13} & \cdots & S_{1N} \\ S_{21} & S_{22} & S_{23} & \cdots & S_{2N} \\ \cdots & \cdots & \cdots & \cdots & \cdots \\ S_{N1} & S_{N2} & S_{N3} & \cdots & S_{NN} \end{bmatrix} \begin{bmatrix} e^{-j\theta_1} & & & \\ & e^{-j\theta_2} & & \\ & & \ddots & \\ & & & e^{-j\theta_N} \end{bmatrix}, \tag{2.4}$$

where $\theta_n = \beta_n l_n$ is the outward electrical phase shift of the nth terminal plane.

For a reciprocal junction the scattering matrix is symmetrical, that is, $S_{nm} = S_{mn}$, or,

$$S = S^t, \tag{2.5}$$

where the superscript t indicates the transpose of a matrix.

For a lossless passive junction the total power leaving the N ports must equal the total incident power. The mathematical statement of this power-conservation condition is

$$\sum_{n=1}^{N}|S_{ni}|^2 = \sum_{n=1}^{N} S_{ni}S_{ni}^* = 1, \qquad \text{for all } i = 1, 2, \cdots, N, \tag{2.6a}$$

i.e. the inner product of any column of the scattering matrix with its own conjugate equals unity, and

$$\sum_{n=1}^{N} S_{ns}S_{nr}^* = 0, \qquad \text{for all } s, r = 1, 2, \cdots, N, \quad s \neq r, \tag{2.6b}$$

i.e. the inner product of any column of a scattering matrix with the complex conjugate of any other column is zero.

Since many common microwave circuits are two-port junctions, the scattering-matrix description can be simpler with only four elements, S_{11}, S_{21}, S_{12}, and S_{22}. The incident- and scattered-wave amplitudes are related by

$$[V^-] = [S][V^+], \tag{2.7a}$$

or

$$V_1^- = S_{11}V_1^+ + S_{12}V_2^+, \tag{2.7b}$$

$$V_2^- = S_{21}V_1^+ + S_{22}V_2^+. \tag{2.7c}$$

A two-port network is symmetrical when an interchange of ports 1 and 2 does not alter its configuration or characteristics in any manner. This symmetry results in the following relationships among *S*-parameters:

$$S_{11} = S_{22}, \tag{2.8a}$$

and

$$S_{12} = S_{21}. \tag{2.8b}$$

That is, only two parameters (out of the total of four) need be evaluated.

In several microwave circuits, two-port components are connected in cascade, i.e., the port 2 of the first component is connected to the port 1 of the second component (and so on), as shown in Figure 2.8. S-matrix of the combination can be written in terms of S-matrices of components *A* and *B*. Say

$$[S^A]=\begin{bmatrix} S_{11}^A & S_{12}^A \\ S_{21}^A & S_{22}^A \end{bmatrix}, \tag{2.9a}$$

and

$$[S^B]=\begin{bmatrix} S_{11}^B & S_{12}^B \\ S_{21}^B & S_{22}^B \end{bmatrix}. \tag{2.9b}$$

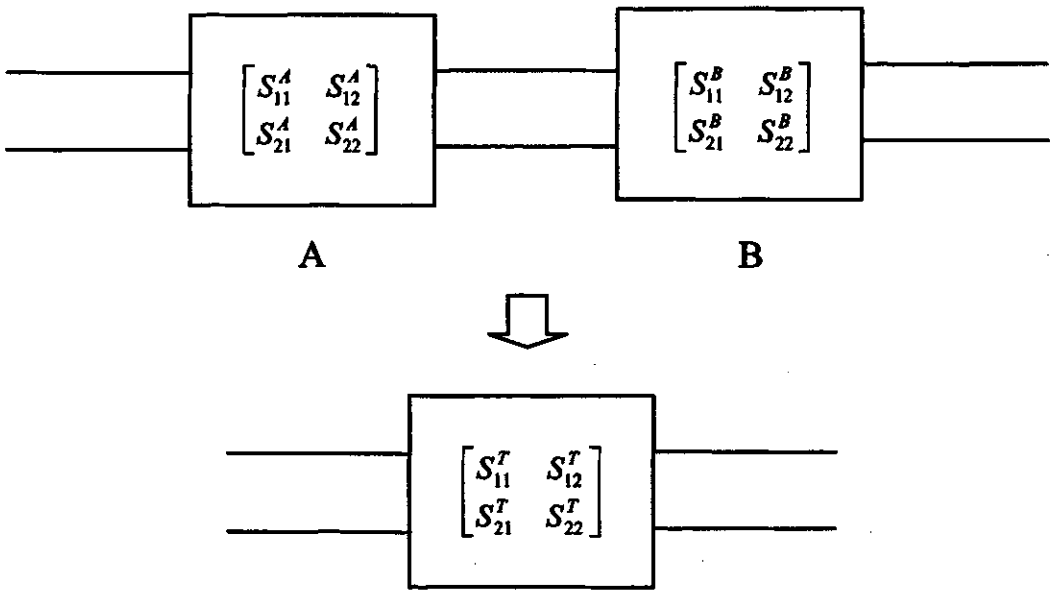

Figure 2.8 Cascading of S matrices

The overall resulting scattering matrix S^T is given by [11]

$$[S^T]=\begin{bmatrix} S_{11}^T & S_{12}^T \\ S_{21}^T & S_{22}^T \end{bmatrix}=\begin{bmatrix} S_{11}^A+\dfrac{S_{12}^A S_{11}^B S_{21}^A}{1-S_{22}^A S_{11}^B} & \dfrac{S_{12}^A S_{12}^B}{1-S_{22}^A S_{11}^B} \\ \dfrac{S_{21}^A S_{21}^B}{1-S_{22}^A S_{11}^B} & S_{22}^B+\dfrac{S_{21}^B S_{22}^A S_{12}^B}{1-S_{22}^A S_{11}^B} \end{bmatrix}. \quad (2.9c)$$

This relation can be used repeatedly to obtain S-matrix of a cascade with two or more than two components.

2.5 Chapter summary

A literature survey on microwave filter design is presented in this chapter. Some important concepts on K- and J- inverters, waveguide discontinuities and scattering matrix are described. The chapter also discusses the roles of different types of waveguide and slab-line discontinuities in microwave filter realization.

Chapter 3 Numerical Techniques in Electromagnetics and Microwaves

3.1 Introduction

Scientists and engineers use several techniques in solving continuum or field problems. Loosely speaking, these techniques can be classified as experimental, analytical, or numerical [27]. Experiments are expensive, time consuming, sometimes hazardous, and usually do not allow much flexibility in parameter variation. Analytical methods include Separation of Variables, Series Expansion, Conformal Mapping, Integral Solutions (e.g., Laplace and Fourier Transforms), and Perturbation Methods. They give exact solutions. Numerical Methods usually give approximate solutions of sufficient accuracy for engineering purposes. They include Finite Difference Method, Method of Weighted Residuals, Moment Method, Finite Element Method, Transmission-line Modeling, Monte Carlo Method, etc.

The need for numerical solution of electromagnetic (EM) problems is best expressed in the words of Paris and Hurd [28]: "Most problems that can be solved formally (analytically) have been solved." Until the 1940s, most EM problems were solved using the classical methods of Separation of Variables and Integral Equation Solutions. Besides the fact that a high degree of ingenuity, experience, and effort were required to apply those methods, only a narrow range of practical problems could be investigated due to the complex geometries defining the problems.

Numerical solution of EM problems started in the mid-1960s with the availability of modern high-speed digital computers. Since then considerable effort has been expended on solving practical, complex EM-related problems for which closed form analytical solutions are either intractable or do not exist. The numerical approach has the advantage of allowing the actual work to be carried out by operators without a knowledge of higher mathematics or physics, with a resulting economy of labor on the part of the highly trained personnel.

There are two important theorems commonly used in EM. These are the divergence (Gauss's) theorem

$$\oint_S F \cdot dS = \int_v \nabla \cdot F dv \,, \tag{3.1}$$

and Stokes's theorem

$$\oint_L F \cdot dl = \int_S \nabla \times F \cdot dS \,, \tag{3.2}$$

where F is a vector, and $\nabla \cdot F$ and $\nabla \times F$ are the divergence and curl of the vector.

For electrostatic fields, the two fundamental laws governing this type of field are Gauss's law,

$$\oint D \cdot dS = \int \rho_v dv \,, \tag{3.3}$$

which is a direct consequence of Coulomb's force law, and the law describing electrostatic field as conservative,

$$\oint E \cdot dl = 0 \,. \tag{3.4}$$

In Equations (3.3) and (3.4), D and E are the electric flux density and electric field intensity, respectively; ρ_v is the volume charge density (in $coulombs/meter^3$).

The integral form of the laws in Equations (3.3) and (3.4) can be expressed in the differential form by applying Equation (3.1) to Equation (3.3) and Equation (3.2) to Equation (3.4). That is

$$\nabla \cdot D = \rho_v, \tag{3.5}$$

and

$$\nabla \times E = 0. \tag{3.6}$$

The vector fields D and E are related as

$$D = \varepsilon E, \tag{3.7}$$

where ε is the dielectric permittivity of the medium. In terms of the electric potential V (in *volts*), E is expressed as

$$E = -\nabla V, \tag{3.8}$$

or

$$V = -\int E \cdot dl. \tag{3.9}$$

Combining Equations (3.5), (3.7), and (3.8) gives Poisson's equation:

$$\nabla \cdot \varepsilon \nabla V = -\rho_v, \tag{3.10a}$$

or, if ε is constant,

$$\nabla^2 V = -\frac{\rho_v}{\varepsilon}. \tag{3.10b}$$

When $\rho_v = 0$, Equation (3.10) becomes Laplace's equation

$$\nabla \cdot \varepsilon \nabla V = 0, \tag{3.11a}$$

or for constant ε,

$$\nabla^2 V = 0. \tag{3.11b}$$

3.2 The Finite Difference Method (FDM)

3.2.1 Finite difference equation

The Finite Difference Method is probably the simplest of the numerical methods used to solve Partial Differential Equations (PDE). First, take a look at how finite difference approximations are constructed.

Given a function $f(x)$ shown in Figure 3.1, its derivative, slope or the tangent at point P can be approximated by the slope of the arc PB, giving the forward-difference formula,

$$f'(x_0) \approx \frac{f(x_0+\Delta x)-f(x_0)}{\Delta x}, \tag{3.12}$$

or the slope of the arc AP, yielding the backward-difference formula,

$$f'(x_0) \approx \frac{f(x_0)-f(x_0-\Delta x)}{\Delta x}, \tag{3.13}$$

or the slope of the arc AB, resulting in the central-difference formula,

$$f'(x_0) \approx \frac{f(x_0+\Delta x)-f(x_0-\Delta x)}{2\Delta x}. \tag{3.14}$$

The second derivative of $f(x)$ at P can also be estimated as

$$f''(x_0) \approx \frac{f'(x_0+\Delta x/2)-f'(x_0-\Delta x/2)}{\Delta x}. \tag{3.15a}$$

As Δx is very small, $f'(x_0+\Delta x/2)$ and $f'(x_0-\Delta x/2)$ can be approximated by $f'(x_0+\Delta x)$ and $f'(x_0-\Delta x)$, respectively. That is

$$f''(x_0) \approx \frac{1}{\Delta x}\left[\frac{f(x_0+\Delta x)-f(x_0)}{\Delta x}-\frac{f(x_0)-f(x_0-\Delta x)}{\Delta x}\right], \tag{3.15b}$$

or $$f''(x_0) \approx \frac{f(x_0+\Delta x)-2f(x_0)+f(x_0-\Delta x)}{(\Delta x)^2}. \qquad (3.15c)$$

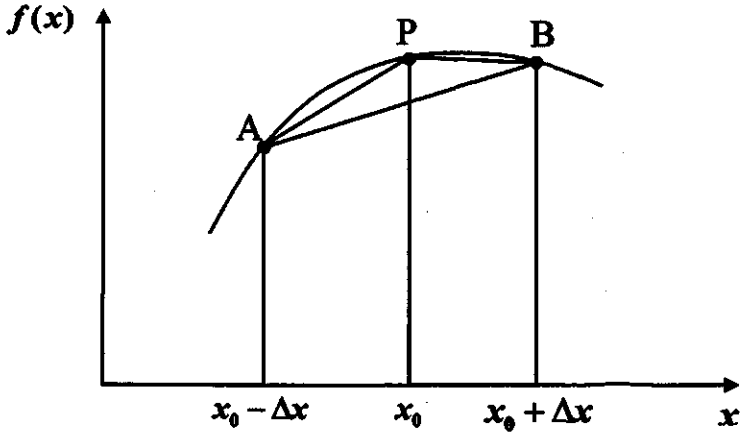

Figure 3.1 Estimates for the derivative of $f(x)$ at point P using forward, backward, and central differences

Any approximation of a derivative in terms of values at a discrete set of points is called finite difference approximation.

The same results can be obtained by use of Taylor's series. According to the well-known expansion,

$$f(x_0+\Delta x) = f(x_0)+\Delta x f'(x_0)+\frac{1}{2!}(\Delta x)^2 f''(x_0)+\frac{1}{3!}(\Delta x)^3 f'''(x_0)+\cdots, \qquad (3.16)$$

and

$$f(x_0-\Delta x) = f(x_0)-\Delta x f'(x_0)+\frac{1}{2!}(\Delta x)^2 f''(x_0)-\frac{1}{3!}(\Delta x)^3 f'''(x_0)+\cdots. \qquad (3.17)$$

Upon adding Equations (3.16) and (3.17),

$$f(x_0+\Delta x)+f(x_0-\Delta x) = 2f(x_0)+(\Delta x)^2 f''(x_0)+O(\Delta x)^4, \qquad (3.18)$$

where $O(\Delta x)^4$ is the error introduced by truncating the series which is not greater than $(\Delta x)^4$. Assuming this term is negligible (usually Δx is very small),

$$f''(x_0) \approx \frac{f(x_0+\Delta x)-2f(x_0)+f(x_0-\Delta x)}{(\Delta x)^2},$$

which is Equation (3.15c). Subtracting Equation (3.17) from Equation (3.16) and neglecting terms of the order $(\Delta x)^3$ yields

$$f'(x_0) \approx \frac{f(x_0+\Delta x)-f(x_0-\Delta x)}{2\Delta x},$$

which is Equation (3.14). This shows that the leading errors in Equations (3.14) and (3.15c) are of the order $(\Delta x)^2$. Similarly, the difference formula in Equations (3.12) and (3.13) have truncation errors of $O(\Delta x)$. Higher order finite difference approximations can be obtained by taking more terms in Taylor series expansion. If the infinite Taylor series were retained, an exact solution would be realized for the problem. However, for practical reasons, the infinite series is usually truncated after the second-order term. This imposes an error that exists in all finite difference solutions.

The first step in applying the finite-difference method is to select a discrete set of values x and y, the mesh points, as illustrated in Figure 3.2 for two dimensions. If the spatial interval that separates the points in the mesh is denoted by h, the mesh points can be denoted by the discrete index k, where

$$x_k = kh, \tag{3.19}$$

$$y_k = kh. \tag{3.20}$$

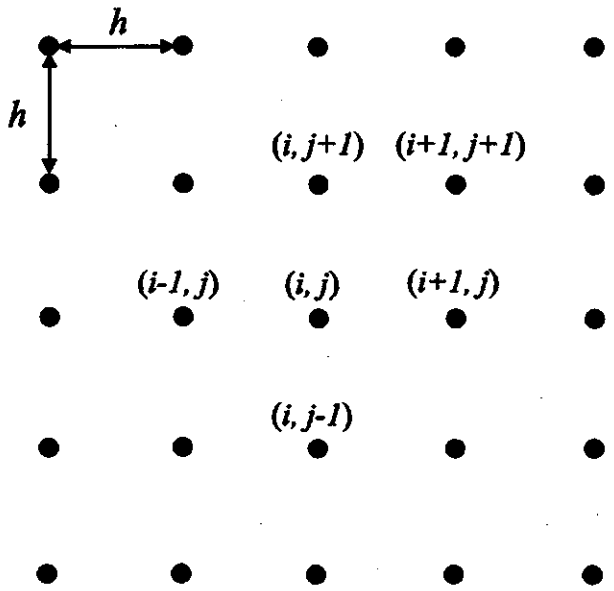

Figure 3.2 Mesh of points in two dimensions

Concentrating on the value of the function f at the mesh points and in a sense ignoring the values at other points, functions of discrete indices are then defined by

$$F(i,j) = f(ih, jh). \tag{3.21}$$

If the complexity of the field varies over the region of interest, a nonuniform mesh may be desirable.

The finite-difference approximation for the Laplacian of a function of two variables is

$$\frac{\partial^2 f}{\partial x^2} + \frac{\partial^2 f}{\partial y^2} = \frac{f(x+h,y) - 2f(x,y) + f(x-h,y)}{h^2} + \frac{f(x,y+h) - 2f(x,y) + f(x,y-h)}{h^2}$$

$$= \frac{f(x+h,y) + f(x-h,y) + f(x,y+h) + f(x,y-h) - 4f(x,y)}{h^2}, \tag{3.22}$$

which in discrete terms is

$$\nabla^2(i,j) = \frac{F(i+1,j)+F(i-1,j)+F(i,j+1)+F(i,j-1)-4F(i,j)}{h^2}. \qquad (3.23)$$

Use of this approximation with Laplace's equation

$$\frac{\partial^2 f}{\partial x^2}+\frac{\partial^2 f}{\partial y^2}=0, \qquad (3.24)$$

results in the discrete equation

$$F(i-1,j)+F(i+1,j)+F(i,j+1)+F(i,j-1)-4F(i,j)=0. \qquad (3.25)$$

If one such equation is written for each unknown value of F, a set of linear algebraic equations results.

3.2.2 Boundary conditions

If the function f is specified on the boundary, a boundary condition known as the Dirichlet condition, the value of F is specified on all the boundary points. With this condition it is desirable to satisfy Equation (3.25) at each internal point. If the internal point at which it is to satisfy Equation (3.25) adjoins a boundary point, some of the functional values in this equation are known.

Another frequently encountered boundary condition is the Neumann condition, where the normal derivative is specified and frequently set to the value zero. In Figure 3.3, the point (i, j) is a boundary point where the Neumann condition

$$\frac{\partial f}{\partial x}=0 \qquad (3.26)$$

is to be satisfied. Because the functional value $F(i, j)$ is unknown, Equation (3.25) must be used at this point. This requires a value for $F(i+1, j)$, but the point $(i+1, j)$ is outside

the computation region, and thus the functional value $F(i+1, j)$ is not available. The boundary condition (3.26) and Equation (3.14) lead to

$$F(i+1,j) = F(i-1,j), \tag{3.27}$$

and it is possible to use this relation to replace the value for the point outside the computation region. Then Equation (3.25) would be replaced by

$$2F(i-1,j) + F(i,j+1) + F(i,j-1) - 4F(i,j) = 0. \tag{3.28}$$

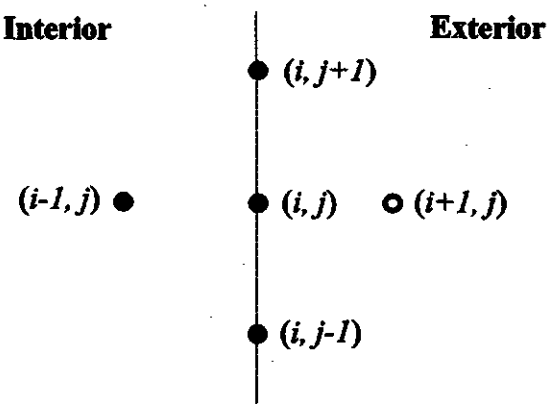

Figure 3.3 Neumann boundary condition

3.2.3 Iterative methods

At each node in the domain of the problem, the field values satisfy either equation (3.25) or (3.28). This gives rise to a set of linear algebraic equations. The set of linear algebraic equations can be solved directly, but even moderately small values of points may result in so many unknowns that direct solution is not feasible. Iterative, or indirect, methods have been found to be preferable for most two- and three-dimensional problems. For such a solution, write (3.25) in the form

$$F(i,j) = \frac{F(i+1,j) + F(i-1,j) + F(i,j+1) + F(i,j-1)}{4}. \tag{3.29}$$

The process of iteration starts with some initial values $F^0(i,j)$ for the unknown values, and cycles repeatedly through all (i,j) pairs that correspond to unknown values of F, and uses (3.29) in the form

$$F^1(i,j)=\frac{F^0(i+1,j)+F^0(i-1,j)+F^0(i,j+1)+F^0(i,j-1)}{4}. \qquad (3.30)$$

Equation (3.30) can be used to calculate an improved set of values $F^1(i,j)$. Then a second set of values can be calculated, and so on, using the general formula

$$F^n(i,j)=\frac{F^{n-1}(i+1,j)+F^{n-1}(i-1,j)+F^{n-1}(i,j+1)+F^{n-1}(i,j-1)}{4}, \qquad (3.31)$$

where, as before, the superscript indicates the number of the iteration. This process can be continued until the solution has converged to suitable accuracy. Because the change from one step of the iteration to the next may involve slight changes in the functional values, convergence is difficult to detect by examining successive steps. A safer procedure is to double the number of iterations successively and examine the changes after 1, 2, 4, 8, and so on, steps of iteration. When these numbers change little, it is safe to assume that the process has converged.

The process of iterating by repeatedly using the same equations for the nodal values is known as relaxation. An improvement that speeds the convergence process is known as over relaxation, and for the example of Laplace's equation replaces Equation (3.31) by

$$F^n(i,j)=F^{n-1}(i,j)$$
$$+R\left[\frac{F^{n-1}(i+1,j)+F^{n-1}(i-1,j)+F^{n-1}(i,j+1)+F^{n-1}(i,j-1)}{4}-F^{n-1}(i,j)\right]. \qquad (3.32)$$

If the constant R, known as the relaxation parameter, is equal to unity, the regular relaxation process results. Values of R greater than unity speed convergence, but too large a value of R results in numerical instability. For Laplace's equation, a value of 2 gives instability, and values near 1.5 are shown to give good results. It can be tested in the program to get the optimum value of R.

In calculating the functional values for one iteration step, only the values from the preceding step are used, which is an iterative process called the Jacobi process. For the first calculation in each step, that is all that can be done. For the second iteration, there is a choice, because the first calculation has given a more accurate value for one of the numbers. The iterative process that always uses the most recent numbers available is known as the Gauss-Seidel Method. The Gauss-Seidel Method can be shown to converge faster for a wide range of problems, and in addition, is easier to program since it is not necessary to store more than one value for each unknown.

The initial set of values $F^0(i,j)$ required to start the iterative process can be chosen arbitrarily as all zero or all unity. Convergence to the desired solution occurs faster if starting the process with a set of initial values that are reasonably close to the final values.

3.3 The Finite Element Method (FEM)

The basic concept of the finite element method is that although the behavior of a function may be complex when viewed over a large region, a simple approximation may suffice for a small subregion. The total region is divided into a number of nonoverlapping subregions called finite elements [29-32]. In two dimensions, polygons are usually used,

and the simplest polygons are triangles and squares. Figure 3.4a shows a region divided into squares and Figure 3.4b shows the same region divided into isoceles right triangles. Sometimes, as illustrated in Figure 3.4c, a combination of triangles and squares is useful. One of the advantages of using triangles is that a fairly arbitrary region can be more easily approximately covered by a set of triangles, as shown in Figure 3.4d.

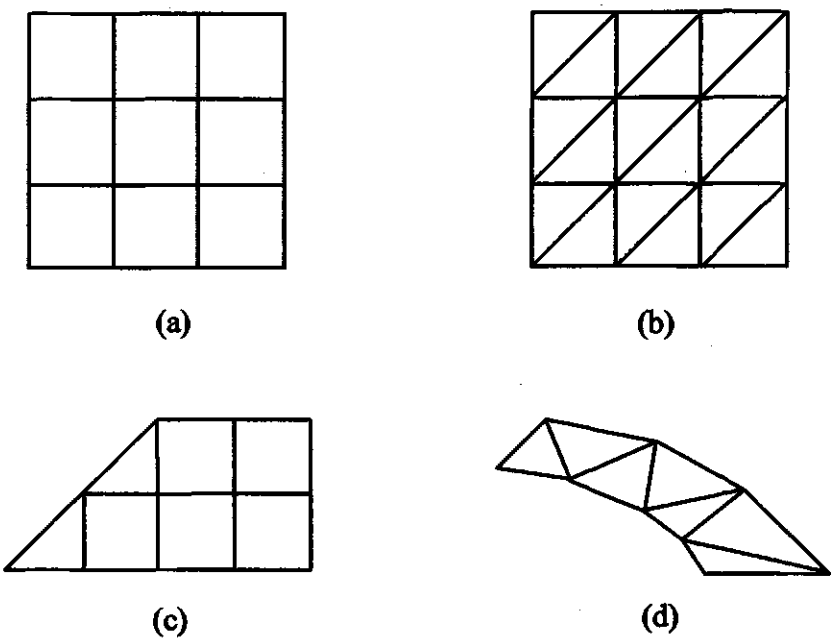

Figure 3.4 Division of regions: (a) Square elements; (b) Right isoceles triangles; (c) triangles and squares (d) Irregular region into triangles

In view of the fact that quadrilateral elements do not conform to a curved boundary as easily as triangular elements, it is preferable to use triangular elements throughout the analysis in this section.

Regardless of the shape of the elements, the field is approximated by a different expression over each element, but where the edges of adjoining elements overlap, the field representations must agree to maintain continuity of the field. The equations to be solved are usually stated not in terms of the field variables but in terms of an integral-type functional such as energy. The functional is chosen such that the field solution makes the functional stationary. The total functional is the sum of the integral over each element.

The finite element analysis of any problem involves basically four steps [27]:

- Discretizing the solution region into a finite number of subregions or elements called finite elements.
- Deriving governing equations for a typical element.
- Assembling all elements in the solution region, and
- Solving the system of equations obtained.

Next, apply the four steps mentioned above to solve Laplace's equation (3.11b),

$$\nabla^2 V = 0$$

3.3.1 Finite element discretization

To find the potential distribution $V(x, y)$ for the two-dimensional solution region shown in Figure 3.5a, divide the region into a number of finite elements named elements 1, 2, 3, ..., N, as illustrated in Figure 3.5b.

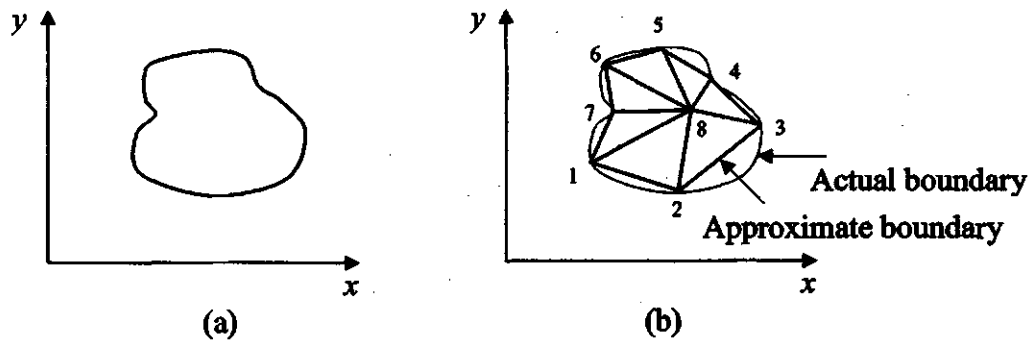

Figure 3.5 Illustration of the solution region and its finite element discretization

Next is to seek an approximation for the potential V_e within an element e and then to interrelate the potential distribution in various elements such that the potential is continuous across interelement boundaries. The approximate solution for the whole region is

$$V(x,y) \approx \sum_{e=1}^{N} V_e(x,y), \tag{3.33}$$

where N is the number of triangular elements into which the solution region is divided. The most common form of approximation for V within an element is polynomial approximation, namely,

$$V_e(x,y) = a + bx + cy, \tag{3.34}$$

for a triangular element. The constants a, b, and c are to be determined. The potential V_e in general is nonzero within element e but zero outside e.

3.3.2 Element governing equations

Consider a typical triangular element shown in Figure 3.6. The potential V_{e1}, V_{e2}, and V_{e3} at nodes 1, 2, and 3, respectively, are obtained using Equation (3.34), i.e.,

$$\begin{bmatrix} V_{e1} \\ V_{e2} \\ V_{e3} \end{bmatrix} = \begin{bmatrix} 1 & x_1 & y_1 \\ 1 & x_2 & y_2 \\ 1 & x_3 & y_3 \end{bmatrix} \begin{bmatrix} a \\ b \\ c \end{bmatrix}. \tag{3.35}$$

The coefficients a, b, and c are determined from Equation (3.35) as

$$\begin{bmatrix} a \\ b \\ c \end{bmatrix} = \begin{bmatrix} 1 & x_1 & y_1 \\ 1 & x_2 & y_2 \\ 1 & x_3 & y_3 \end{bmatrix}^{-1} \begin{bmatrix} V_{e1} \\ V_{e2} \\ V_{e3} \end{bmatrix}. \tag{3.36}$$

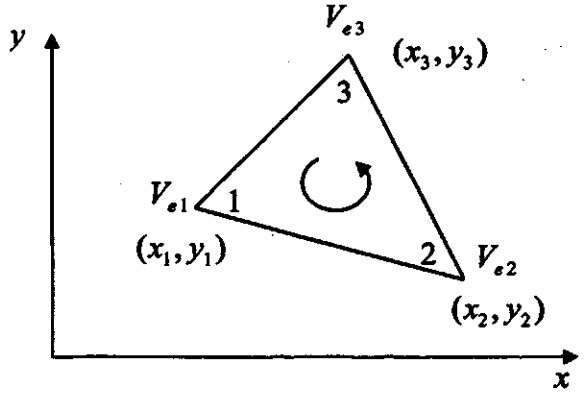

Figure 3.6 Typical triangular element

Substituting this into Equation (3.34) gives

$$V_e = \begin{bmatrix} 1 & x & y \end{bmatrix} \frac{1}{2A} \begin{bmatrix} (x_2y_3 - x_3y_2) & (x_3y_1 - x_1y_3) & (x_1y_2 - x_1y_3) \\ (y_2 - y_3) & (y_3 - y_1) & (y_1 - y_2) \\ (x_3 - x_2) & (x_1 - x_3) & (x_2 - x_1) \end{bmatrix} \begin{bmatrix} V_{e1} \\ V_{e2} \\ V_{e3} \end{bmatrix},$$

or

$$V_e = \sum_{i=1}^{3} \alpha_i(x,y)\, V_{ei}, \tag{3.37}$$

where

$$\alpha_1 = \frac{1}{2A}\left[(x_2y_3 - x_3y_2) + (y_2 - y_3)\, x + (x_3 - x_2)\, y\right], \tag{3.38a}$$

$$\alpha_2 = \frac{1}{2A}\left[(x_3y_1 - x_1y_3) + (y_3 - y_1)\, x + (x_1 - x_3)\, y\right], \tag{3.38b}$$

$$\alpha_3 = \frac{1}{2A}\left[(x_1y_2 - x_2y_1) + (y_1 - y_2)\, x + (x_2 - x_1)\, y\right], \tag{3.38c}$$

and A is the area of the element e, i.e.,

$$2A = \begin{vmatrix} 1 & x_1 & y_1 \\ 1 & x_2 & y_2 \\ 1 & x_3 & y_3 \end{vmatrix} = (x_1y_2 - x_2y_1) + (x_3y_1 - x_1y_3) + (x_2y_3 - x_3y_2),$$

or

$$A = \frac{1}{2}\left[(x_2 - x_1)(y_3 - y_1) - (x_3 - x_1)(y_2 - y_1)\right]. \tag{3.39}$$

The value of A is positive if the nodes are numbered counterclockwise (starting from any nodes) as shown by the arrow in Figure 3.6. Equation (3.37) gives the potential at any point (x, y) within the element provided that the potentials at the vertices are known, which is unlike finite difference analysis where the potential is known at the grid points only. α_i are linear interpolation functions that are called element shape functions.

The functional corresponding to Laplace's equation is given by

$$W_e = \frac{1}{2}\int \varepsilon |E|^2\, dS = \frac{1}{2}\int \varepsilon |\nabla V_e|^2\, dS. \tag{3.41}$$

Physically, the functional W_e is the energy per unit length associated with the element *e*.

From Equation (3.37),

$$\nabla V_e = \sum_{i=1}^{3} V_{ei} \nabla \alpha_i \,. \tag{3.42}$$

Substituting Equation (3.42) into Equation (3.41) gives

$$W_e = \frac{1}{2} \sum_{i=1}^{3} \sum_{j=1}^{3} \varepsilon V_{ei} \left[\int \nabla \alpha_i \cdot \nabla \alpha_j \, dS \right] V_{ej} \,. \tag{3.43}$$

If the term in brackets is defined as

$$C_{ij}^{(e)} = \int \nabla \alpha_i \cdot \nabla \alpha_j \, dS \,, \tag{3.44}$$

Equation (3.43) may be written in matrix form as

$$W_e = \frac{1}{2} \varepsilon [V_e]^t [C^{(e)}] [V_e] \,, \tag{3.45}$$

where the superscript *t* denotes the transpose of the matrix,

$$[V_e] = \begin{bmatrix} V_{e1} \\ V_{e2} \\ V_{e3} \end{bmatrix} , \tag{3.46a}$$

and

$$[C^{(e)}] = \begin{bmatrix} C_{11}^{(e)} & C_{12}^{(e)} & C_{13}^{(e)} \\ C_{21}^{(e)} & C_{22}^{(e)} & C_{23}^{(e)} \\ C_{31}^{(e)} & C_{32}^{(e)} & C_{33}^{(e)} \end{bmatrix} . \tag{3.46b}$$

The matrix $[C^{(e)}]$ is usually called the element coefficient matrix or stiffness matrix in structural analysis. The matrix element $C_{ij}^{(e)}$ of the coefficient matrix may be regarded as the coupling between nodes *i* and *j* ; its value is obtained from Equations (3.38) and (3.44):

$$C_{12}^{(e)} = \int \nabla\alpha_1 \cdot \nabla\alpha_2 \, dS$$

$$= \frac{1}{4A^2}\left[(y_2 - y_3)(y_3 - y_1) + (x_3 - x_2)(x_1 - x_3)\right] \int dS$$

$$= \frac{1}{4A}\left[(y_2 - y_3)(y_3 - y_1) + (x_3 - x_2)(x_1 - x_3)\right]. \tag{3.47a}$$

Similarly,

$$C_{13}^{(e)} = \frac{1}{4A}\left[(y_2 - y_3)(y_1 - y_2) + (x_3 - x_2)(x_2 - x_1)\right], \tag{3.47b}$$

$$C_{23}^{(e)} = \frac{1}{4A}\left[(y_3 - y_1)(y_1 - y_2) + (x_1 - x_3)(x_2 - x_1)\right], \tag{3.47c}$$

$$C_{11}^{(e)} = \frac{1}{4A}\left[(y_2 - y_3)^2 + (x_3 - x_2)^2\right], \tag{3.47d}$$

$$C_{22}^{(e)} = \frac{1}{4A}\left[(y_3 - y_1)^2 + (x_1 - x_3)^2\right], \tag{3.47e}$$

$$C_{33}^{(e)} = \frac{1}{4A}\left[(y_1 - y_2)^2 + (x_2 - x_1)^2\right], \tag{3.47f}$$

and

$$C_{21}^{(e)} = C_{12}^{(e)}, \tag{3.47g}$$

$$C_{31}^{(e)} = C_{13}^{(e)}, \tag{3.47h}$$

$$C_{32}^{(e)} = C_{23}^{(e)}. \tag{3.47i}$$

3.3.3 Assembling all elements

Having considered a typical element, the next step is to assemble all such elements in the solution region. The energy associated with the assemblage of elements is

$$W = \sum_{e=1}^{N} W_e = \frac{1}{2}\varepsilon [V]^t [C][V], \tag{3.48}$$

where

$$[V]=\begin{bmatrix} V_1 \\ V_2 \\ V_3 \\ \vdots \\ V_n \end{bmatrix}, \tag{3.49}$$

n is the number of nodes, N is the number of elements, and $[C]$ is called the overall or global coefficient matrix, which is the assemblage of individual element coefficient matrices.

So far it is assumed that the whole solution region is homogeneous so that ε is constant. For an inhomogeneous solution region, the region is discretized such that each finite element is homogeneous. In this case, Equation (3.41) still holds, but to apply Equation (3.48), replace ε by ε_0 and multiply the integrand in Equation (3.44), since ε ($=\varepsilon_0\varepsilon_r$) or simply ε_r varies from element to element.

3.3.4 Solving the resulting equations

Since Laplace's equation is satisfied when the total energy in the solution region is minimum [27], it is required that the partial derivatives of W with respect to each nodal value of the potential be zero, i.e.,

$$\frac{\partial W}{\partial V_1}=\frac{\partial W}{\partial V_2}=\cdots=\frac{\partial W}{\partial V_n}=0, \tag{3.50}$$

or

$$\frac{\partial W}{\partial V_k}=0, \qquad k=1,2,\cdots,n. \tag{3.51}$$

In general, this leads to

$$0 = \sum_{i=1}^{n} V_i C_{ik}, \tag{3.52}$$

where n is the number of nodes in the mesh. For all nodes, obtain a set of simultaneous equations from which the solution of $[V]^t = [V_1 \quad V_2 \quad \cdots \quad V_n]$ can be found. One of the methods for doing this is the iteration method.

In general, at node k in a mesh with n nodes from Equation (3.52), it is possible to obtain

$$V_k = -\frac{1}{C_{kk}} \sum_{i=1, i \neq k}^{n} V_i C_{ki}, \tag{3.53}$$

where node k is a free node. Since $C_{ki} = 0$ if node k is not directly connected to node i, only nodes that are directly linked to node k contribute to V_k in Equation (3.53). Equation (3.53) can be applied iteratively to all the free nodes. The iteration process begins by setting the potentials of fixed nodes (where the potentials are known) to their prescribed values and the potentials at the free nodes (where the potentials are unknown) equal to zero or to the average potential [33]

$$V_{ave} = \frac{1}{2}(V_{\min} + V_{\max}), \tag{3.54}$$

where $V_{\min}$ and $V_{\max}$ are the minimum and maximum values of V at the fixed nodes where the potential V is prescribed or known.

At the end of the first iteration, when the new values have been calculated for all the free nodes, they become the old values for the second iteration. The procedure is repeated until the change between subsequent iterations is negligible enough. All the iteration methods described in the finite difference method are applicable here.

3.4 The Transmission Line Matrix method (TLM)

The Transmission Line Matrix Method (TLM), otherwise known as the Transmission Line Modeling, is a numerical technique for solving field problems using circuit equivalence. It is based on the equivalence between Maxwell's equations and the equations for voltages and currents on a mesh of continuous two-wire transmission lines. The main feature of this method is the simplicity of formulation and programming for a wide range of applications [34]. As compared with the lumped network model, the transmission-line model is more general and performs better at high frequencies where the transmission and reflection properties of geometrical discontinuities cannot be regarded as lumped [35].

Like other numerical techniques, the TLM method is a discretization process. Unlike other methods such as finite difference and finite element methods, which are mathematical discretization approaches, the TLM is a physical discretization approach. In the TLM, the discretization of a field involves replacing a continuous system by a network or array of lumped elements.

The TLM method involves dividing the solution region into a rectangular mesh of transmission lines. Junctions are formed where the lines cross and form impedance discontinuities. A comparison between the transmission-line equations and Maxwell's equations allows equivalences to be drawn between voltages and currents on the lines and electromagnetic fields in the solution region. Thus, the TLM method involves two basic steps [36]:

- Replacing the field problem by the equivalent network and deriving analogy between the field and network quantities.

- Solving the equivalent network by iterative methods.

3.4.1 Transmission-line equations

Before applying the TLM method, it seems fitting to review briefly the basic concepts of transmission lines.

Consider an elemental portion of length Δl of a two-conductor transmission line. The equivalent circuit of the line is shown in Figure 3.7, where the line parameters R, L, G, and C are resistance per unit length, inductance per unit length, conductance per unit length, and capacitance per unit length, respectively. The model in Figure 3.7 may represent any two-conductor line and it is called the T-type equivalent circuit. Other types are possible, but will end up with the same set of equations. In the model of Figure 3.7, it is assumed without loss of generality that wave (voltage or current) propagates in the $+Z$ direction, from the generator to the load.

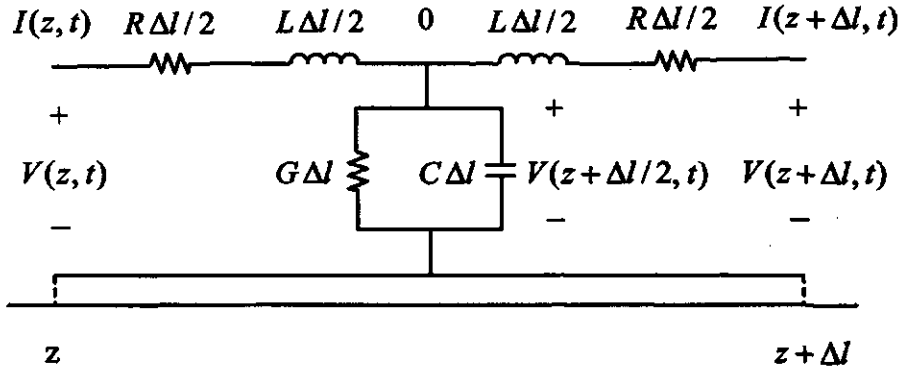

Figure 3.7 T-type equivalent circuit model of a differential length of a two-conductor transmission line

$$\frac{\partial^2 \Phi}{\partial z^2} = k_3 \frac{\partial^2 \Phi}{\partial t^2}, \tag{3.60}$$

where $k_3 = LC$. Equation (3.60) is called the Helmholtz equation, or simply the wave equation.

Thus, under certain conditions, the one-dimensional transmission line can be used to model problems involving an elliptic, parabolic, or hyperbolic partial differential equation (PDE).

3.4.2 Solution of wave equations

In order to show how Maxwell's equations may be represented by the transmission-line equations, the differential length of the lossless transmission line between two nodes of the mesh is represented by lumped inductors and capacitors as shown in Figure 3.8 for two-dimensional wave propagation problems [38-39]. At the nodes, pairs of transmission lines form impedance discontinuity. The complete network of transmission line matrices is made up of a large number of such building blocks as depicted in Figure 3.9, where single lines are used to represent a transmission line pair and a uniform internodal distance of Δl is assumed throughout the matrix (i.e., $\Delta l = \Delta x = \Delta z$).

In Figure 3.8, applying Kirchhoff's laws and taking the limit as $\Delta l \to 0$ following equations are obtained [27].

$$-\frac{\partial I_z}{\partial z} - \frac{\partial I_x}{\partial x} = 2C \frac{\partial V_y}{\partial t}, \tag{3.61a}$$

$$\frac{\partial V_y}{\partial x} = -L \frac{\partial I_x}{\partial t}, \tag{3.61b}$$

and

$$\frac{\partial V_y}{\partial z} = -L\frac{\partial I_z}{\partial t} \,. \tag{3.61c}$$

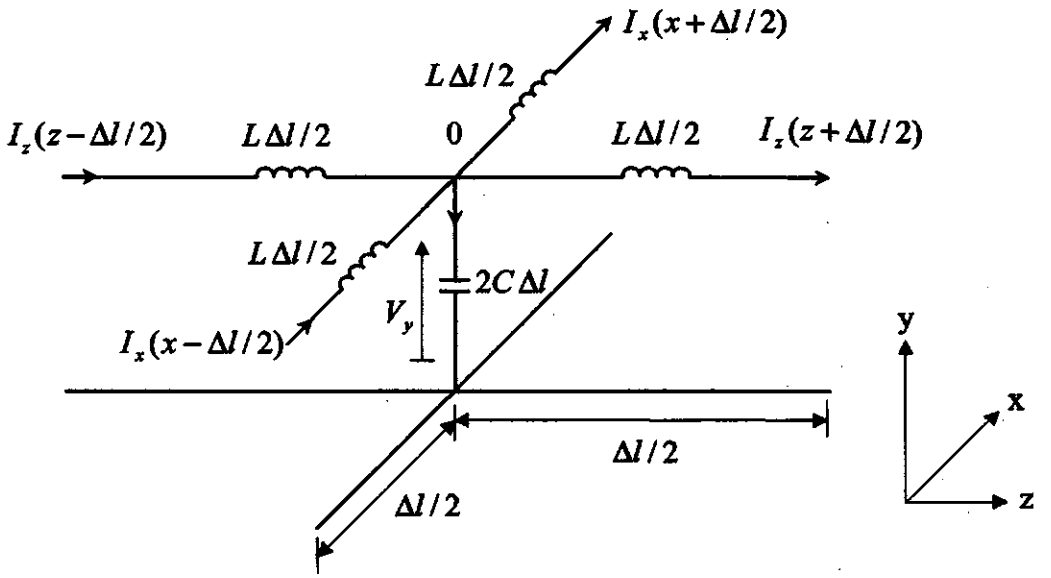

Figure 3.8 Equivalent network of a two-dimensional TLM shunt node

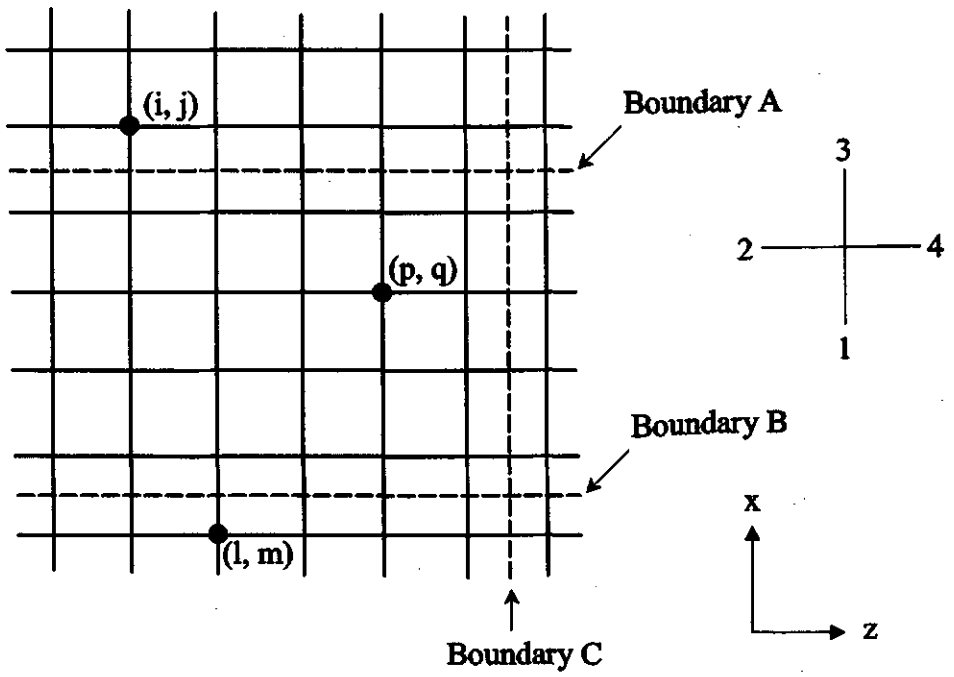

Figure 3.9 Transmission-line matrix and boundary

Differentiating Equation (3.61a) with respect to t, Equation (3.61b) with respect to x, and Equation (3.61a) with respect to z, yields

$$-\frac{\partial^2 I_z}{\partial z \partial t}-\frac{\partial^2 I_x}{\partial x \partial t}=2C\frac{\partial^2 V_y}{\partial t^2}\ , \tag{3.62a}$$

$$\frac{\partial^2 V_y}{\partial x^2}=-L\frac{\partial^2 I_x}{\partial t \partial x}\ , \tag{3.62b}$$

$$\frac{\partial^2 V_y}{\partial z^2}=-L\frac{\partial^2 I_z}{\partial t \partial z}\ . \tag{3.62c}$$

Substituting Equations (3.62b) and (3.62c) into Equation (3.62a) leads to

$$\frac{\partial^2 V_y}{\partial x^2}+\frac{\partial^2 V_y}{\partial z^2}=2LC\frac{\partial^2 V_y}{\partial t^2}\ . \tag{3.63}$$

Equation (3.63) is the Helmholtz wave equation in two-dimensional space.

In order to show the field theory equivalence of Equations (3.62) and (3.63), consider Maxwell's equations

$$\nabla\times E=-\mu\frac{\partial H}{\partial t}\ , \tag{3.64a}$$

and

$$\nabla\times H=\varepsilon\frac{\partial E}{\partial t}\ . \tag{3.64b}$$

Expansion of Equation (3.64) in the rectangular coordinate system yields

$$\frac{\partial E_z}{\partial y}-\frac{\partial E_y}{\partial z}=-\mu\frac{\partial H_x}{\partial t}\ , \tag{3.65a}$$

$$\frac{\partial E_x}{\partial z}-\frac{\partial E_z}{\partial x}=-\mu\frac{\partial H_y}{\partial t}\ , \tag{3.65b}$$

$$\frac{\partial E_y}{\partial x} - \frac{\partial E_x}{\partial y} = -\mu \frac{\partial H_z}{\partial t} \quad , \tag{3.65c}$$

$$\frac{\partial H_z}{\partial y} - \frac{\partial H_y}{\partial z} = \varepsilon \frac{\partial E_x}{\partial t} \quad , \tag{3.65d}$$

$$\frac{\partial H_x}{\partial z} - \frac{\partial H_z}{\partial x} = \varepsilon \frac{\partial E_y}{\partial t} \quad , \tag{3.65e}$$

$$\frac{\partial H_y}{\partial x} - \frac{\partial H_x}{\partial y} = \varepsilon \frac{\partial E_z}{\partial t} \quad . \tag{3.65f}$$

Consider the situation for which $E_x = E_z = H_y = 0$, $\frac{\partial}{\partial y} = 0$. It is noticed at once that this mode is a transverse electric (TE) mode with respect to the z-axis but a transverse magnetic (TM) mode with respect to the y-axis. Thus by the principle of duality, the network in Figure 3.8 can be used for E_y, H_x, H_z fields as well as E_x, E_z, H_y fields. A network capable of reproducing TE waves is also capable of reproducing TM waves. For TE waves, Equation (3.65) reduces to

$$\frac{\partial H_x}{\partial z} - \frac{\partial H_z}{\partial x} = \varepsilon \frac{\partial E_y}{\partial t} \quad , \tag{3.66a}$$

$$\frac{\partial E_y}{\partial x} = -\mu \frac{\partial H_z}{\partial t} \quad , \tag{3.66b}$$

$$\frac{\partial E_y}{\partial z} = \mu \frac{\partial H_x}{\partial t} \quad . \tag{3.66c}$$

Taking similar steps for Equations (3.66a – c) as were taken for Equations (3.61a – c) results in another Helmholtz equation

$$\frac{\partial^2 E_y}{\partial x^2} + \frac{\partial^2 E_y}{\partial z^2} = \mu\varepsilon \frac{\partial^2 E_y}{\partial t^2} \quad . \tag{3.67}$$

Comparing Equations (3.66) and (3.67) with Equations (3.61) and (3.63) yields the following equivalence between the parameters

$$E_y \equiv V_y \,, \tag{3.68a}$$

$$H_x \equiv -I_z \,, \tag{3.68b}$$

$$H_z \equiv I_x \,, \tag{3.68c}$$

$$\mu \equiv L \,, \tag{3.68d}$$

$$\varepsilon \equiv 2C \,. \tag{3.68e}$$

Thus in the equivalent circuit:

- the voltage at the shunt node is E_y,
- the current in the z direction is $-H_x$,
- the current in the x direction is H_z,
- the inductance per unit length represents the permeability of the medium,
- twice the capacitance per unit length represents the permittivity of the medium.

If ${}_kV_n^i$ and ${}_kV_n^r$ are the voltage impulses incident upon and reflected from terminal n of a node at time $t=k\Delta l/c$, derive the relationship between the two quantities as follows. Assume that a voltage impulse function of unit magnitude is launched into terminal 1 of a node, as shown in Figure 3.10, and that the characteristic resistance of the line is normalized. A unit-magnitude delta function of voltage and current will then travel towards the junction with unit energy ($S_i = 1$). Since line 1 has three other lines joined to it, its effective terminal resistance is 1/3. With the knowledge of its reflection coefficient,

both the reflected and transmitted voltage impulses can be calculated. The reflection coefficient is

$$\Gamma = \frac{R_L - R_o}{R_L + R_o} = \frac{1/3 - 1}{1/3 + 1} = -\frac{1}{2}, \tag{3.69}$$

so that the reflected and transmitted energies are

$$S_r = S_i \Gamma^2 = \frac{1}{4}, \tag{3.70a}$$

$$S_t = S_i (1 - \Gamma^2) = \frac{3}{4}, \tag{3.70b}$$

where subscripts *i*, *r*, and *t* indicate incident, reflected, and transmitted quantities, respectively. Thus a voltage impulse of −1/2 is reflected back in terminal 1, while a voltage impulse of $1/2 = [\frac{3}{4} + 3]^{1/2}$ will be launched into each of the other three terminals as shown in Figure 3.10.

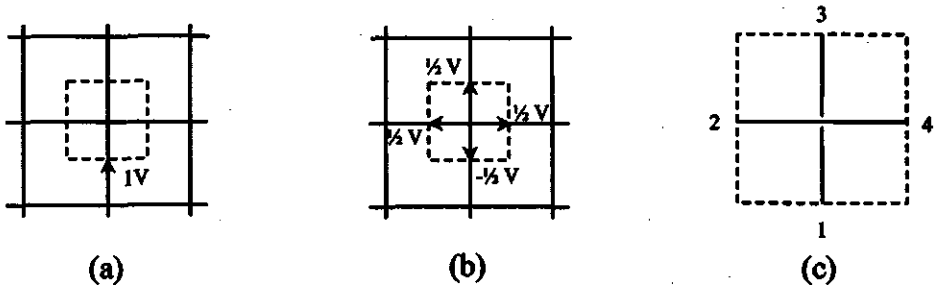

Figure 3.10 The impulse response of a node in a matrix

The more general case of four impulses being incident on four branches of a node can be obtained by applying the superposition principle to the previous case of a single pulse. Hence, if a time $t = k\Delta l / c$, voltage impulses ${}_kV_1^i$, ${}_kV_2^i$, ${}_kV_3^i$, and ${}_kV_4^i$ are incident

on lines 1 to 4, respectively, at any junction node as in Figure 3.10c, the combined voltage reflected along line 1 at time $t=(k+1)\Delta l/c$ will be [34, 38]

$$ {}_{k+1}V_1^r = \frac{1}{2}\left\langle {}_kV_2^i + {}_kV_3^i + {}_kV_4^i - {}_kV_1^i \right\rangle . \tag{3.71} $$

In general, the total voltage impulse reflected along line n at time $t=(k+1)\Delta l/c$ will be

$$ {}_{k+1}V_n^r = \frac{1}{2}\left[\sum_{m=1}^{4} {}_kV_m^i\right] - {}_kV_n^i . \qquad n=1,2,3,4. \tag{3.72} $$

This idea is conveniently described by a scattering matrix equation relating the reflected voltages at time $(k+1)\Delta l/c$ to the incident voltages at the previous time step $k\Delta l/c$:

$$ {}_{k+1}\begin{bmatrix} V_1 \\ V_2 \\ V_3 \\ V_4 \end{bmatrix}^r = \frac{1}{2}\begin{bmatrix} -1 & 1 & 1 & 1 \\ 1 & -1 & 1 & 1 \\ 1 & 1 & -1 & 1 \\ 1 & 1 & 1 & -1 \end{bmatrix} {}_k\begin{bmatrix} V_1 \\ V_2 \\ V_3 \\ V_4 \end{bmatrix}^i . \tag{3.73} $$

Also an impulse emerging from a node at position (z, x) in the mesh (reflected impulse) becomes automatically an incident impulse at the neighboring node. Hence

$$ {}_{k+1}V_1^i(z, x+\Delta l) = {}_{k+1}V_3^r(z,x) , \tag{3.74a} $$

$$ {}_{k+1}V_2^i(z+\Delta l, x) = {}_{k+1}V_4^r(z,x) , \tag{3.74b} $$

$$ {}_{k+1}V_3^i(z, x-\Delta l) = {}_{k+1}V_1^r(z,x) , \tag{3.74c} $$

$$ {}_{k+1}V_4^i(z-\Delta l, x) = {}_{k+1}V_2^r(z,x) . \tag{3.74d} $$

Thus by applying Equations (3.73) and (3.74), the magnitudes, positions, and directions of all impulses at time $(k+1)\Delta l/c$ can be obtained at each node in the network provided that their corresponding values at time $k\Delta l/c$ are known. The impulse response may, therefore, be found by initially fixing the magnitude, position, and

direction of travel of impulse voltages at time $t = 0$, and then calculating the state of the network at successive time intervals.

The propagation of pulses in the TLM model is illustrated in Figure 3.11, where the first two iterations following an initial excitation pulse in a two-dimensional shunt-connected TLM are shown. Free-space propagation has been assumed for the sake of simplicity. The scattering process forms the basic algorithm of the TLM method [34, 39].

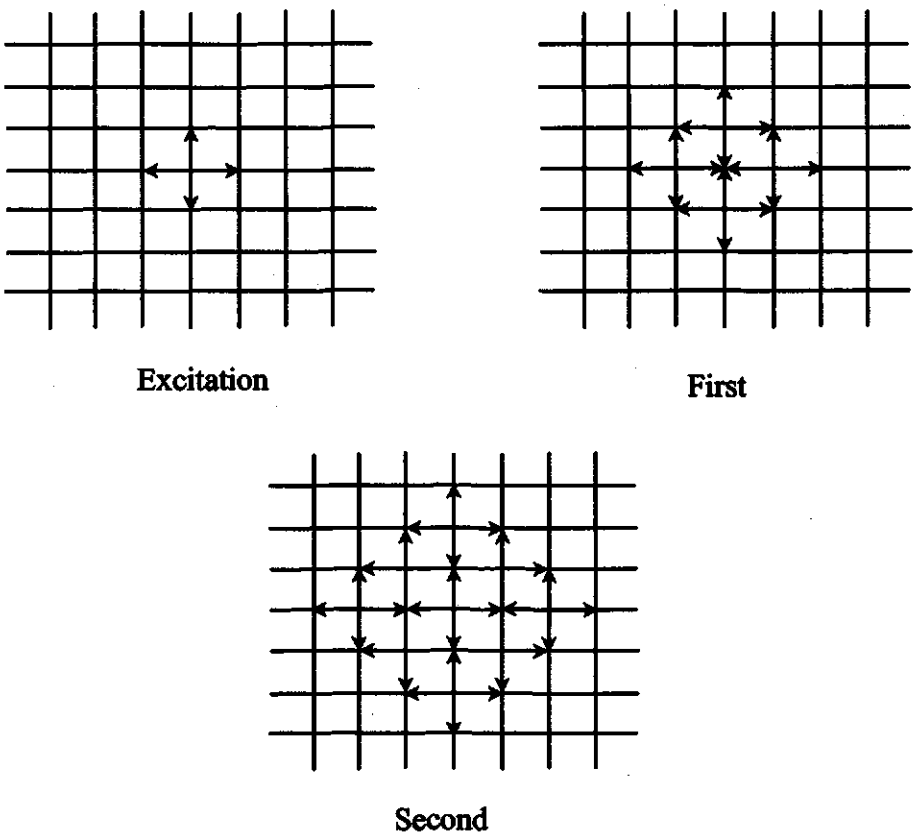

Figure 3.11 Scattering in a two-dimensional TLM network excited by a Dirac impulse

The TLM mesh considered so far is two-dimensional. By applying a hybrid TLM mesh consisting of three shunt and three series nodes to simultaneously describe all the six field components, the three-dimensional results can be also obtained [27].

The output impulse function, in terms of voltage or current, may be taken from any point in the TLM mesh. It consists of a train of impulses of varying magnitude in the time domain separated by a time interval $\Delta l / c$. Thus the frequency response obtained by taking the Fourier transform of the output response consists of series of delta functions in the frequency domain corresponding to the discrete modal frequencies for which a solution exits.

3.5 Chapter summary

In this chapter, three numerical methods for solving electromagnetic problems are discussed. The methods include the Finite Difference Method (FDM), the Finite Element Method (FEM) and the Transmission Line Matrix Method (TLM). These are the three methods used in the filter design of this research.

Chapter 4 The Design of the Filters

In Chapter 1 some fundamental concepts on filters are introduced. The design methods for bandpass and low-pass filters will be discussed in this chapter. The filters are formed by TEM-mode slab-line resonators and uniform non-TEM mode waveguide resonators.

4.1 Design of TEM mode ceramic block bandpass filters

In this section, a bandpass filter that is extensively used in cellular radio is described. The filter consists of quarter-wavelength coaxial resonators formed in a mono-block ceramic. Since the coupling between pairs of adjacent resonators is via an air hole, additional coupling elements are not needed. This structure effectively reduces the size and cost of the filters. The coupling coefficient can be analyzed by numerical solution of Laplace's equation for the electric potential. The most suitable numerical techniques are the Finite Element Method and the Finite Difference Method.

4.1.1 Filter configuration

Figure 4.1 shows a mono-block ceramic bandpass filter. The inner surfaces of the odd numbered holes of the bandpass filter are metalized. All surfaces of the block, except the upper wall, are silver-plated. The metalized holes act as inner conductors of a slab-

line resonator. The length of the resonator is adjusted to be a quarter-wavelength of the fundamental wave at the centre frequency of the filter. All of the resonators are short-circuited at one end and open-circuited at the other end. The number of resonators is decided by the filter's specifications (desired frequency response). Assume that there are five resonators in this case. Each resonator is coupled through a vacant air hole (the even holes in Figure 4.1) to the next resonator. Input and output couplings to the filter as shown in Figure 4.1 are accomplished by metal patch capacitors. The whole filter is made from a mono-block ceramic.

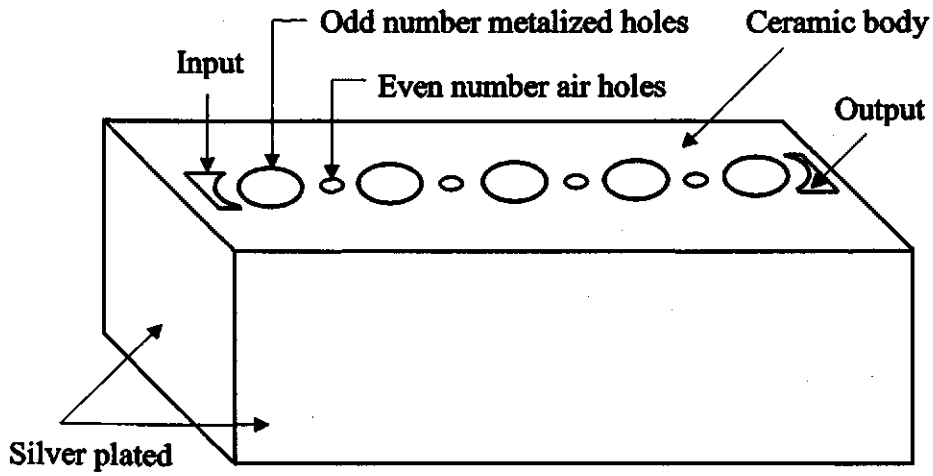

Figure 4.1 A mono-block ceramic bandpass filter configuration

Conventional designs of this kind of filter used two metal patches connected to the respective metal holes to form a planar capacitor to realise the coupling between adjacent resonators as shown in Figure 4.2. Such a structure has several disadvantages:

- The resonant frequency changes with the adjustment of the coupling capacitor. Therefore, the tuning of the filter is very difficult and time-consuming.
- There is no design theory. The design is done experimentally.
- The structure, especially that of the coupling capacitors, is very difficult to manufacture (the capacitors shown in Figure 4.2 are simplified and actual capacitors have a very complex shape). Therefore, all these add to developmental and production costs.

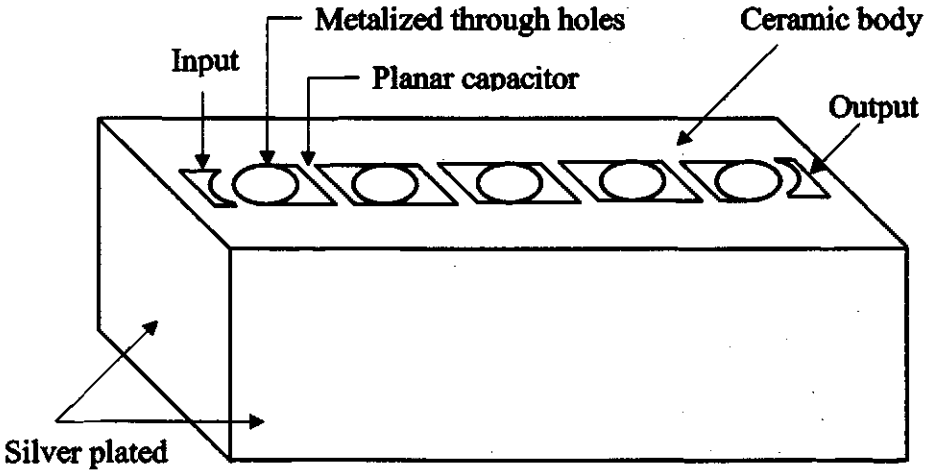

Figure 4.2 Illustration of the filter structure of conventional design

The filter structure shown in Figure 4.1 overcomes these disadvantages. The numerical methods introduced in Chapter 3 can be used to analyse the interresonator couplings to design the filter.

The equivalent circuit diagram of the filter is shown in Figure 4.3. Every quarter-wavelength resonator corresponds to a parallel resonant circuit (L_i, C_i, $i = 1 - 5$). The

coupling holes provide inductive coupling (coupling inductances L_{ij}) between adjacent resonators. The external terminations and the two outermost quarter-wavelength resonant circuits are also coupled to each other through capacitive couplings (C_{in}, C_{out}).

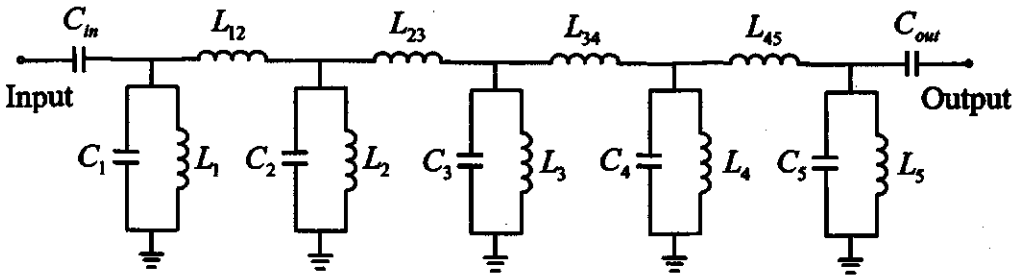

Figure 4.3 The equivalent circuit for a mono-block ceramic bandpass filter

4.1.2 Filter synthesis

Several methods are available for designing microwave filters. Of these, the low-pass prototype filter based synthesis method, which predates computers, has been most successful. However, it focuses on special cases that allow the use of analytic solutions under highly idealized conditions. Despite drawbacks, this technique has been the basis for the vast majority of filter designs. Furthermore, traditional design is the starting point for the second type of design using numerical methods. Therefore, it is natural to start with a discussion of the traditional approach to obtain the element values for a prototype low-pass filter.

A prototype low-pass filter is shown in Figure 4.4. There are actually an unlimited number of different solutions to the low-pass prototype design. In this thesis, the focus

will be put on the one that has been applied the most: equal-ripple (Chebyshev) response, as shown in Figure 1.6b in Chapter 1.

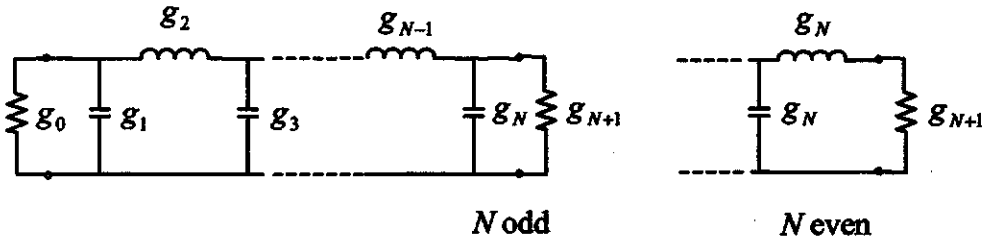

Figure 4.4 Prototype low-pass filter

Using the insertion-loss method, the g_k values for the Chebyshev response in Figure 4.4 can be calculated from the following equations [5]:

$$g_0 = 1\,, \tag{4.1a}$$

$$g_1 = \frac{2a_1}{\xi}\,, \tag{4.1b}$$

$$g_k = \frac{4a_{k-1}a_k}{b_{k-1}g_{k-1}}\,, \qquad k = 2, 3, \cdots, N\,, \tag{4.1c}$$

$$g_{k+1} = \begin{cases} 1, & N\ odd \\ \tanh^2\dfrac{\beta}{4}, & N\ even \end{cases}\,, \tag{4.1d}$$

where

$$a_k = \sin\frac{(2k-1)\pi}{2N}\,, \qquad k = 1, 2, \cdots, N\,, \tag{4.1e}$$

$$b_k = \xi^2 + \sin^2\frac{k\pi}{N}\,, \qquad k = 1, 2, \cdots, N\,, \tag{4.1f}$$

$$\beta = \ln\left(\coth\frac{A_m}{17.37}\right), \tag{4.1g}$$

$$\xi = \sinh\frac{\beta}{2N}, \tag{4.1h}$$

A_m is the amplitude of the ripple. N is the order of the filter or the number of resonators, which is determined by [40]

$$N \geq \frac{L_A + RL + 6}{20\log(\gamma + \sqrt{\gamma^2 - 1})}, \tag{4.1i}$$

where, γ is the ratio $\Delta f_i/\Delta f$ (Δf is the ripple bandwidth, Δf_i is the isolation bandwidth), RL is the passband return loss, and L_A is the stop band isolation of the filter.

The next step in the design procedure is finding the necessary normalized coupling coefficients in terms of low-pass prototype element values and design frequencies as follows [5]:

$$K^c_{n,n+1} = \frac{\Delta f}{f_0\sqrt{g_n g_{n+1}}}, \tag{4.2}$$

where Δf is the equal ripple bandwidth for Chebyshev response, f_0 is the centre frequency of the proposed filter, and g_n are the low-pass prototype element values.

4.1.3 Modelling of the coupling using numerical method

The cross section of coupled lines used in a round-rod TEM-mode slab-line ceramic block filter, including vacant holes, is shown in Figure 4.5. For analysis of the field on the resonator, a periodic arrangement of uniform coupled transmission lines is

assumed. Uniform is intended to mean that the cross-section of the set of coupled lines is the same throughout this section. To characterise this structure accurately, it is necessary to resort to numerical analysis. The Finite Difference Method and Finite Element Method are simple and versatile for solving the coupling problem on the resonators. Using the odd-even mode technique discussed in Section 1.1.3, the voltage distribution over the two coupled line regions can be obtained. Then the electric field can be found which will lead to the estimation of the line capacitance and the effective dielectric constant. The coupling coefficient can be calculated using [41]

$$K^c = 2\frac{f_{0,o} - f_{0,e}}{f_{0,o} + f_{0,e}}, \tag{4.3}$$

where $f_{0,o}$ and $f_{0,e}$ are the resonant frequencies of the odd mode and the even mode, respectively.

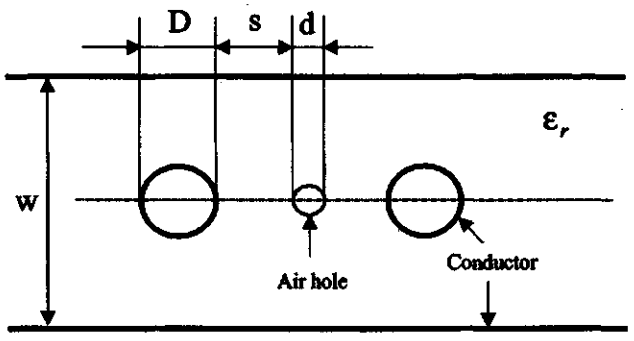

Figure 4.5 A cross section of coupled lines for numerical analysis

Equation 4.3 can be transformed into

$$K^c = 2\frac{\sqrt{\varepsilon_{r,e}} - \sqrt{\varepsilon_{r,o}}}{\sqrt{\varepsilon_{r,e}} + \sqrt{\varepsilon_{r,o}}}, \tag{4.4}$$

where $\varepsilon_{r,o}$ and $\varepsilon_{r,e}$ are odd mode and even mode effective dielectric constants [41], respectively.

If $\varepsilon_{r,e} = \varepsilon_{r,o}$, the coupling coefficient $K^c = 0$. However, in this case, $\varepsilon_{r,e}$ and $\varepsilon_{r,o}$ are not equal to each other due to the vacant hole between any two consecutive resonators. The difference between $\varepsilon_{r,e}$ and $\varepsilon_{r,o}$ results in the coupling of the resonators.

The effective dielectric constant for the coupled resonators is expressed as

$$\varepsilon_{r,eff} = \frac{\varepsilon_{r,e} + \varepsilon_{r,o}}{2} . \tag{4.5}$$

And the centre frequency (or the resonant frequency) f_0 is given by

$$f_0 = \frac{c}{\lambda_g \sqrt{\varepsilon_{r,eff}}} = \frac{c}{4L\sqrt{\varepsilon_{r,eff}}} , \tag{4.6}$$

where c is the velocity of light in free space, λ_g is the guide wavelength, and L is the length of the coupled resonators. Thus, the height of the ceramic block of the filter is determined by

$$H = L = \frac{\lambda_0}{4\sqrt{\varepsilon_{r,eff}}} = \frac{\lambda_g}{4} . \tag{4.7}$$

A good estimation of insertion loss is given by [42]

$$IL_0 = \frac{4.343}{\left(\frac{\Delta f}{f_0}\right)} \sum_{i=1}^{N} \frac{g_i}{Q_{u,i}} , \tag{4.8}$$

where IL_0 is the insertion loss at centre frequency (dB), and $Q_{u,i}$ is *i-th* resonator's unloaded Q. The desired quality factor of the resonator determines the widths and length of the ceramic block, though usually they are determined by experiment.

From Figure 4.5, it is known that the coupling coefficient changes with the distance s between metal hole and air hole or the diameter of the air hole, provided the other parameters of the block are fixed. Thus the curve of coupling coefficient versus distance s can be obtained if the diameter of the air hole is fixed, as shown in Figure 4.6, by numerical analysis. This curve can be used as the data in the design of the filter.

Figure 4.6 Coupling coefficient versus distance s

4.2 Design of the round-rod waveguide bandpass filters

In the previous section TEM-mode ceramic block bandpass filters are discussed. Such filters' performance is limited by a low Q-factor and high loss. On the contrary, waveguides offer a high Q-factor and low loss. In addition, waveguide filters can handle power levels that cannot be reached by slab-line filters.

The filter synthesis method discussed in this section is based on distributed transmission line theory and the conventional low frequency network theory. It determines the geometrical dimension of each coupling round rod and the distance between two consecutive resonators in the waveguide filter structure. The design

procedure relies greatly on the accurate characterization of the waveguide discontinuities inherent in these types of filters.

4.2.1 The design approach according to Matthaei, Young and Jones' handbook [4]

Consider the half-wave waveguide resonator coupled bandpass filter configurations shown in Figure 4.7. Figure 4.8 shows the K-inverter equivalent network of the Filter shown in Figure 4.7. According to the design outlined in Matthaei, Young, and Jones' handbook, the design procedure is as follows [4].

The fractional bandwidth in a waveguide filter is defined as $w_\lambda = \dfrac{\lambda_{gL} - \lambda_{gH}}{\lambda_{g0}}$, where λ_{gL}, λ_{gH} and λ_{g0} are the guided wavelengths at the lower cutoff, upper cutoff, and the centre frequencies, respectively, of the filter.

Once the fractional bandwidth is known, the normalized K-inverter values are obtained from

$$\frac{K_{01}}{Z_0} = \sqrt{\frac{\pi w_\lambda}{g_0 g_1}}, \tag{4.9}$$

$$\frac{K_{j,j+1}}{Z_0} = \frac{\pi w_\lambda}{2\sqrt{g_j g_{j+1}}}, \qquad j = 1, 2, 3, ..., N\text{-}1, \tag{4.10}$$

and

$$\frac{K_{N,N+1}}{Z_0} = \sqrt{\frac{\pi w_\lambda}{2 g_N g_{N+1}}}, \tag{4.11}$$

where $g_1, g_2, \ldots, g_{N+1}$ are the low-pass prototype parameters, and (see Figure 4.8b),

$$Z_0 = R_1 = R_2 . \tag{4.12}$$

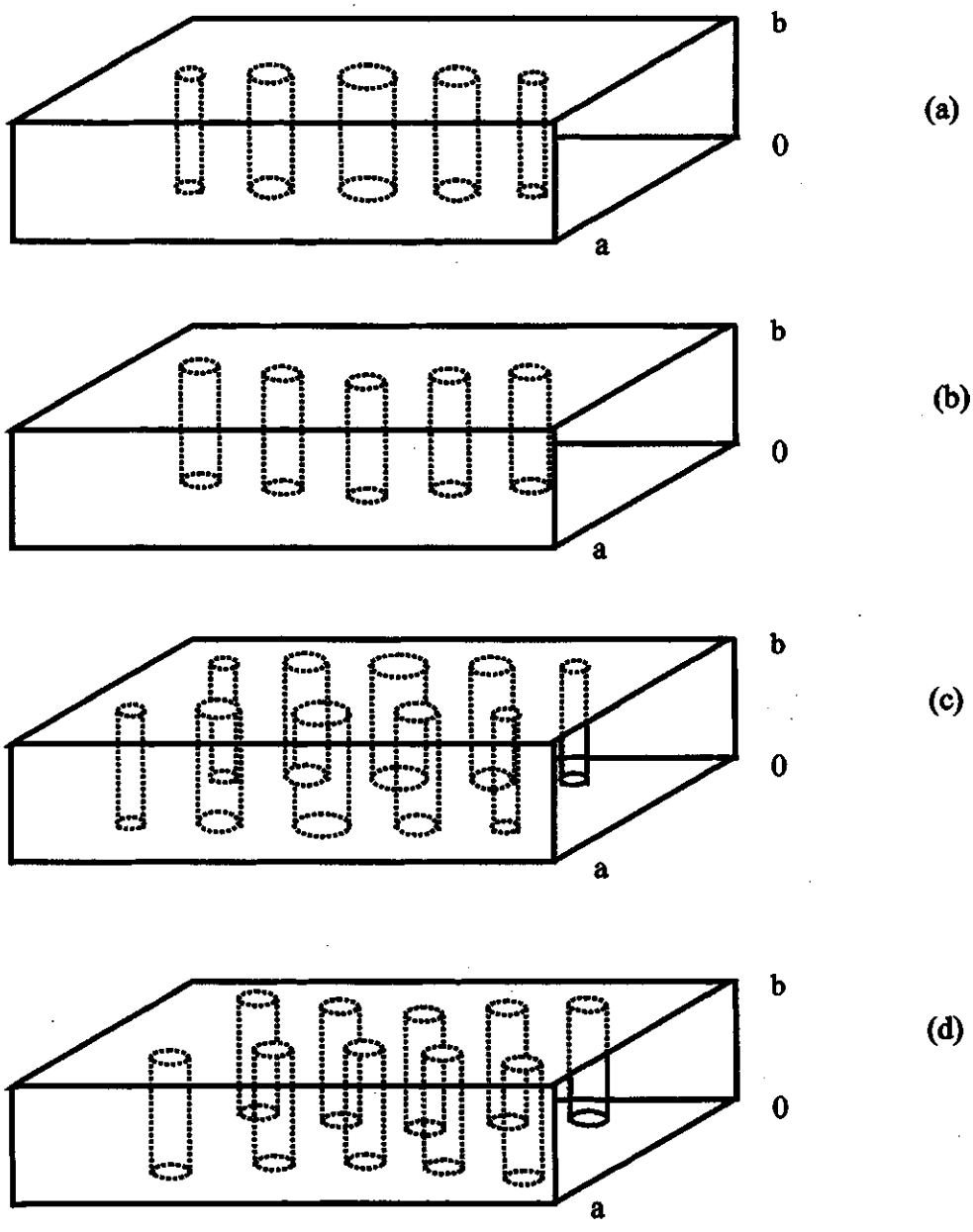

Figure 4.7 Various round rod waveguide filters: (a) Single rod with variable diameter, (b) Single rod with constant diameter, (c) Double rods with variable diameters, and (d) Double rods with variable diameters

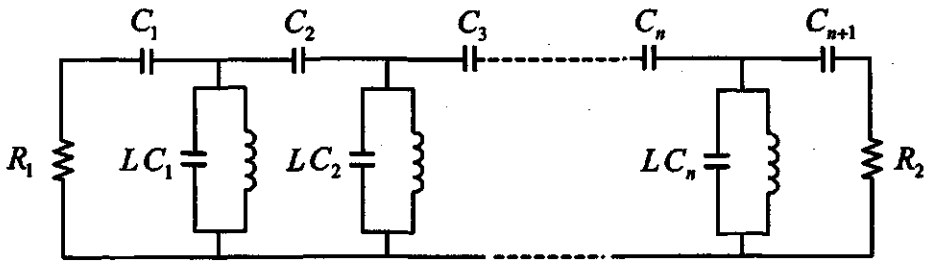

(a)

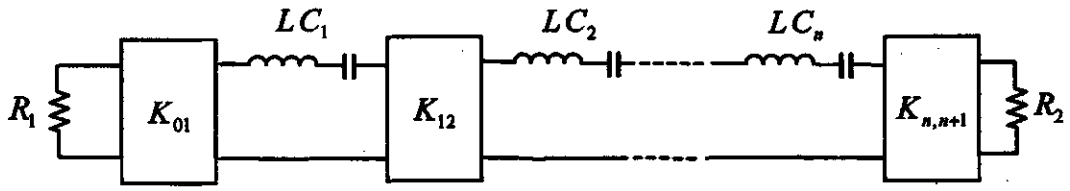

(b)

Figure 4.8 Equivalent network of the filters in Figure 4.7: (a) bandpass filter prototype, (b) bandpass filter containing impedance inverter

For purely lumped-inductance discontinuities having shunt reactance $X_{j,j+1}$, shown in Figure 4.9,

$$\frac{X_{j,j+1}}{Z_0} = \frac{\dfrac{K_{j,j+1}}{Z_0}}{1-\left(\dfrac{K_{j,j+1}}{Z_0}\right)^2}, \tag{4.13}$$

and

$$\theta_j = \pi - \frac{1}{2}\left[\tan^{-1}\left(\frac{2X_{j-1,j}}{Z_0}\right) + \tan^{-1}\left(\frac{2X_{j,j+1}}{Z_0}\right)\right], \tag{4.14}$$

where θ_j, ($j = 1, 2, ..., N$) are the electrical lengths of the resonators.

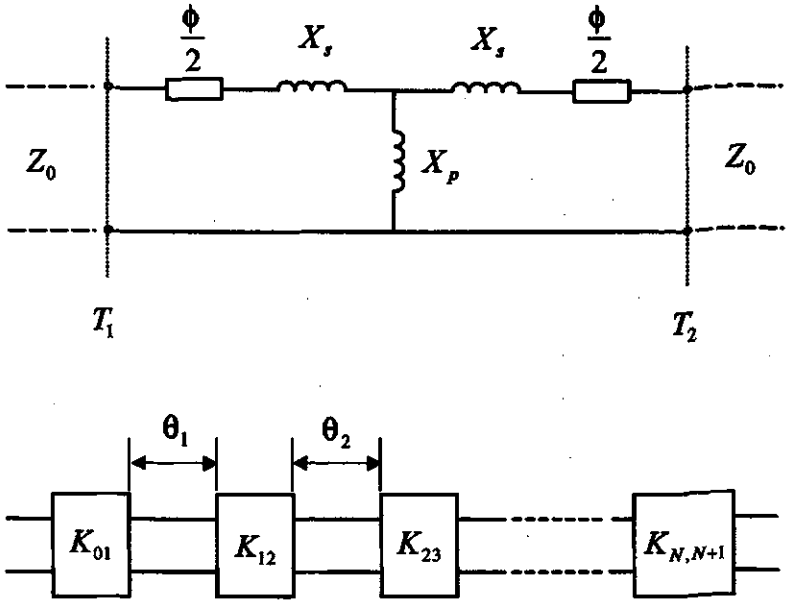

Figure 4.9. Lumped element equivalent network of a discontinuity

The designer may choose any suitable type of waveguide discontinuities in order to realize the required K inverters. A few typical discontinuities and the equivalent scattering matrix networks are shown in Figure 4.10.

The handbook of Matthaei, Young, and Jones [4] provides graphs which directly relate the K-inverter values to the rod diameter in the case of a centrally located single rod filter shown in Figure 4.10a. The main disadvantage of this structure is that the diameters of the rods have to be varied depending upon the required K-inverter value to be realized. However, the same goal can be achieved by using a constant rod diameter for all K inverters as shown in Figure 4.10c, where the rods are not symmetrically located.

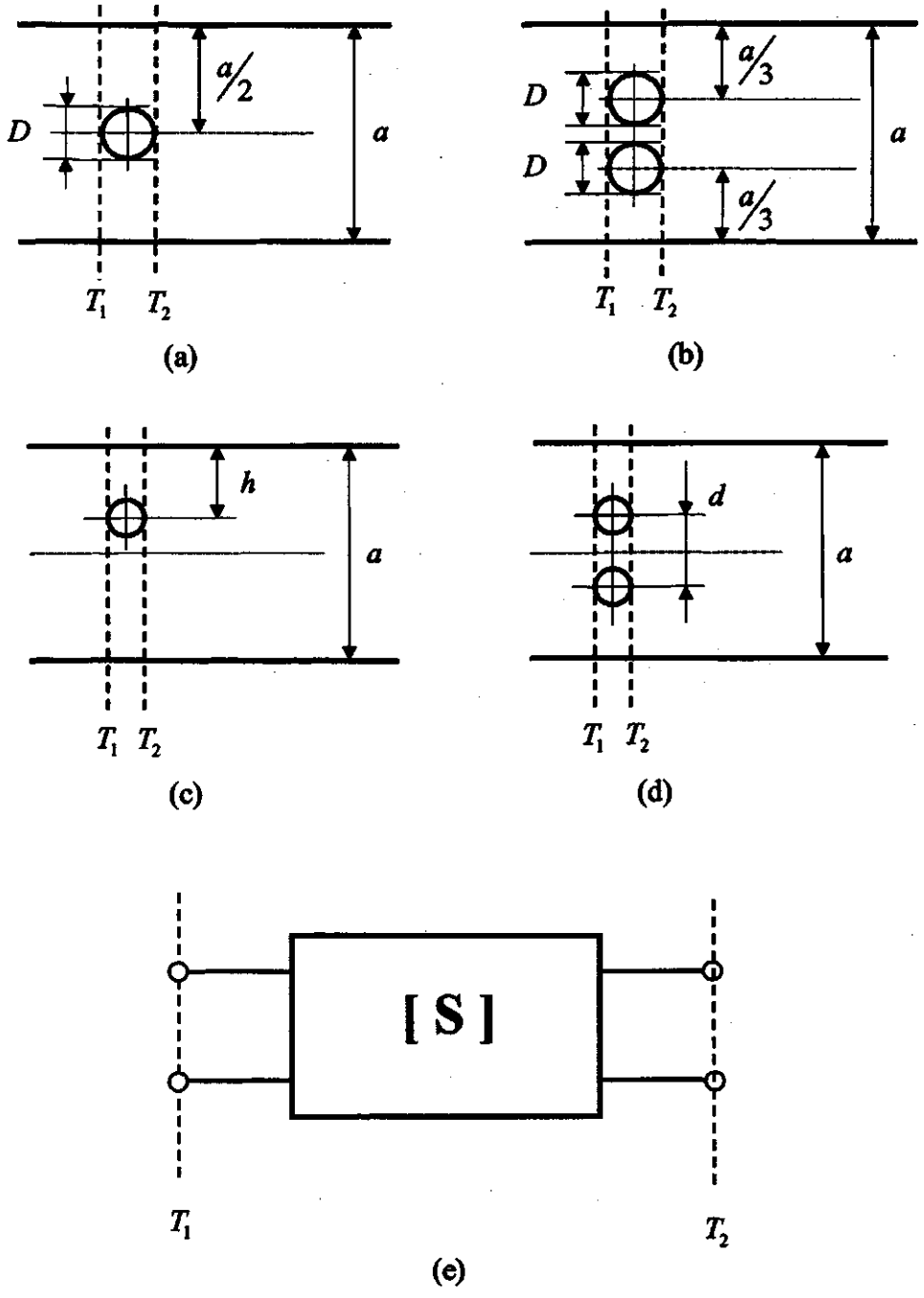

Figure 4.10. Various round rod discontinuities and the S-matrix two-port network

Unfortunately, no design curve is currently available for the structure shown in Figure 4.10b, 4.10c and 4.10d, which can be used directly to realize the K-inverters. In addition, a simple mode matching technique cannot be used to solve for the scattering matrices of the discontinuities because of the associated complexity of the mixed coordinate system (rectangular for the waveguide and circular cylindrical for the posts). The equations for K-inverters presented in Matthaei, Young, and Jones' book [4] have limitations that do not take into consideration the frequency dependence of the waveguide discontinuities.

4.2.2 The full-wave 3-D modeling based approach with distributed element K-inverters of Levy and Rhodes

A viable option is the full electromagnetic modelling of an off-centered round post discontinuity in a rectangular waveguide. A number of papers have appeared in the literature that deal with such analysis [43]. At the same time, there exist, today, some very accurate full electromagnetic analysis based commercially available software that can be used to generate the design model for the K-inverters for the filter configurations shown in Figure 4.7. The Transmission Line Matrix analysis based software Micro-Stripes [6] is used to develop the model for the K-inverters for the round rod discontinuities shown in Figure 4.10. The required K-inverter values are calculated for the filters using the distributed element prototype network by Levy [43] and Rhodes [40].

According to [43] and [40] the required K-inverter values for a filter are obtained as described in the following text:

1) The order of the filter, N, will give the number of resonators and $N+1$ will be the number of rod couplers needed to meet the design specifications. N is determined from the ripple bandwidth Δf, the isolation bandwidth Δf_i, the passband return loss RL and the stop band isolation L_A of the filter using the following equation for a Chebyshev type response. The filter order is given by [40]. Thus,

$$N \geq \frac{L_A + RL + 6}{20 \log(\gamma + \sqrt{\gamma^2 - 1})}, \tag{4.15a}$$

where γ is the ratio $\Delta f_i / \Delta f$.

2) The midband guide wavelength λ_{g0} is determined by solving [43],

$$\lambda_{gL} \sin\left(\frac{\pi \lambda_{g0}}{\lambda_{gL}}\right) + \lambda_{gH} \sin\frac{\pi \lambda_{g0}}{\lambda_{gH}} = 0, \tag{4.15b}$$

where λ_{gL} and λ_{gH} are the guide wavelengths in the resonator section at the lower and upper cut-off frequencies, respectively, of the filter. For a narrow-band case,

$$\lambda_{g0} \approx \frac{\lambda_{gL} + \lambda_{gH}}{2}. \tag{4.15c}$$

A suitable numerical method is used for solving equation (4.15b).

3) A scaling parameter is given by

$$\alpha = \frac{\lambda_{g0}}{\lambda_{gL} \sin(\frac{\pi \lambda_{g0}}{\lambda_{gL}})}. \tag{4.15d}$$

4) The impedance Z_n of the distributed elements and the impedance inverter values $k'_{n,n+1}$ are given by

$$Z_n = \frac{2\alpha \sin\left[\frac{(2n-1)\pi}{2N}\right]}{y} - \frac{1}{4y\alpha}\left\{\frac{y^2+\sin^2\left(\frac{n\pi}{N}\right)}{\sin\frac{(2n+1)\pi}{2N}} + \frac{y^2+\sin^2\left[\frac{(n-1)\pi}{N}\right]}{\sin\frac{(2n-3)\pi}{2N}}\right\},$$

$$n = 1, 2, ..., N, \qquad (4.15e)$$

$$k'_{n,n+1} = \frac{\sqrt{y^2+\sin^2\left(\frac{n\pi}{N}\right)}}{y}, \qquad (4.15f)$$

where

$$y = \sinh\left[\frac{1}{N}\sinh^{-1}\frac{1}{\varepsilon_p}\right], \qquad (4.15g)$$

and ε_p is the factor that determines the passband ripple level of the filter.

5) The normalised K-inverter values which are to be realised by the waveguide rod discontinuities for the filter are defined by

$$K_{n,n+1} = \frac{k'_{n,n+1}}{\sqrt{Z_n Z_{n+1}}}, \qquad n = 0, ..., N, \qquad (4.15h)$$

and

$$Z_0 = Z_{N+1} = 1. \qquad (4.15i)$$

Once the required K-inverter values have been calculated from the preceding equations, they can be physically realized in terms of discontinuities in a rectangular waveguide. However, as mentioned, although the approach is quite general for any type of discontinuity in a waveguide, single and double round rod discontinuities have been chosen in the present work. Figure 4.10 shows four types of round rod discontinuity, generally used in waveguide post filters and Figure 4.9 shows their equivalent circuits.

The equivalent circuits are used to determine the K-inverter values and the values of the associated phase angle ϕ (see Figure 4.9), using the following equations,

$$K = \left| \tan\left(\frac{\phi}{2} + \tan^{-1} x_s \right) \right| , \tag{4.16}$$

$$\phi = -\tan^{-1}(2x_p + x_s) - \tan^{-1}(x_s) , \tag{4.17}$$

$$jx_s = \frac{1 - S_{12} + S_{11}}{1 - S_{11} + S_{12}} , \tag{4.18}$$

$$jx_p = \frac{2S_{12}}{(1 - S_{11})^2 - S_{12}^2} , \tag{4.19}$$

where $x_s = \frac{X_s}{Z_o}$ and $x_p = \frac{X_p}{Z_o}$; and S_{ij} are the computed scattering parameters of the K-inverter forming discontinuity shown in Figure 4.10e.

Using the previous equations, θ_j in Figure 4.9 can be calculated as

$$\theta_j = \pi + \frac{1}{2}(\phi_{j,j-1} + \phi_{j,j+1}) . \tag{4.20}$$

The physical distance between two adjacent K inverters is given by

$$l_j = \frac{\theta_j}{2\pi}\lambda_g . \tag{4.21}$$

4.3 Design of the iris waveguide low-pass filters

4.3.1. The design approach according to Levy and Rhodes' J-inverters

Corrugated waveguide structures are used as lowpass filters in numerous antenna feed systems. Their application is, most often, in rejection of spurious harmonics from transmitters. Historically, the first design is based on image parameters, thus it yields results of limited accuracy [21]. An advanced synthesis method for corrugated waveguide

filters is due to Levy [44]. In Levy's method, a generalized stepped-distributed lowpass prototype is used to generate normalized impedances of individual sections, and then converted into physical dimensions.

Figure 4.11 shows the general schematic diagram of a corrugated waveguide harmonic reject filter. It is basically a series of cascaded sections of cavities of electrical length $\pi/8$. Any two consecutive sections are coupled by a capacitive iris of width w and thickness t. Figure 4.12 shows the J-inverter equivalent network of the filter shown in Figure 4.11. The filter can be designed according to the design outlined in Levy's paper [44] and using the J-inverters by Rhodes [40]. More accurate J-inverters by Levy [45] could be used as well; however, calculation of such J-inverters requires numerical techniques. The design steps using J-inverters [40] are as follows:

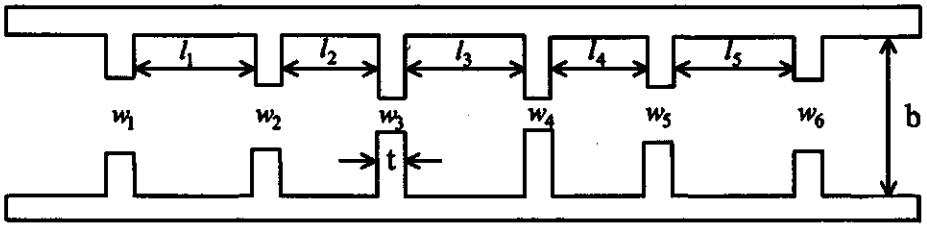

Figure 4.11 Corrugated waveguide harmonic reject filter

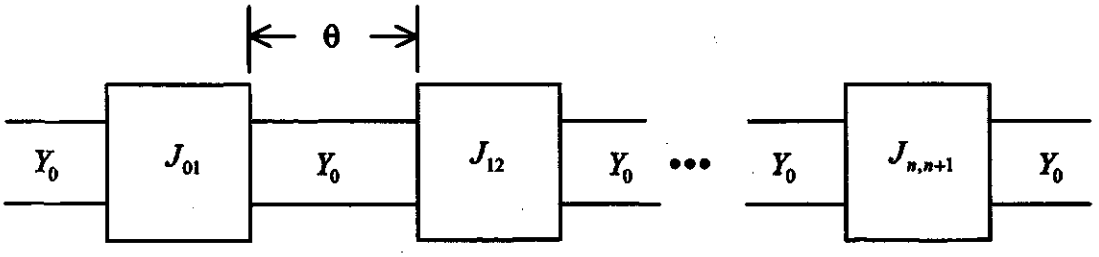

Figure 4.12 Equivalent network of the filter in Figure 4.11, containing impedance inverters

Consider the typical characteristics of a Chebyshev distributed lowpass prototype filter in Figure 4.13.

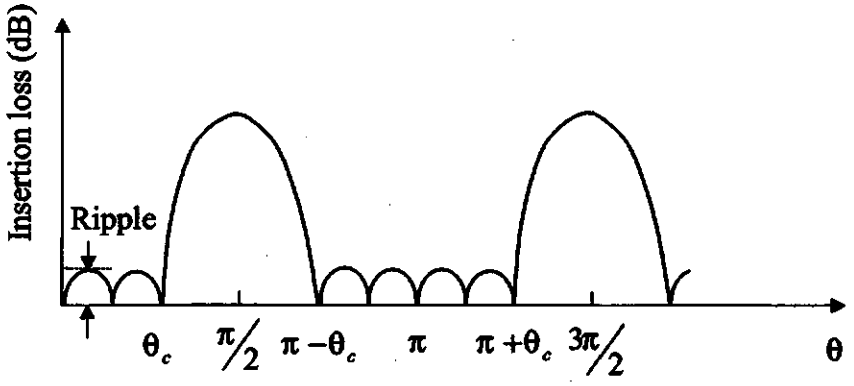

Figure 4.13 Typical characteristic of a Chebyshev distributed lowpass prototype filter

1) Define the fractional bandwidth of the filter as

$$w_q = \frac{2\theta_c}{\pi} . \tag{4.22a}$$

2) Calculate the normalized J-inverters as [40]

$$\overline{J}_{r,r+1} = \frac{J_{r,r+1}}{\sqrt{Y_r Y_{r+1}}} , \tag{4.22b}$$

where

$$Y_r = \frac{2\sin\left[(2r-1)\frac{\pi}{2N}\right]}{y\alpha} - \frac{\alpha}{4y}\left\{\frac{y^2+\sin^2\left(\frac{r\pi}{N}\right)}{\sin\left[(2r+1)\frac{\pi}{2N}\right]} + \frac{y^2+\sin^2\left[(r-1)\frac{\pi}{N}\right]}{\sin\left[(2r-3)\frac{\pi}{2N}\right]}\right\} + O_1(\alpha^3),$$

$$\text{for } r = 1 \text{ to } N, \tag{4.22c}$$

or $$Y_r = 1, \qquad \text{for } r = 0, N+1, \tag{4.22d}$$

where N is the order of the filter.

3) The scaling parameter α is given by

$$\alpha = \sin(\frac{\pi w_q}{4}), \tag{4.22e}$$

and the unnormalized J-inverters are given by

$$J_{r,r+1} = \frac{\sqrt{y^2 + \sin(\frac{r\pi}{N})^2}}{y}, \qquad \text{for } r = 0 \text{ to } N, \tag{4.22f}$$

where

$$y = \sinh\left[\frac{1}{N}\sinh^{-1}\frac{1}{\varepsilon_p}\right], \tag{4.22g}$$

and ε_p is the absolute value of the passband ripple.

The designer may choose a suitable type of capacitive waveguide discontinuity in order to realize the required J-inverters.

4.3.2. The full-wave 3-D modeling based approach with distributed element J-inverters of Rhodes [40]

Once the required J-inverter values have been obtained as described above [40], it is possible to characterize accurately the two-port scattering matrix of the capacitive discontinuity that forms a J-inverter. A viable option is the full electromagnetic modelling of a capacitive iris discontinuity in a rectangular waveguide. A number of papers have appeared in the literature that deal with such analysis [46]. However, there is now a variety of very accurate full electromagnetic analysis based commercially available software that can be used to generate the design model for the J-inverters for the filter configuration shown in Figure 4.11. The Transmission Line Matrix analysis based

software Micro-Stripes [6] was used to develop the model for the J-inverters for the iris discontinuities shown in Figure 4.14a. Figure 4.14b shows the equivalent circuit. The required J-inverter values will also be calculated for the filters using the distributed element prototype network by Rhodes [40].

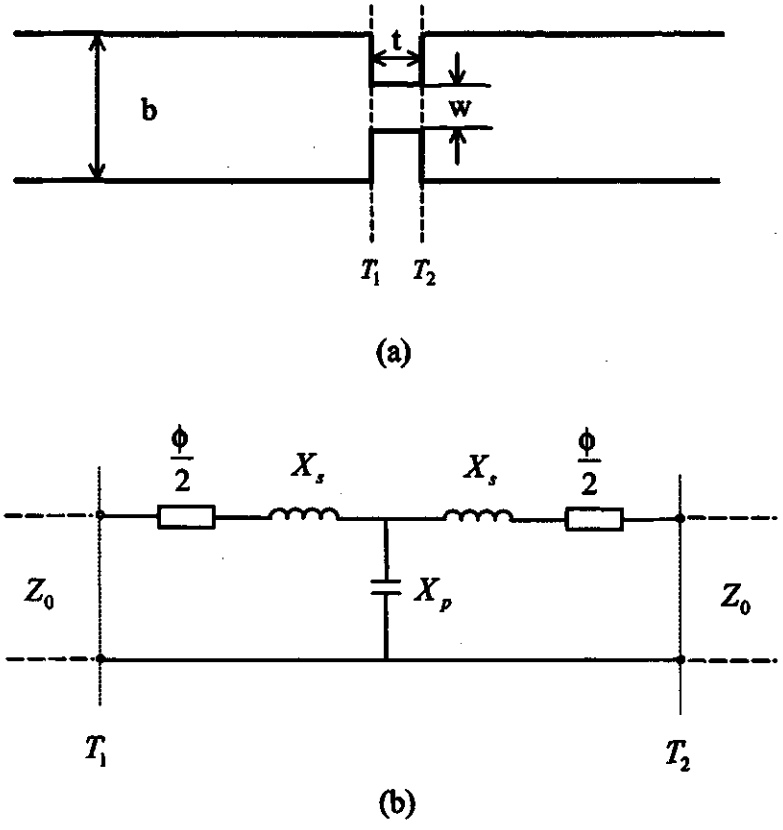

Figure 4.14 Equivalent circuit of a thick capacitive iris in a waveguide

The order of the filter, N, will give the number of sections and $N + 1$ will be the number of iris J-inverters needed to meet the design specifications. N is determined from the ripple bandwidth Δf, the isolation bandwidth Δf_i, the passband return loss L_r and

the stop band isolation L_s of the filter using the following equation for a Chebyshev type response. The filter order is given by [40].

$$N \geq \frac{L_s + L_r + 6}{20 \log(\gamma + \sqrt{\gamma^2 - 1})}, \tag{4.23}$$

where γ is the ratio $\Delta f_1 / \Delta f$.

Once the required J-inverter values have been calculated from the above equations (Equations 4.22a-g), they can be physically realized in terms of capacitive discontinuities in a rectangular waveguide. As mentioned above, although the approach is quite general for any type of capacitive discontinuity in a waveguide, the simplest capacitive iris discontinuity was chosen. Figure 4.14b shows the equivalent circuit of a thick capacitive iris in a waveguide. The equivalent circuit is used to determine the J-inverter value and the value of the associated phase angle ϕ, using the following equations.

$$\phi = -\tan^{-1}(2x_p + x_s) - \tan^{-1}(x_s), \tag{4.24a}$$

$$jx_s = \frac{1 - S_{12} + S_{11}}{1 - S_{11} + S_{12}}, \tag{4.24b}$$

$$jx_p = \frac{2S_{12}}{(1 - S_{11})^2 - S_{12}^2}. \tag{4.24c}$$

Using the above equations, θ_j in Figure 4.12 can be calculated as

$$\theta_j = \frac{\pi}{8} + \frac{1}{2}(\phi_{j,j-1} + \phi_{j,j+1}). \tag{4.24d}$$

The physical distance between two adjacent J inverters or the cavity length is given by

$$l_j = \frac{\theta_j}{2\pi} \lambda_g, \tag{4.24e}$$

where $x_s = \frac{X_s}{Z_o}$, $x_p = \frac{X_p}{Z_o}$, and S_{ij} are the computed scattering parameters of the J-inverter forming discontinuity shown in Figure 4.14a; λ_g is the guide wavelength.

4.4 Chapter summary

This chapter deals with the basic concepts of the filter design using distributed element transmission line. Two types of distributed element resonators are considered. Those support the TEM mode and the TE mode. Starting from the basic lumped element lowpass prototype circuit, the design equations for distributed element filters and the associated K- and J-inverters are discussed. This chapter also discusses how to obtain the resonator lengths for bandpass and lowpass filters.

Chapter 5 Results and Discussion

The 2D and 3D field simulator based microwave filter design approach, described in the previous chapter, has been used in designing a number of slab-line and waveguide bandpass filters. The slab-line filters use mono-block ceramic structure with air-hole couplers and the waveguide filters use single and double round rod couplers or K-inverters.

Besides the bandpass filters, the 3D field simulator based approach is also applied to the design of lowpass waveguide filters coupled by capacitive irises.

This chapter presents and discusses computed and measured results on the above filters, and validates the design approach used in this research.

5.1 Mono-block ceramic microwave bandpass filters

5.1.1 Structure simulations

Figure 4.5 shows the mono-block ceramic filter structure. The FEM method discussed in Chapter 3 is used to calculate the coupling coefficients K^e. The calculation is performed using the commercial FEM software PDEase [8]. PDEase is a powerful and flexible software package for obtaining numerical solutions of static and time-dependent systems of linear and nonlinear partial differential equations by the finite element method.

The plot of the even- and the odd-mode dielectric constants as functions of the radius of the air hole, for a fixed distance between the air hole and the metalized hole, is shown in Figure 5.1. The coupling coefficient K^c vs. the radius of the vacant hole r is shown in Figure 5.2. When no vacant hole exists ($r = 0$), the coupling coefficient K^c is equal to zero due to electric and magnetic phase cancellation [47]. With increasing air hole radius r, the coupling coefficient K^c increases because of the larger difference between the even mode and the odd mode effective dielectric constants ε_r^e and ε_r^o, respectively. At the point of $r = 1.05$ *mm*, the coupling reaches its maximum value and then decreases with further increase in r.

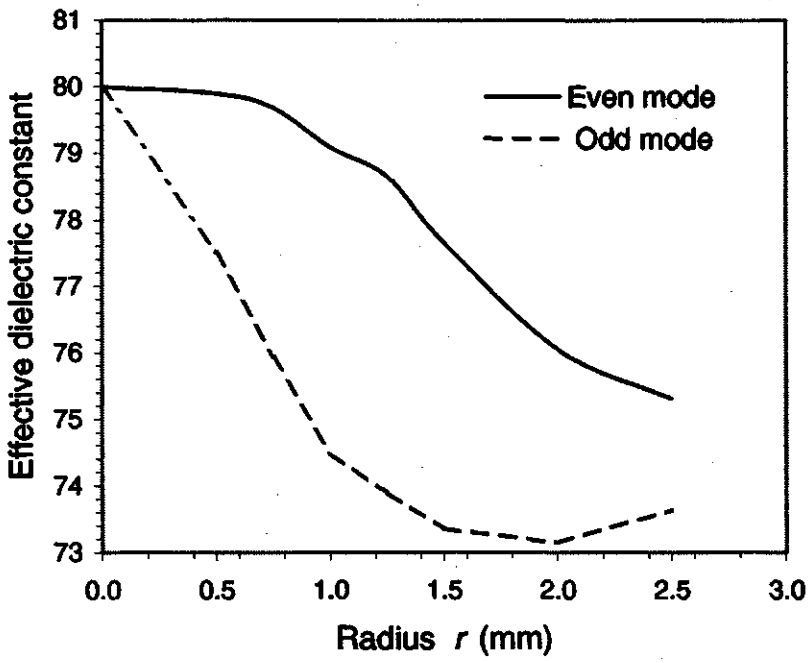

Figure 5.1 Effective dielectric constants versus the radius of the vacant hole

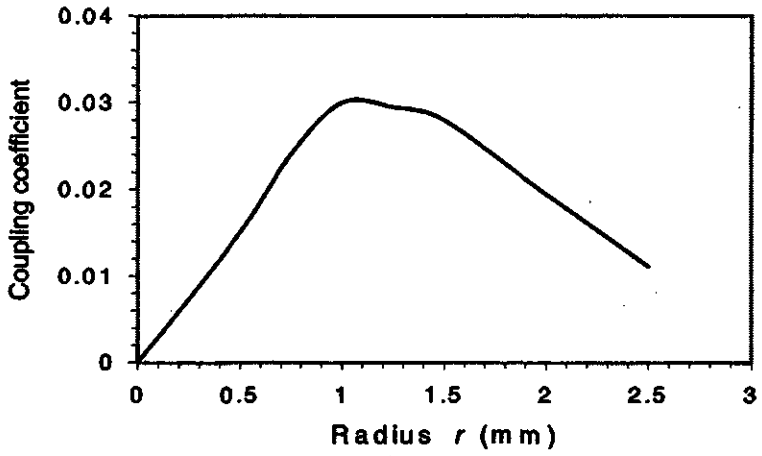

Figure 5.2 Coupling coefficient versus the radius of the vacant hole

Figure 5.3 shows the plot of the coupling coefficient K vs. the distance s between the air hole and the metalized hole for a fixed radius of the air hole. The coupling coefficient varies inversely with distance s, due to the fact that the larger the distance between two resonators, the weaker the coupling.

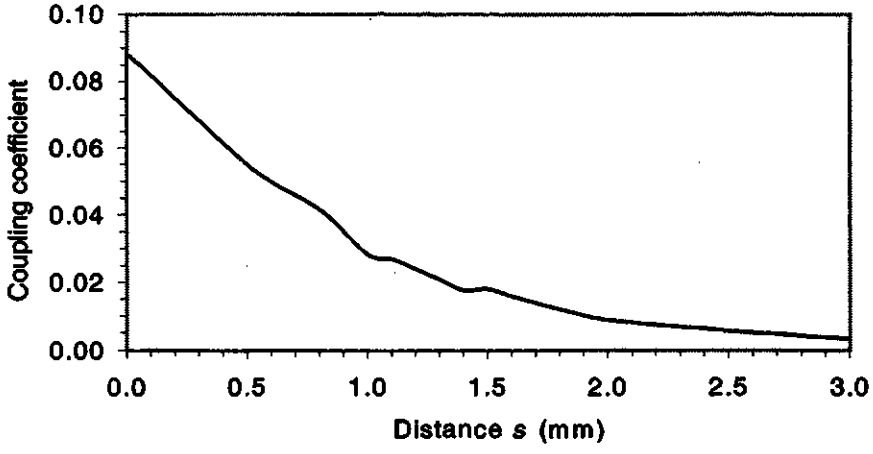

Figure 5.3 Plot of coupling coefficient K versus the distance s

Using the software TableCurve 2D [48], an equation between distance s and coupling coefficient K^c is obtained as

$$s = a + b(K^c) + c(K^c)^2 \ln(K^c) + d/(K^c)^{0.5} + f e^{-(K^c)}, \qquad (5.1)$$

where a = 1046.113, b = -1095.683, c = -362.365, d = 0.115, and f = -1044.915. Equation 5.1 is for D = 2.4mm, r = 1.2mm, L = 6mm, and $\varepsilon_r = 80$. The design equation is programmed in a personal computer and subsequently used as a direct aid to filter synthesis.

5.1.2 Result of the filter design

A mono-block ceramic bandpass filter was designed as follows:

Specifications of the filter:

- Center frequency $f_0 = 900\ MHz$
- Bandwidth $\Delta f = 33\ MHz$
- Return loss $RL = 13.5\ dB$
- Isolation $IL = 28\ dB$
- Isolation bandwidth $\Delta f_i = 57\ MHz$

Using Equation (4.1i) gives the filter order N = 5. The corresponding lowpass prototype element values and the coupling coefficients are listed in Table 5.1.

Table 5.1 Lowpass prototype element values and coupling coefficients of the filter

$N = 5$				
n	g_n		K_{ij}^c	
1	1.3395		K_{12}^c	0.0274
2	1.3370		K_{23}^c	0.0215
3	2.1661		K_{34}^c	0.0215
4	1.3370		K_{45}^c	0.0274
5	1.3395			

The values of the distances between the metal hole and the air hole are obtained using Equation 5.1. The dimensions of the filter are calculated from the design method described in Chapter 4 and given in Table 5.2.

Table 5.2 Dimensions of the filter as illustrated in Figure 4.5

$D = 2.4, d = 2.4$	
$W = 6.0, H = 9.49$	
s_{12} (mm)	3.5
s_{23} (mm)	3.7
s_{34} (mm)	3.7
s_{45} (mm)	3.5

The designed filter was manufactured by Motorola Ceramic Products, Albuquerque, USA. The measured plot of the filter's frequency response is shown in

Figure 5.4. From Figure 5.4, it is seen that the manufactured filter meets the design specifications. The bandwidth, the return loss and isolation are all met. However, the center frequency is shifted from 900 *MHz* to about 895 *MHz*. This may be caused by the error in manufacturing and in the value of the dielectric constant, or the neglect of non-adjacent resonator effects.

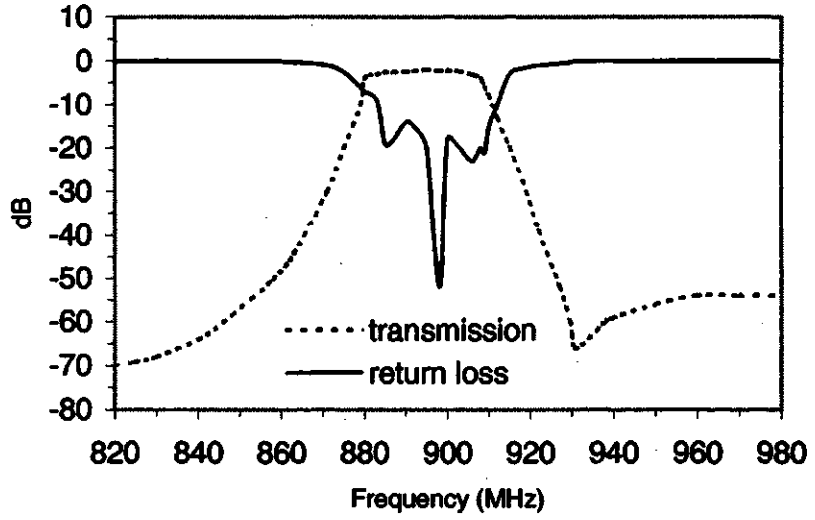

Figure 5.4 Measured result of the frequency response of the designed filter

5.1.3 Improvement of the design

To decrease the filter's dimensions further, the radii of the air holes are changed and the air holes are shifted up from the slab-line's axis, as shown in Figure 5.5. Table 5.3 shows the dimensions of the filter. This filter will be fabricated and subsequently tested.

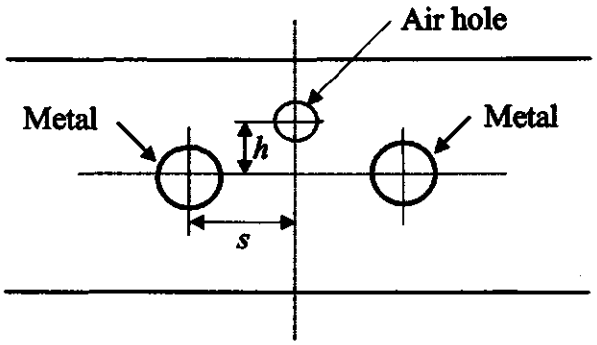

Figure 5.5 New structure of the filter

Table 5.3 New dimensions of the filter

D = 2.4, d = 1.0, s = 0.5 (mm)	
W = 6.0, H = 9.45	
h_1 *(mm)*	*0.5*
h_2 *(mm)*	*0.8*
h_3 *(mm)*	*0.8*
h_4 *(mm)*	*0.5*

The new filter has a more compact structure. For almost the same width and height, the length of the filter is 39mm, compared to 56.2mm for the former structure. These are significant improvements in length, volume, and weight of the filter.

5.2 Round rod waveguide bandpass filters

5.2.1 Simulation results of the round rod waveguide

Figure 5.6 shows the computed K-inverter and phase (ϕ) values as functions of the normalized distance from one of the side walls of the waveguide with normalized frequency as a parameter. The diameter of the rod is kept constant (see Figure 5.7). f_c is the cutoff frequency of the dominant mode (TE_{10}) and f is the center frequency of the filter to be designed. The curves have been obtained by the TLM analysis of the discontinuity using the Micro-Stripes [6] program. The analytical equations for the curves are shown in the Appendix A.1, which are obtained using the software TableCurve 2D [48]. The equations are programmed in a personal computer and subsequently used as a direct aid to filter synthesis.

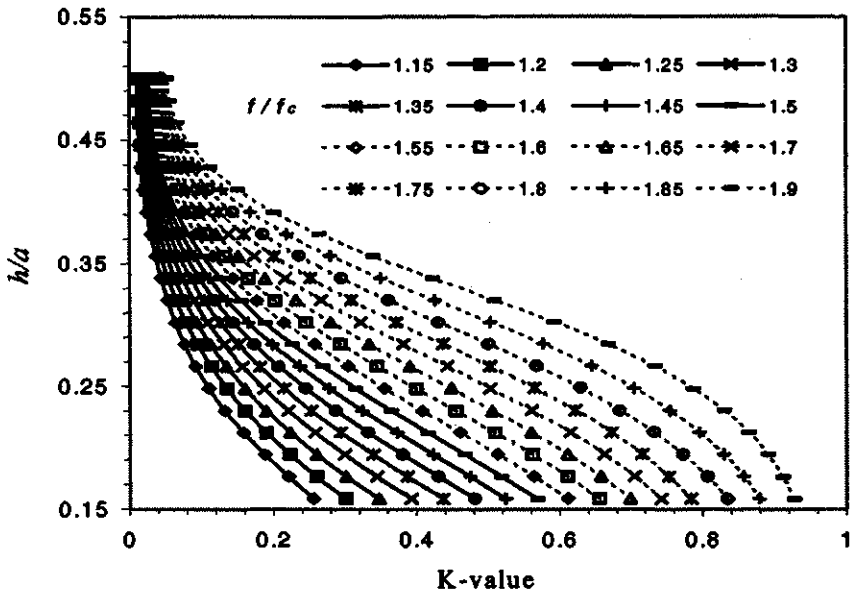

Figure 5.6a Computed K-inverter values for a constant diameter single rod discontinuity in a rectangular waveguide ($a/b = 2.25$)

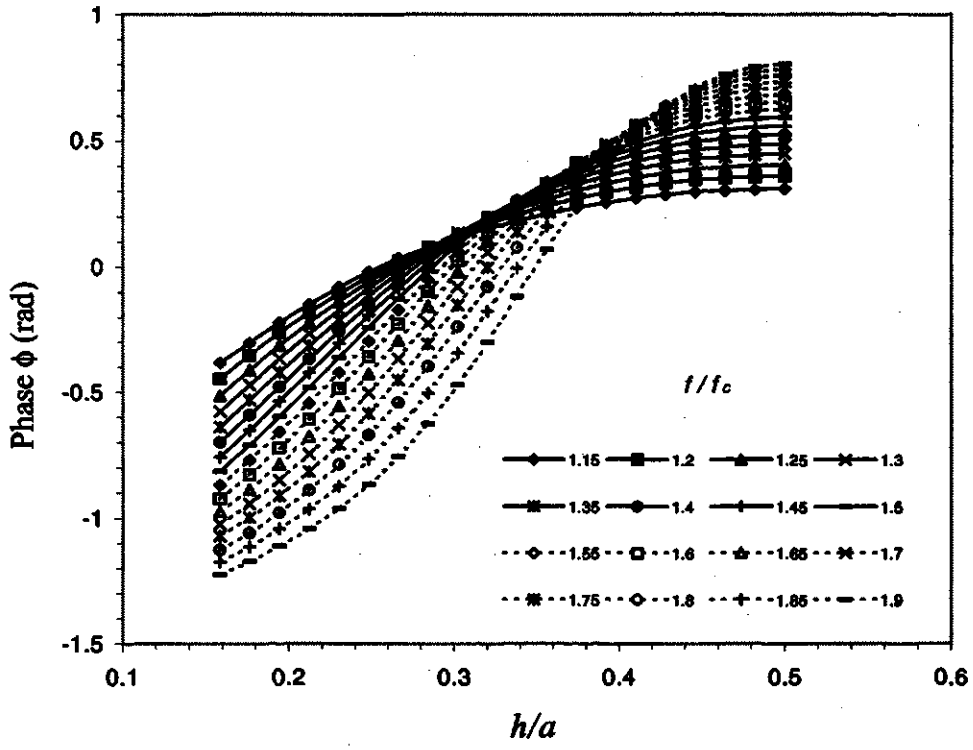

Figure 5.6b Computed phase ϕ values for a constant diameter single rod discontinuity in a rectangular waveguide ($a/b = 2.25$)

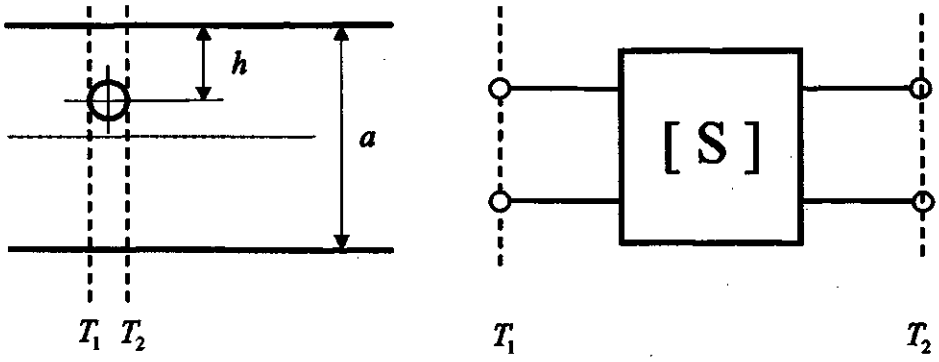

Figure 5.7 Simulation structure for a constant diameter single rod discontinuity in a rectangular waveguide

Figure 5.8 shows the computed K-inverter and phase ϕ curves for the constant diameter double rod (see Figure 5.9) discontinuity. Here both K and ϕ are functions of the distance d between the rods. The equations for the curves have been shown in the Appendix A.2. Once again, the curves and the equations can be directly used as design tools.

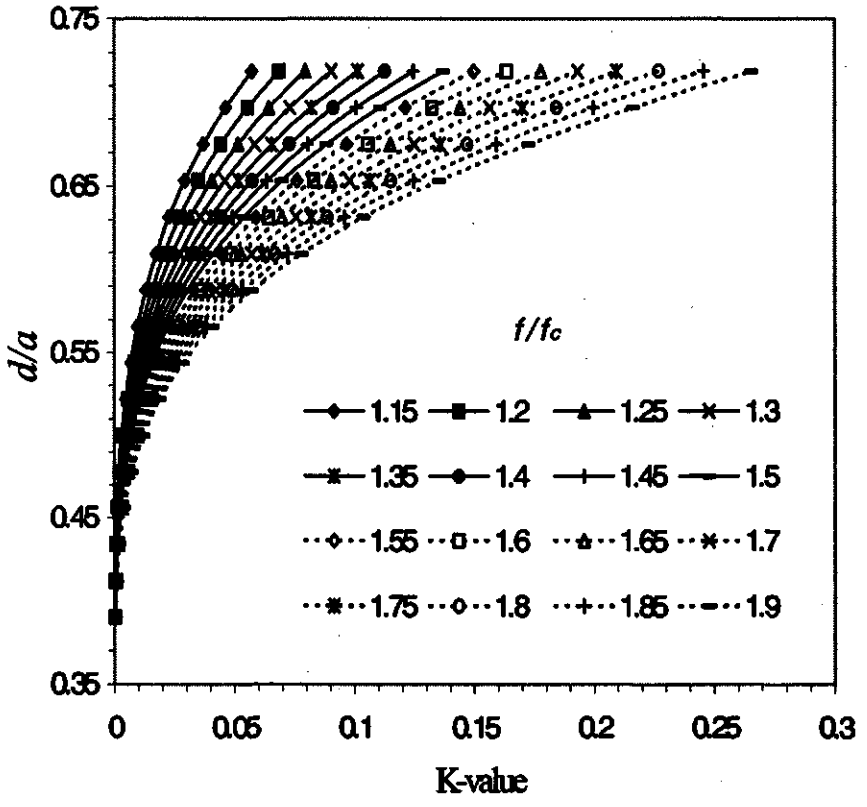

Figure 5.8a Computed K-inverter values for a constant diameter double rod discontinuity in a rectangular waveguide ($a/b = 2.25$)

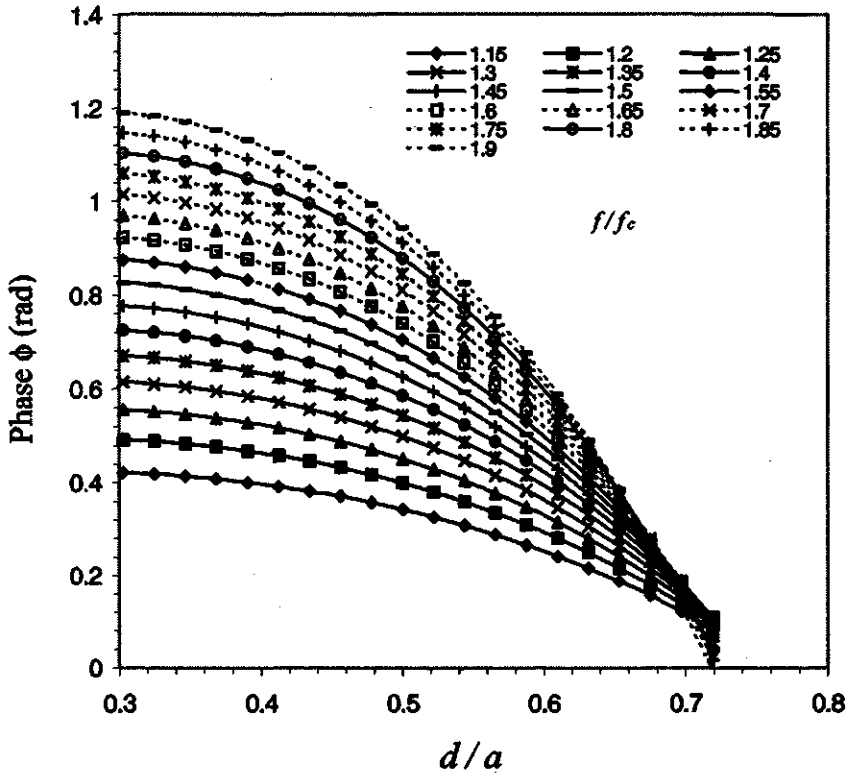

Figure 5.8b Computed phase ϕ values for a constant diameter double rod discontinuity in a rectangular waveguide ($a/b = 2.25$)

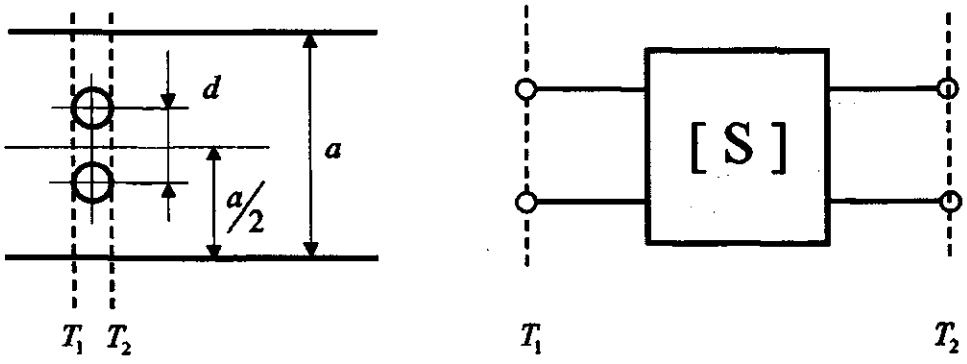

Figure 5.9 Simulation structure for the constant diameter double rod discontinuity in a rectangular waveguide

Figure 5.10 shows the design curves for a single post filter with variable diameter and located at the center of the broad wall of the waveguide resonator as shown in Figure 5.11. The corresponding design equations are shown in the Appendix A.3. The computed curves are more accurate than those in Mathaei, Young and Jones' handbook [4] and Marcuvitz's waveguide handbook [9]. In their handbooks, the results have limited accuracy and are valid for a limited range of frequency.

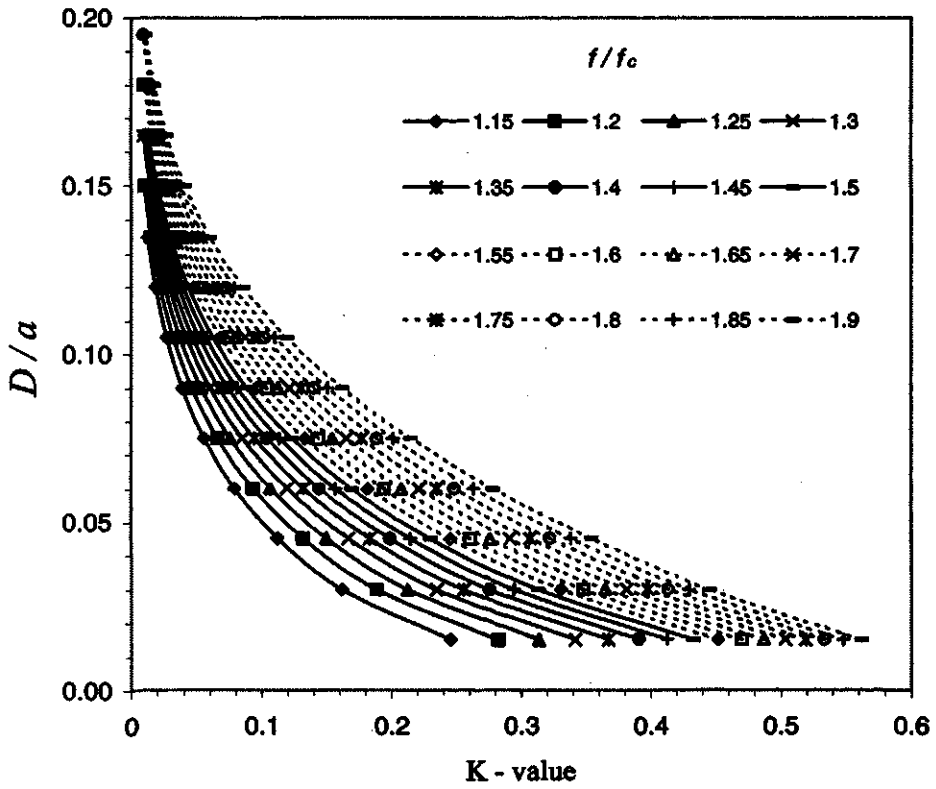

Figure 5.10a Computed K-inverter values for a variable diameter single rod discontinuity in a rectangular waveguide ($a/b = 2.25$)

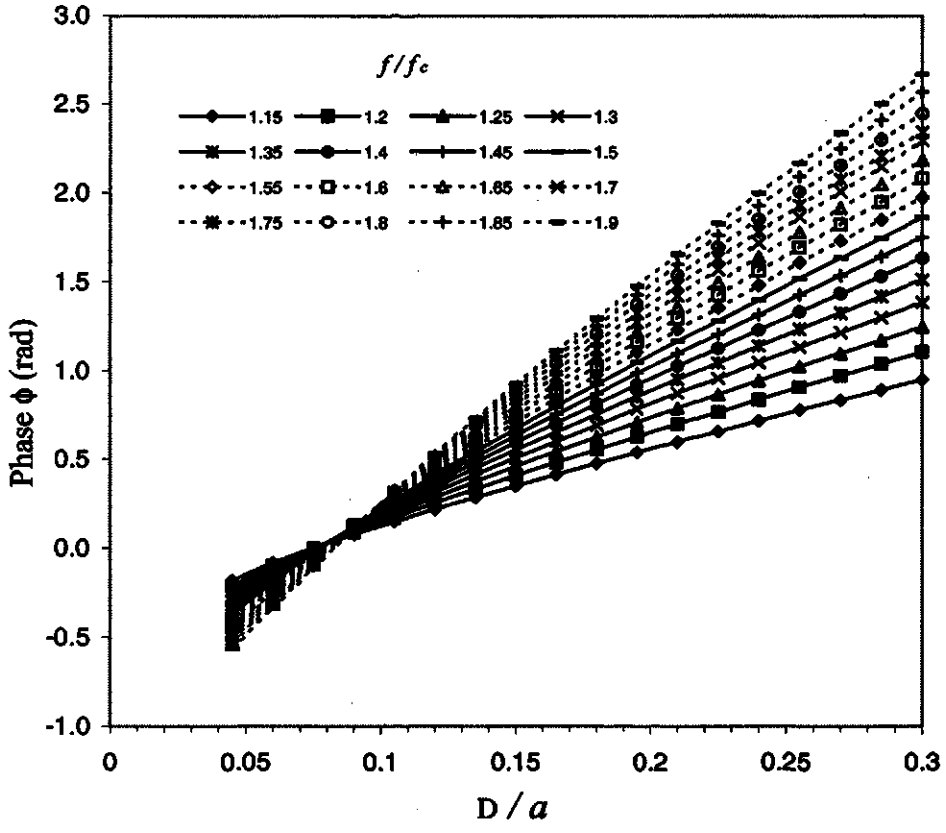

Figure 5.10b Computed phase ϕ values for a variable diameter single rod discontinuity in a rectangular waveguide ($a/b = 2.25$)

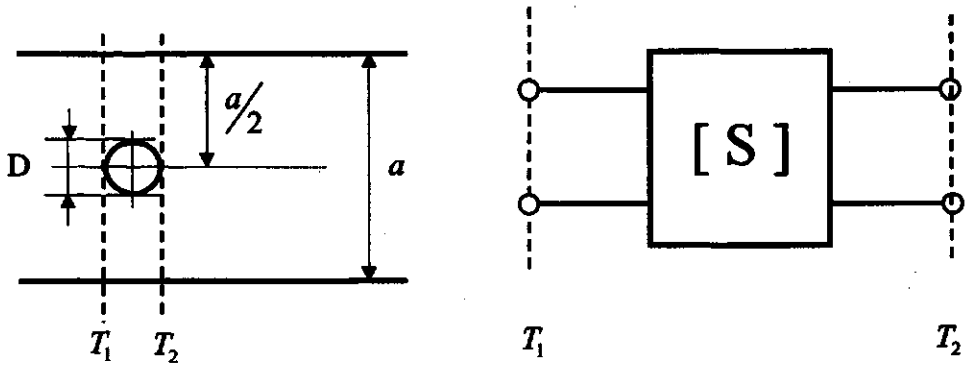

Figure 5.11 Simulation structure for a variable diameter single rod discontinuity in a rectangular waveguide

Similar database for variable-diameter double post discontinuities or other structures can also be developed, if needed.

5.2.2 Results of the bandpass filter design and discussions

Three filters have been designed using the modeling results developed and presented in the preceding section. In each case, the designed filter was analyzed using the Finite Element Method (Fullwave [7]) or the Mode Matching Method. These methods are different than TLM, which is used to model the K-inverters. The computed frequency responses of the filters met the design specifications very well and it establishes confidence in the method and the design curves.

Figure 5.12 shows the frequency response of a variable diameter single rod filter with the specifications as:

- Center frequency $f_0 = 9.5\ GHz$
- Bandwidth $\Delta f = 300\ MHz$
- Return loss $RL = 16\ dB$
- Isolation $IL = 70\ dB$
- Isolation bandwidth $\Delta f_i = 1\ GHz$

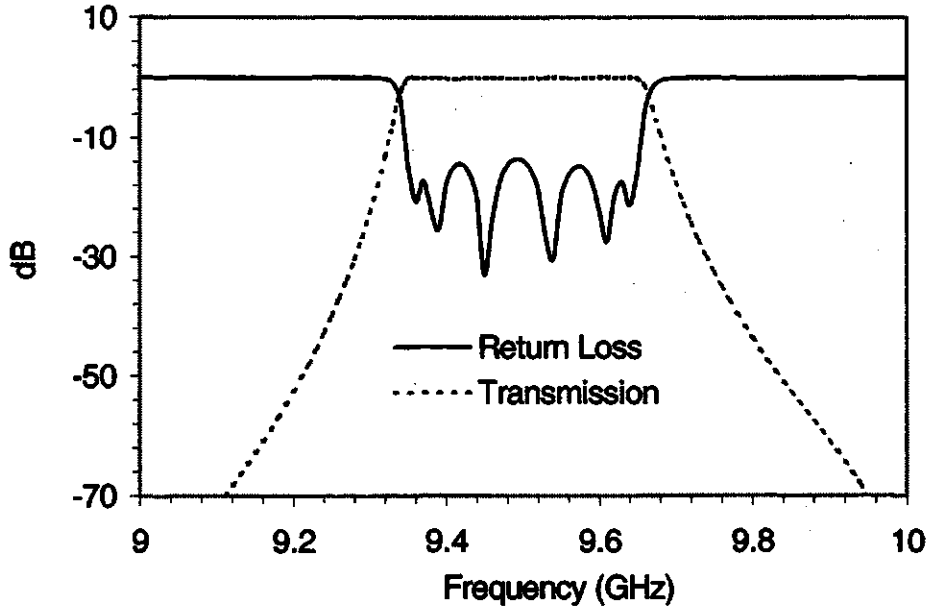

Figure 5.12 Analyzed frequency response of a single rod filter with variable diameter; a = 22.86mm, b = 10.16mm, r_1 = 0.785mm, r_2 = 2.169mm, r_3 = 2.413mm, r_4 = 2.444mm, l_1 = 20.761mm, l_2 = 23.353mm, l_3 = 23.731mm

This filter was designed as a constituent channel of an X-band diplexer. Figure 5.13 shows the response of the second channel designed by the same method. The second channel is centered at a frequency that is 650 *MHz* away from the first channel but has an identical frequency response. The computed results show very good agreement between synthesis and analysis, with the exception of a difference of less than 2.00 *dB* in the passband return loss in one of the channel filters.

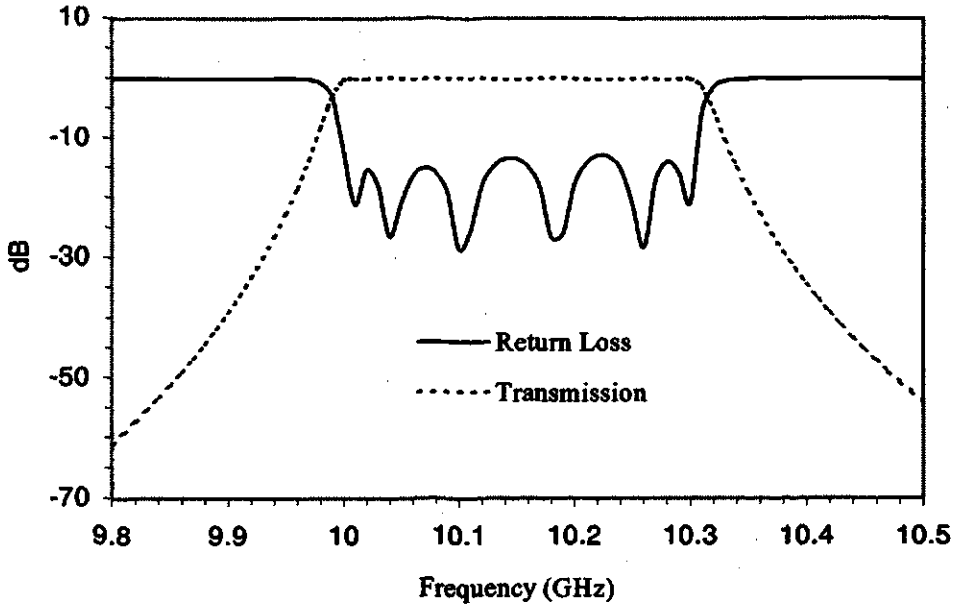

Figure 5.13 Analyzed frequency response of a single rod filter with variable diameter; a = 22.86mm, b = 10.16mm, r_1 = 1.018mm, r_2 = 2.490mm, r_3 = 2.730mm, r_4 = 2.761mm, l_1 = 19.124mm, l_2 = 21.663mm, l_3 = 22.015mm

Figure 5.14 shows the responses of the designed channel filters using variable diameter double rods of a narrower band diplexer in which the filter passbands are centered at 9.55 and 10.065 *GHz* with 100 *MHz* bandwidth and 1 *GHz* isolation bandwidth. These filters were analyzed using the Mode Matching Method. Once again, the agreement between design and analysis were found to be very good.

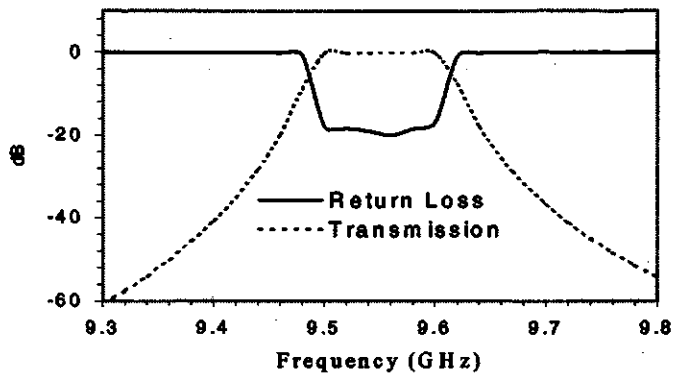

Figure 5.14a Analyzed frequency response of a double rod filter with variable diameter: a = 22.86mm, b = 10.16mm, r_1 = 0.536mm, r_2 = 1.531mm, r_3 = 1.634mm, l_1 = 21.210mm, l_2 = 23.036mm

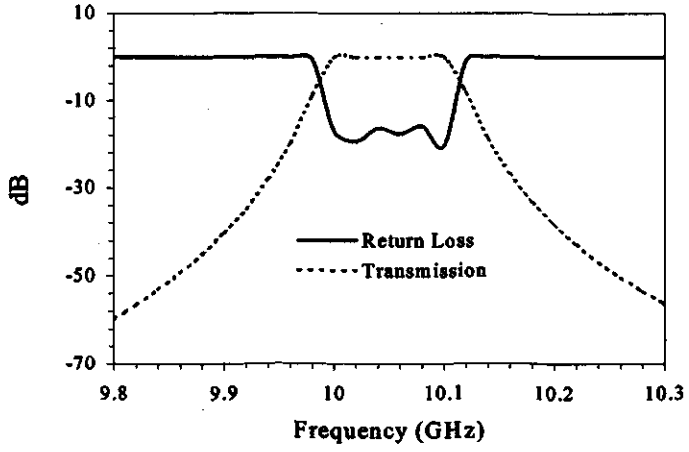

Figure 5.14b Analyzed frequency response of a double rod filter with variable diameter: a = 22.86mm, b = 10.16mm, r_1 = 0.634mm, r_2 = 1.638mm, r_3 = 1.736mm, l_1 = 19.655mm, l_2 = 21.401mm

Figure 5.15 shows the analyzed frequency response of an X-band filter that used a constant diameter single rod discontinuity. The filter is centered at 9.5 *GHz* with a 300 *MHz* bandwidth, 1 *GHz* isolation bandwidth, 70 *dB* isolation and 20 *dB* return loss. The analysis is performed using the TLM method and the Micro-Stripes [6] program. The analysis of frequency response shows achievement of accurate center frequency, bandwidth and isolation. However, the return loss is -12.2 *dB* instead of -20 *dB*.

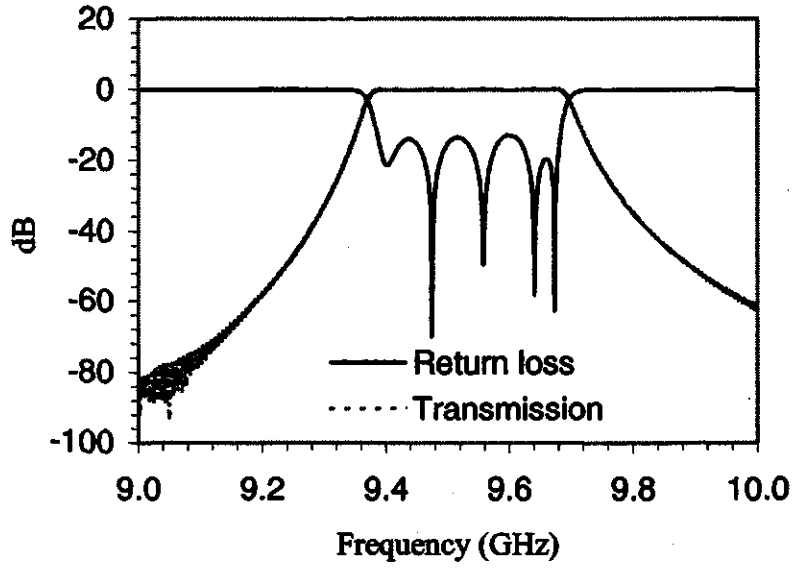

Figure 5.15 Analyzed frequency response of a constant diameter single rod filter (Analysis by Micro-Stripes [6]), a = 22.86mm, b = 10.16mm, r = 3.21mm, b_1 = 5.384mm, b_2 = 8.355mm, b_3 = 8.963mm, b_4 = 9.053mm, l_1 = 22.170mm, l_2 = 24.609mm, l_3 = 24.893mm

The filter was subsequently analyzed using the Mode Matching Method. Figure 5.16 shows the result of mode matching analysis. The return loss is about –18 *dB*. This error can be reduced to zero by redesigning the filter for 22 *dB* return loss.

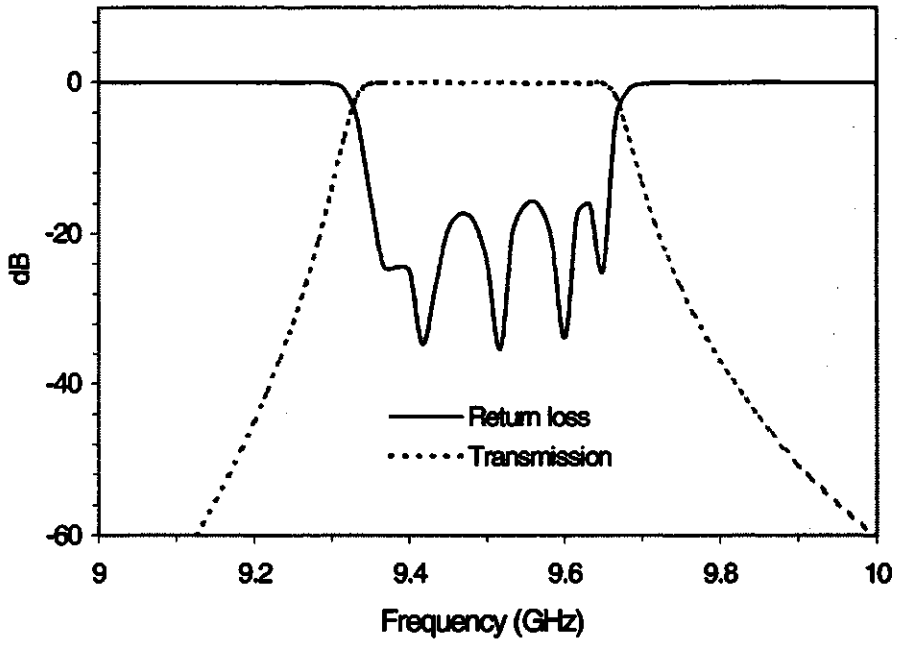

Figure 5.16 Analyzed frequency response of a constant diameter single rod filter (Analysis by the Mode Matching Method),

The above examples establish the confidence in the new approach towards waveguide filter design using modern 3-D simulators.

5.3 Iris waveguide lowpass filters

5.3.1 Simulation results of capacitive iris J-inverter in a rectangular waveguide

Figure 5.17 shows the computed normalized iris width w/a and phase ϕ values as functions of J-inverter value with normalized frequency f/f_c as a parameter, for a constant thickness iris t/a (see Figure 5.18) filter design, and for $b/a = 0.5$. f_c is the cutoff frequency of the dominant mode TE_{10} and f is the cutoff frequency of the filter to be designed. The curves are obtained by the TLM method using Micro-Stripes [6] program. The analytical equations for the curves are obtained by using TableCurve [48]. The equations are shown in Appendix B.1. The equations are programmed in a personal computer and can be used subsequently as a direct aid to filter synthesis.

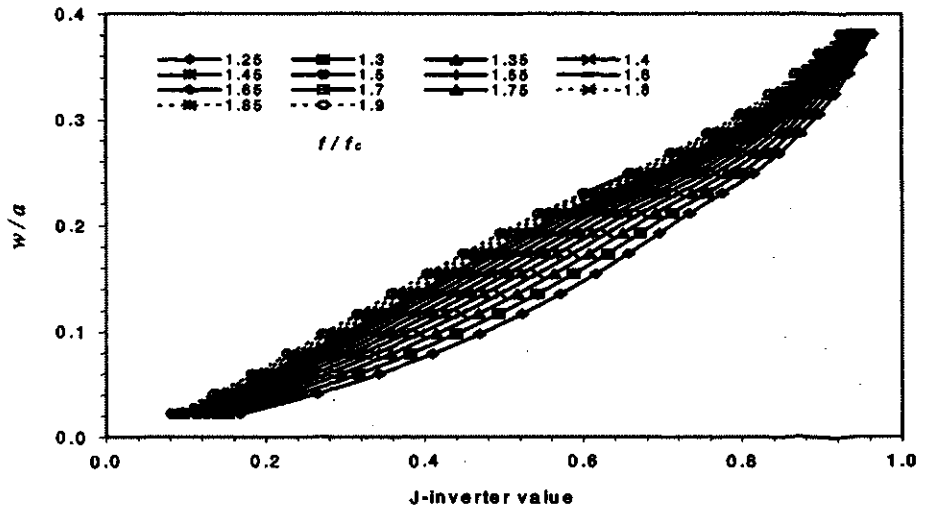

Figure 5.17a Computed J-inverter values for a constant iris thickness discontinuity in a rectangular waveguide ($b/a = 0.5$)

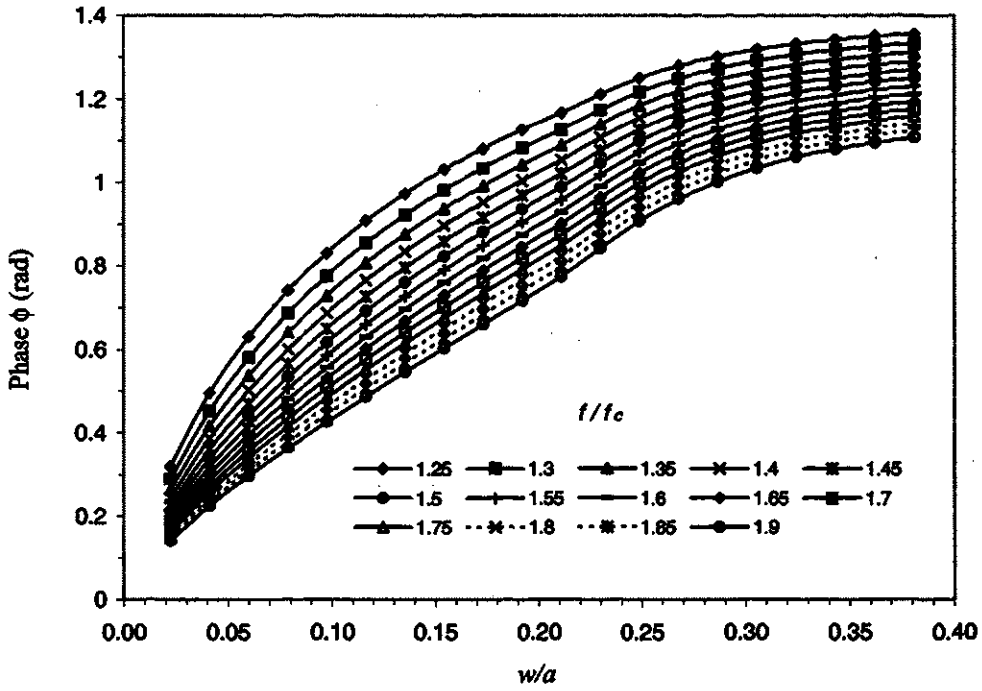

Figure 5.17b Computed phase ϕ values for a constant iris thickness discontinuity in a rectangular waveguide ($b/a = 0.5$)

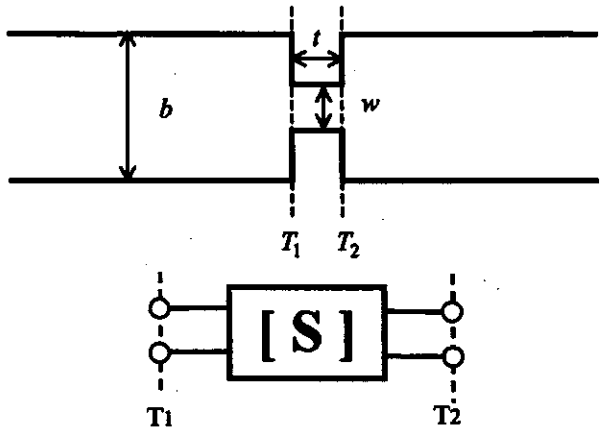

Figure 5.18 Simulation structure for a thick capacitive iris in a waveguide

Figure 5.19 shows the computed J-inverter and phase ϕ curves for the constant thickness capacitive iris, for $b/a = 0.444$. Here J and ϕ are functions of w/a and f/f_c, respectively. The equations for the curves are shown in the Appendix B.2. Once again, the curves and equations can be used directly as design tools.

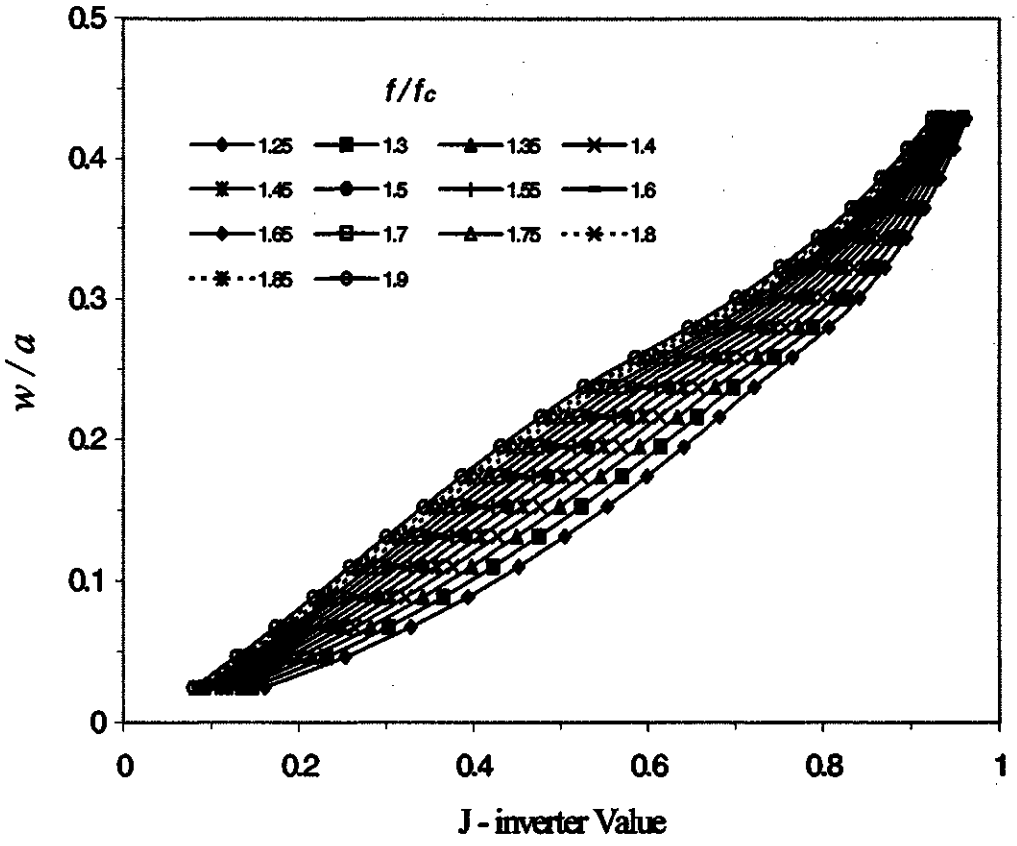

Figure 5.19a Computed J-inverter values for a constant iris thickness discontinuity in a rectangular waveguide ($b/a = 0.444$)

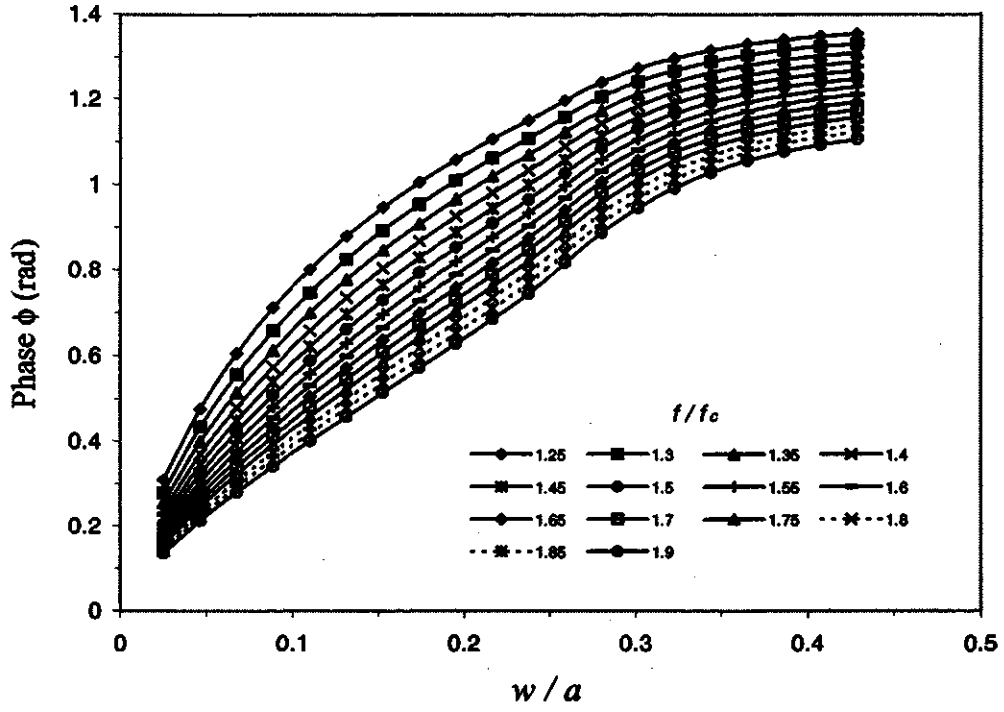

Figure 5.19b Computed phase ϕ values for a constant iris thickness discontinuity in a rectangular waveguide ($b/a = 0.444$)

The design curves in Figure 5.17 and 5.19 could be obtained using the closed-form analytical equations in Marcuvitz's Waveguide Handbook [9]. However, such equations offer limited accuracy and are valid for a limited range of frequency and geometrical dimensions.

A smaller b/a ratio suppresses TE_{1n} type modes and offers a wider stop band at the cost of lower power handling capability of the filter. Using the same method, design curves for other b/a ratios can be created.

5.3.2 Results of the lowpass filter design and discussions

In order to validate the design approach described in the preceding section, three filters were designed. Two of them were fabricated and experimentally tested. Figure 5.20 shows the analyzed frequency response of an eleven section X-band filter with cutoff at 8.00 *GHz* and designed for 20 *dB* passband return loss. The analysis was done using the Mode Matching Method. The computed cutoff frequency was found to be 8.045 *GHz*. The filter shows a very wide stopband with the first spurious passband occurring near 17.8 *GHz*.

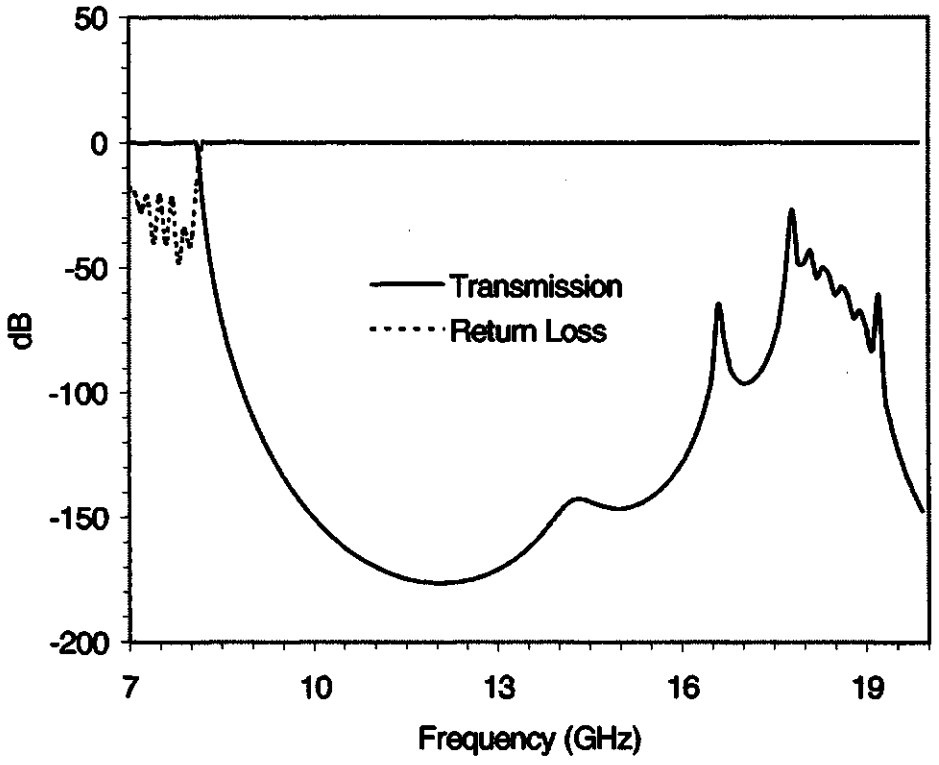

Figure 5.20 Analyzed frequency response of iris filter with constant iris thickness for $a = 22.86$mm, $b = 10.16$mm, $t = 2$mm

Figure 5.21 shows the analyzed frequency response of another X-band filter with cutoff at 9.5 *GHz*. This is a nine-section filter designed for 33 *dB* return loss in the passband. The analyzed response shows a poor return loss of 25 *dB*. Table 5.4 shows the computed geometrical dimension of the filter. Figure 5.22 shows the computed frequency response of the same filter designed using Levy's Scheme [45]. More than 33 *dB* return loss is obtained in the passband.

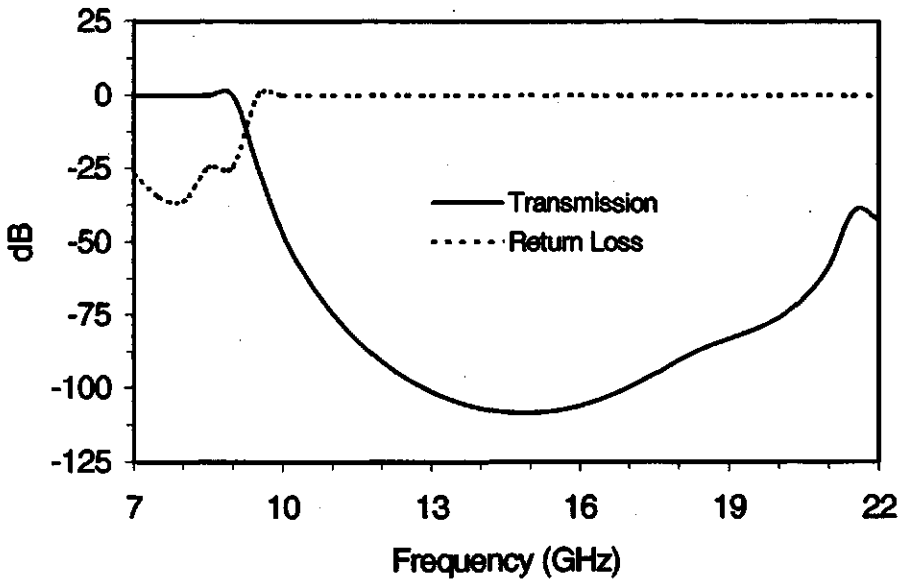

Figure 5.21 Analyzed frequency response of iris filter with constant iris thickness for a = 28.5mm, b = 7.112mm, t = 2.54mm, designed by Rhodes' method [40]

Table 5.4 The computed geometrical dimension of the filter for $a = 28.5$mm, $b = 7.112$mm, and $t = 2.54$mm

Iris widths (mm)	*Resonator lengths (mm)*
w(0) = 4.36	*l(1) = 8.28*
w(1) = 2.52	*l(2) = 6.76*
w(2) = 1.59	*l(3) = 5.92*
w(3) = 1.29	*l(4) = 5.62*
w(4) = 1.22	*l(5) = 5.56*
w(5) = 1.22	*l(6) = 5.62*
w(6) = 1.29	*l(7) = 5.92*
w(7) = 1.59	*l(8) = 6.76*
w(8) = 2.52	*l(9) = 8.28*
w(9) = 4.36	

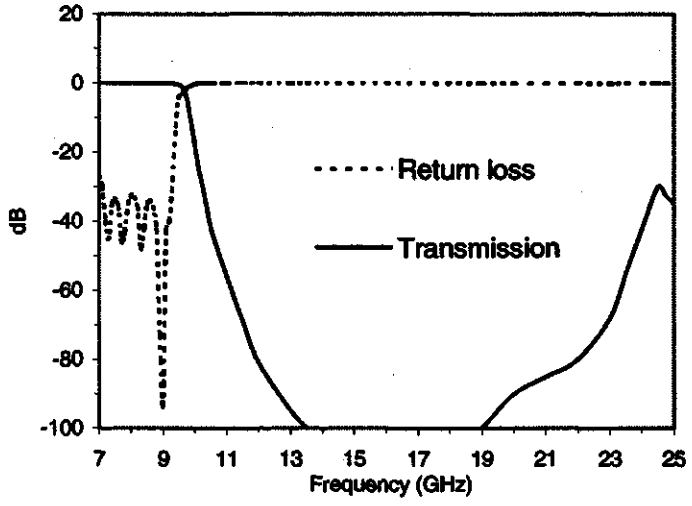

Figure 5.22 Computed frequency response designed using Levy's Scheme [45]

Figure 5.23 shows the experimental frequency response of the filter. The measured passband return loss is only 26 *dB* because of the two stepped impedance transformers used at the two ends of the filter during measurement. The measuring

equipment has limits at below -60 *dB* to -70 *dB* at very high frequencies according to the testing engineer. The fluctuations in the stopband may be due to the misalignment of the irises in the manufactured filter. The misalignments change the propagation of the microwaves in the filter and can be eliminated by accurate manufacturing. The fluctuations may also be caused by the interaction of higher order modes.

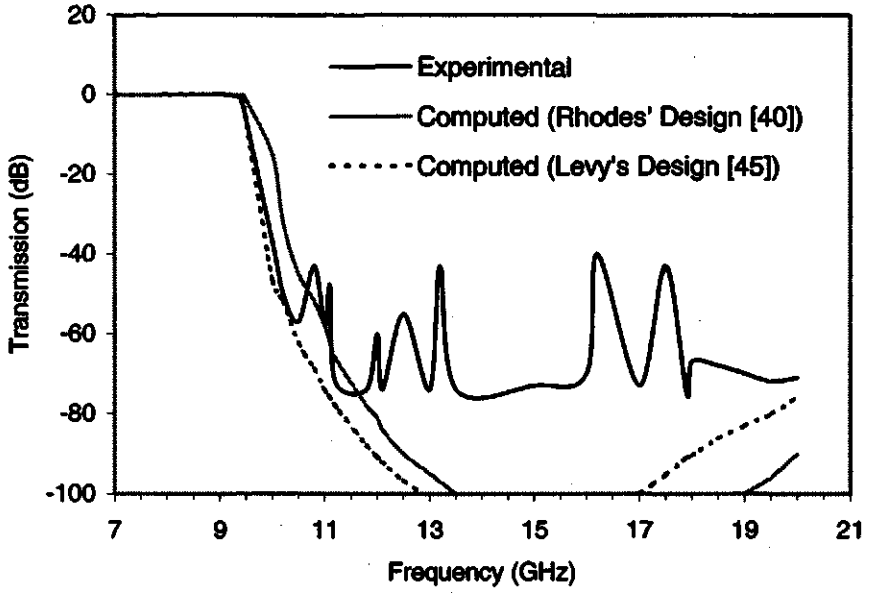

Figure 5.23 Experimental frequency response of the filter

Figure 5.24 shows the computed frequency response of a seven section filter designed by Rhodes' method, for 26 *dB* passband return loss and 20 *GHz* cut-off frequency. Figure 5.25 shows the frequency response of the same filter designed by Levy's Scheme [45]. While Rhodes method shows only 20 *dB* return loss, Levy's Scheme [45] shows 26 *dB* return loss. In either case, however, the computed cut-off is at 19.5 *GHz*. Figure 5.26 shows the measured frequency response of the filter. The measured cut-off frequency is at 19.35 *GHz*. The experimental result looks good enough.

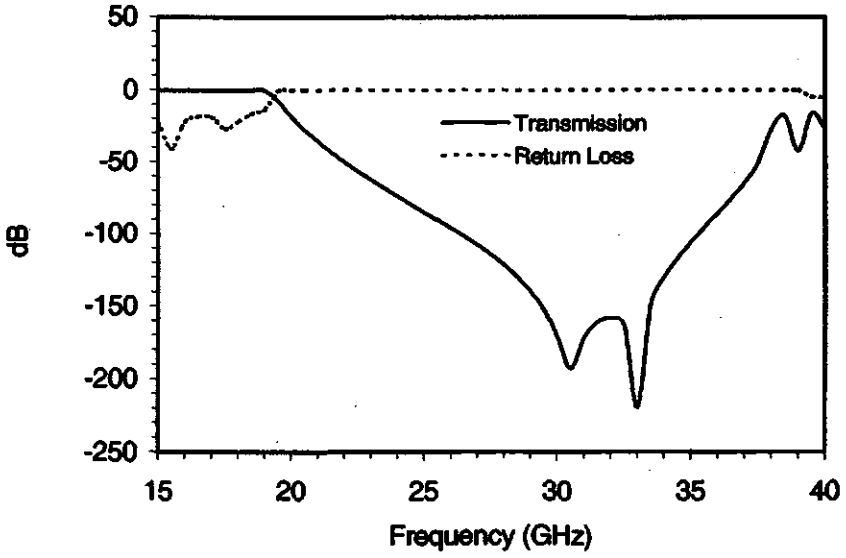

Figure 5.24 Computed frequency response of iris filter with constant iris thickness, a = 15.8mm, b = 7.9mm, t = 0.51mm, designed by Rhodes' method

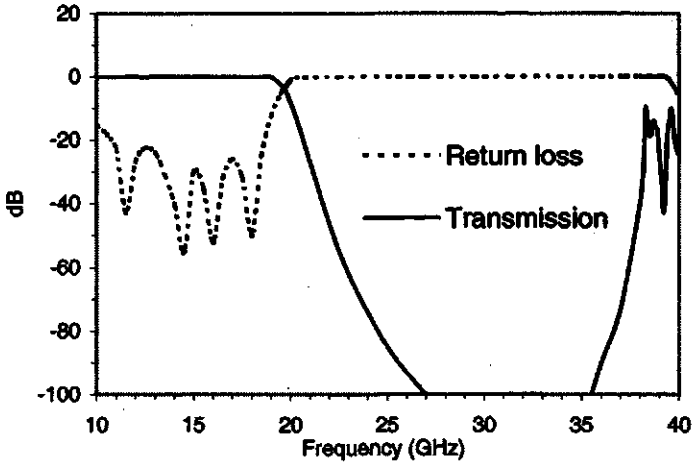

Figure 5.25 Computed frequency response of the filter designed by Levy's Scheme [45]

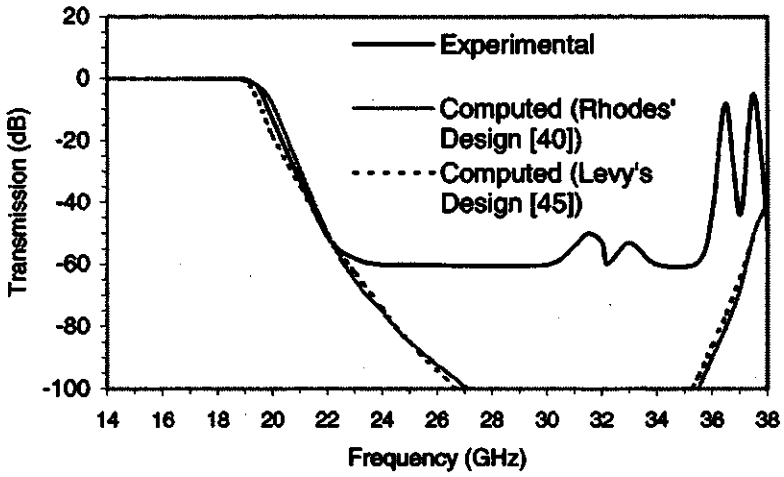

Figure 5.26 Measured frequency response of the filter

The agreement between computed and experimental results shows that the higher order mode interaction among adjacent irises have little effect on the frequency response of a filter. It also establishes the confidence in the iris coupled waveguide lowpass filter design using modern 3-D simulators.

5.4 Chapter summary

This chapter has demonstrated a successful use of commercially available 2D or 3D simulators in the design of TEM or TE mode waveguide filters. The software based on the numerical methods introduced in Chapter 3 are used to calculate coupling coefficients of resonators in slab-line filter and K- and J- inverters of discontinuities in waveguide filters. Matching equations for these data are formed as direct aids for filter syntheses. Several examples have been presented for theoretical and experimental validity of the approach. The analyzed and measured frequency responses for these filters are also compared and discussed.

Chapter 6 Conclusions

6.1 Summary and conclusions

The objective of the research in this thesis is to establish the fact that the existing commercially available simulation tools, based on full and rigorous electromagnetic field analysis, can be successfully used in designing microwave waveguide and slab-line filters.

In this thesis, Chapter 1 introduces the fundamental concepts on microwaves. Several waveguide configurations including coaxial cable, rectangular waveguide, and slab-line are also introduced. It also discusses the definitions associated with and classifications of microwave filters. These concepts are very important for the design of the filters discussed in the following chapters. Several commercial simulation tools are also introduced. Finally in Chapter 1, the research objectives and thesis overview are stated.

Literature survey on microwave filter design is presented in Chapter 2. Some important concepts on K- and J- inverters, waveguide discontinuities and scattering matrix are described. The chapter also discusses the roles of different types of waveguide and slab-line discontinuities in microwave filter realization.

In Chapter 3, three numerical methods for solving electromagnetic problems are discussed. The methods include the Finite Difference Method (FDM), the Finite Element

Method (FEM) and the Transmission Line Matrix Method (TLM). These are the three methods used in the filter design of this research.

Chapter 4 deals with the basic concepts of the filter design using distributed element transmission line. Two types of distributed element resonators are considered. These support the TEM mode and the TE mode. Starting from the basic lumped element lowpass prototype circuit, the design equations for distributed element filters and the associated K- and J-inverters are discussed. This chapter also discusses how to obtain the resonator lengths for bandpass and lowpass filters.

Chapter 5 demonstrates a successful use of commercially available 2D or 3D simulators in the design of TEM or TE mode waveguide filters. The software based on the numerical methods introduced in Chapter 3 are used to calculate coupling coefficients of resonators in slab-line filter and K- and J- inverters of discontinuities in waveguide filters. Matching equations for these data are formed as direct aids for filter syntheses. Several examples have been presented for theoretical and experimental validity of the approach. The analyzed or measured frequency responses for these filters are also compared and discussed.

In the design of a TEM-mode ceramic block slab-line filter, the couplings between two consecutive resonators were realized by air holes instead of metal patches in the previous design. The design database was generated using the Finite Element Method. The database was subsequently used in the design of a mobile radio filter. The filter was fabricated by MOTOROLA. The measured performance of the filter was very good. It met all specifications except the centre frequency that was shifted by 5 MHz at 900 MHz. The shift in centre frequency could be due to following reasons: 1) Inaccurate dielectric

constant of the material; 2) Mechanical tolerance; 3) Neglect of non-adjacent resonator effects which was ignored in the design. On the whole, the simulation based approach proved to be highly efficient. Prior to the availability of this approach, MOTOROLA would require at least eight to ten iterations to realize such filters.

A new structure of the ceramic block filter is designed to decrease the volume of the filter. The radii of the air holes are decreased from 2.4 *mm* to 1 *mm* and their positions are shifted up from the slab-line's axis as shown in Figure 5.5. The volume and weight of the filter can be decreased by about 30 percent. Its compact size is more suitable for wireless communications. To the author's knowledge, this is the first time such a filter structure has been proposed. This filter will be fabricated and tested.

In the design of round-rod waveguide bandpass filters, the database for the K-inverters was generated by using the Transmission Line Matrix Method in the time domain. Several bandpass filters were designed using single and double rods. Each design was analyzed using the Finite Element Method or the Mode Matching Method in the frequency domain. The results showed that the filters met the design specifications.

A major pitfall in inductive reactance coupled waveguide bandpass filters is the higher order mode interactions among K-inverters. Such interactions tend to shift the centre frequency and reduce the bandwidth of a filter. However, such effects have not been noticed in the designs. This is due to the fact that very few higher order modes are generated by the non-abrupt round rod discontinuities. Therefore, the current approach will not be so effective if the resonators are iris or septum coupled.

In the design of corrugated waveguide lowpass filters, once again, the required database was generated using the TLM method. The approach is the same as used in

bandpass filter design. However, a different set of J-inverter equations was used. Several filters were designed and subsequently analyzed using the Finite Element Method. Levy's Scheme was used to prove the correctness of the design. Two filters were manufactured and tested. The experimental results showed excellent agreement with the design specifications.

There were certainly higher order mode interactions among the J-inverter forming capacitive iris discontinuities. However, with lowpass filters being inherently wide band, the effect was negligible.

The thesis has shown how to use analysis software to design various types of slab-line and waveguide filters. The generated database and the normalized equations will be useful in many other designs.

Based on this research, one paper [49] has been published in the International Journal of RF and Microwave Computer-Aided Engineering and another paper [50] is to appear.

6.2 Future work

Some suggestions for improving the microwave filter design using 2-D and 3-D commercial simulators are:

- To build a accurate coupling database for the new design of the slab-line filter as shown in Figure 5.5. The position and diameter of the air hole will be changed to obtain the optimum results.

- To generate a more accurate database that includes the higher order mode effects of adjacent K- and J-inverters. This will also make the approach viable for iris and septum coupled bandpass filter designs.
- To design the bandpass waveguide filters with other waveguide structures, such as three round rod coupled waveguide and two asymmetrical round rod coupled waveguide.
- To design the triplexers and other multiplexers using the same approach as in the Section 5.2.2.
- To develop simulation methods that are more powerful, more accurate, easier to use and less expensive.

LIST OF REFERENCES

[1] E. G. Cristal, "*Coupled Circular Cylindrical Rods between Parallel Ground Planes*," IEEE Trans. On MTT, Vol. 12, pp. 428-439, July 1964.

[2] Bharathi Bhat, and Shiban K. Koul, *Stripline-Like Transmission Lines for Microwave Integrated Circuits*, John Wiley & Sons, New Delhi, India, 1989.

[3] R. E. Collin, *Field Theory of Guided Waves*, IEEE Press, NY, 1992.

[4] G. Matthaei, L. Young and E. M. T. Jones, *Microwave Filters, Impedance Matching Networks and Coupled Structures*, Artech House, Norwood, MA, 1992.

[5] I. Bahl, and P. Bhartia, *Microwave Solid State Circuit Design*. John Willy and Sons, 1988.

[6] *Micro-Stripes User's Manual*, Kimberley Communications Consultants Ltd., Nottingham, UK, 1996.

[7] *FullWave Getting Started Guide*, Infolytica Corporation, Montreal, Canada, 1998.

[8] *PDEase Reference Manual*, SPDE Inc., Bass Lake, CA, USA, 1997.

[9] N. Marcuvitz, Ed., *Waveguide Handbook*, McGraw-Hill, New York, 1951; also Peregrinus, London, 1985.

[10] L. Lewin, *Theory of Waveguides*, Newnes-Butterworth, London, 1975.

[11] Robert E. Collin, *Foundations for Microwave Engineering*, McGraw-Hill, Inc., 1996.

[12] T. Koryu Ishii, *Handbook of Microwave Technology*, Academic Press, CA, 1995.

[13] S. Darlington, "Synthesis of reactance 4-poles," J. Math. Phys., vol. 18, pp. 257-353, Sept. 1939.

[14] A. I. Zverev, *Handbook of Filter Synthesis*, John Wiley & Sons, New York, 1967.

[15] A. B. Williams, and F. J. Taylor, *Electronic Filter Design Handbook: LC, Active, and Digital Filters*, McGraw-Hill, New York, 1988.

[16] W. P. Mason and R. A. Sykes, "The use of coaxial and balanced transmission lines in filters and wide band transformers for high radio frequencies," Bell Syst. Tech. J., vol. 16, pp. 275-302, 1937.

[17] *Microwave Transmission Circuits*, M.I.T. Rad Lab. Series, vol. 9, G. L. Ragan, Ed. New York: McGraw Hill, 1948. See Chapters 9 and 10 by R. M. Fano and A. W. Lawson.

[18] H. J. Orchard, "Formulas for ladder filters," Wireless Engineer, vol. 30, pp. 3-5, Jan. 1953.

[19] E. Green, "Synthesis of ladder networks to give Butterworth or Chebyshev response in the passband," Proc. IEE, vol. 101 IV, monograph no. 88, 1954.

[20] S. B. Cohn, "Direct-coupled-resonator filters," Proc. IRE, vol. 45, pp. 187-196, Feb. 1957.

[21] J. Uher, J. Bornemann and U. Rosenberg, *Waveguide Components for Antenna Feed Systems: Theory and CAD*, Artechc House, Norwood , MA, 1995.

[22] *EMPIRE, FDTD based software*, IMST, Kamp-Lintfort, Germany, 1998.

[23] *HFSS, Finite Element Method based software*, Hewlett and Packard, Palo Alto, CA., 1997.

[24] *SONNET, Moment Method based software*, Sonnet Software Inc. Liverpool, NY, USA, 1998.

[25] *EMSIGHT, Moment Method based software*, Applied Wave Research, Inc. Redondo Beach, CA, 1998.

[26] *MOMENTUM*, Hewlett and Packard, Palo Alto, CA, 1998.

[27] Matthew N. O. Sadiku, *Numerical Techniques in Electromagnetics*, CRC Press, 1992.

[28] D. T. Paris and F.K. Hurd, *Basic Electromagnetic Theory*, McGraw-Hill, New York, 1969, p. 166.

[29] P. P. Silvester and R. L. Ferrai, *Finite Elements for Electrical Engineers*, Cambridge University Press, New York, 1983.

[30] C. W. Steele, *Numerical Computation of Electric and Magnetic Fields*, Van Nostrand Reinhold, New York, 1987.

[31] A. J. Davies, *The Finite Element Method: A First Approach*, Oxford University Press, Oxford, 1980.

[32] W. B. Bickford, *A First Course in the Finite Element Method*, Richard D. Irwin, Homewood, 1990.

[33] O. W. Andersen, "Laplacian Electrostatic Field Calculations by Finite Elements with Automatic Grid Generation," IEEE Trans. Power App. Syst., vol. PAS-92, no. 5, Sept./Oct. 1973, pp. 1485-1492.

[34] W. J. R. Hoefer, "The Transmission-line Matrix Method – theory and applications," IEEE Trans. Microwave Theory Tech., vol. MTT-33, No. 10, Oct. 1985, pp. 882-893.

[35] N. Marcovitz and J. Schwinger, "On the Reproduction of the Electric and Magnetic fields produced by Currents and Discontinuities in Wave Guides, I," J. Appl. Phys., vol. 22, no. 6, June 1951, pp. 806-819.

[36] M. N. O. Sadiku and L. C. Agba, "A simple introdution to the transmission-line modeling," IEEE Trans. Circ. Sys., vol. CAS-37, no. 8, Aug. 1990, pp. 991-999.

[37] B. J. Ley, *Computer Aided Analysis and Design for Electrical Engineers*, New York: Holt, Rinehart and Winston, 1970, pp. 815-817.

[38] P. B. Johns and R. L. Beurle, "Numerical Solution of 2-dimensional Scattering Problems Using a Transmission Line Matrix," Proc. IEEE, vol. 118, no. 9, Sept. 1971, pp. 1203-1208.

[39] G. E. Marike and G. Yek, "Dynamic Three-dimensional T. L. M. Analysis of Microstrip Lines on Anisotropic Substrate," IEEE Trans. Micro. Theo. Tech., vol. MTT-33, no. 9, Sept. 1985, pp. 789-799.

[40] J. D. Rhodes, *Theory of Electric Filters*, John Wiley & Sons, New York, 1976.

[41] Atsushi Fukasawa, "Analysis and Composition of a New Microwave Filter Configuration with Inhomogeneous Dielectric Medium," IEEE Trans. on MTT, vol. MTT-30, No. 9, Sept. 1982, pp. 1367-1375.

[42] S. B. Cohn, "Dissipation Loss in Multi-Coupled Resonator Filters," Proc. IRE, Vol. 47, 1957, pp. 1342-1348.

[43] R. Levy, "Theory of direct coupled cavity filters," IEEE Trans. on MTT, Vol.15, No. 6, June, 1967, pp.340-348.

[44] R. Levy, "Tapered Corrugated Waveguide Low-Pass Filters," IEEE Trans. Microwave Theory Tech., MTT-21, Aug., 1973, pp. 525-532.

[45] R. Levy, "Tables of Element Values for the Distributed Low-Pass Prototype Filters," IEEE Trans. Microwave Theory Tech., MTT -13, June 1965, pp.514-536.

[46] T. Itoh, *Numerical Techniques in Microwave and Millimeter Wave Integrated Circuits*, John Wiley & Sons, New York, 1990.

[47] J. T. Bolljahn, G. L. Matthaei, "A Study of the Phase and Filter Properties of Arrays of Parallel Conductors between Ground Planes," Proc. IRE, vol. 50, 1962, pp. 299-311.

[48] *TableCurve 2D*, Jandel Scientific, San Rafael, CA, USA, 1994.

[49] Shi Yin, Tatyana Vasilyeva, Protap Pramanick, "Use of Three-Dimensional Field Simulators in the Synthesis of Waveguide Round Rod Bandpass Filters," International Journal of RF and Microwave Computer-Aided Engineering, vol. 8, Nov. 1998, pp. 484-497.

[50] Shi Yin, Protap Pramanick, "Use of 3-D Field Simulators in the Synthesis of Waveguide Capacitive Iris Coupled Lowpass Filters," International Journal of RF and Microwave Computer-Aided Engineering, to appear.

APPENDIX A

A.1 One rod filter with constant diameter

A.1.1 *h/a - K*

$$y = \frac{A + C\ln z + E(\ln z)^2}{1 + B\ln z + D(\ln z)^2 + F(\ln z)^3},$$

Where y is h/a and z is K.

$$A = a_1 + b_1 \ln x + c_1(\ln x)^2 + d_1(\ln x)^3 + e_1(\ln x)^4 + f_1(\ln x)^5 + g_1(\ln x)^6 + h_1(\ln x)^7 + i_1(\ln x)^8 + j_1(\ln x)^9 + k_1(\ln x)^{10},$$

$$B = a_2 + b_2 \ln x + c_2(\ln x)^2 + d_2(\ln x)^3 + e_2(\ln x)^4 + f_2(\ln x)^5 + g_2(\ln x)^6 + h_2(\ln x)^7 + i_2(\ln x)^8 + j_2(\ln x)^9 + k_2(\ln x)^{10},$$

$$C = a_3 + b_3 \ln x + c_3(\ln x)^2 + d_3(\ln x)^3 + e_3(\ln x)^4 + f_3(\ln x)^5 + g_3(\ln x)^6 + h_3(\ln x)^7 + i_3(\ln x)^8 + j_3(\ln x)^9 + k_3(\ln x)^{10},$$

$$D = a_4 + b_4 \ln x + c_4(\ln x)^2 + d_4(\ln x)^3 + e_4(\ln x)^4 + f_4(\ln x)^5 + g_4(\ln x)^6 + h_4(\ln x)^7 + i_4(\ln x)^8 + j_4(\ln x)^9 + k_4(\ln x)^{10},$$

$$E = a_5 + b_5 \ln x + c_5(\ln x)^2 + d_5(\ln x)^3 + e_5(\ln x)^4 + f_5(\ln x)^5 + g_5(\ln x)^6 + h_5(\ln x)^7 + i_5(\ln x)^8 + j_5(\ln x)^9 + k_5(\ln x)^{10},$$

$$F = a_6 + b_6 \ln x + c_6(\ln x)^2 + d_6(\ln x)^3 + e_6(\ln x)^4 + f_6(\ln x)^5 + g_6(\ln x)^6 + h_6(\ln x)^7 + i_6(\ln x)^8 + j_6(\ln x)^9 + k_6(\ln x)^{10},$$

where x is f / f_c. See Table A.1.

Table A.1 Parameters in h/a - K equations

Subscript	1	2	3	4	5	6
a_n	0.8485451	11.6214354	3.891231	4.9587681	1.1474282	0.4409815
b_n	-18.000752	-249.18609	-86.1731	-108.8605	-25.37332	-9.7305548
c_n	144.2407	2097.05354	716.15405	922.31628	212.62514	82.931162
d_n	-560.44832	-8585.1268	-2902.559	-3792.888	-867.4972	-342.13826
e_n	1029.453	16537.9386	5542.8546	7335.2958	1666.6244	663.41604
f_n	-496.9176	-8635.3066	-2853.428	-3853.848	-866.6972	-349.73506
g_n	-781.4187	-12720.911	-4255.766	-5645.917	-1280.996	-510.83452
h_n	283.41137	5138.72283	1680.4717	2303.8776	514.25474	209.58179
i_n	924.34065	15517.1877	5154.4783	6906.7983	1558.4913	626.00086
j_n	365.18654	5843.53581	1959.2622	2584.4565	585.80549	233.75038
k_n	-1053.0809	-18001.498	-5961.234	-8037.479	-1812.832	-728.92553

A.1.2 Phase ϕ - h/a

$$y = A + Bz + Cz^2 + Dz^3 + Ez^4 + Fz^5 + Gz^6,$$

where y is ϕ and z is h/a.

$$A = a_1 + b_1 x + \frac{c_1}{x} + d_1 x^2 + \frac{e_1}{x^2} + f_1 x^3 + \frac{g_1}{x^3} + h_1 x^4 + \frac{i_1}{x^4} + j_1 x^5,$$

$$B = a_2 + b_2 x + \frac{c_2}{x} + d_2 x^2 + \frac{e_2}{x^2} + f_2 x^3 + \frac{g_2}{x^3} + h_2 x^4 + \frac{i_2}{x^4} + j_2 x^5,$$

$$C = a_3 + b_3 x + \frac{c_3}{x} + d_3 x^2 + \frac{e_3}{x^2} + f_3 x^3 + \frac{g_3}{x^3} + h_3 x^4 + \frac{i_3}{x^4} + j_3 x^5,$$

$$D = a_4 + b_4 x + \frac{c_4}{x} + d_4 x^2 + \frac{e_4}{x^2} + f_4 x^3 + \frac{g_4}{x^3} + h_4 x^4 + \frac{i_4}{x^4} + j_4 x^5,$$

$$E = a_5 + b_5 x + \frac{c_5}{x} + d_5 x^2 + \frac{e_5}{x^2} + f_5 x^3 + \frac{g_5}{x^3} + h_5 x^4 + \frac{i_5}{x^4} + j_5 x^5,$$

$$F = a_6 + b_6 x + \frac{c_6}{x} + d_6 x^2 + \frac{e_6}{x^2} + f_6 x^3 + \frac{g_6}{x^3} + h_6 x^4 + \frac{i_6}{x^4} + j_6 x^5,$$

$$G = a_7 + b_7 x + \frac{c_7}{x} + d_7 x^2 + \frac{e_7}{x^2} + f_7 x^3 + \frac{g_7}{x^3} + h_7 x^4 + \frac{i_7}{x^4} + j_7 x^5,$$

where x is f / f_c. See Table A.2.

Table A.2 Parameters in ϕ - h/a equations

Subscript	1	2	3	4	5	6	7
a_n	3371.316	-56097.592	342608.91	-919421.71	853330.7	517141.17	-994921.2
b_n	-4484.802	74914.119	-460083.2	1242975.3	-1163687	-699091.8	1360640.6
c_n	5473.3001	-91273.396	559267.03	-1506857.2	1405873.3	847519.95	-1641978
d_n	-4382.517	72980.317	-446396.4	1200370.6	-1117128.2	-675142	1303688
e_n	-1297.224	21555.672	-131162.4	350117.18	-322532.41	-196955.3	375076.17
f_n	6871.2641	-114866.54	705867.6	-1907880.9	1787024.4	1073079.9	-2089738
g_n	-7079.389	118010.33	-722380.6	1943638.3	-1809918.5	-1093221	2112496.3
h_n	-2982.957	50015.584	-308413.6	836707.04	-787274.17	-470606.6	921952.49
i_n	4089.846	-68161.31	416896.62	-1120305.1	1041374.4	630155.67	-1214708
j_n	440.41793	-7408.8255	45857.006	-124913.32	118121.33	70256.075	-138549

A.2 Double rod filter with constant diameter

A.2.1 d/a - K

$$y = \frac{A + C\ln z + E(\ln z)^2}{1 + B\ln z + D(\ln z)^2 + F(\ln z)^3},$$

where y is d/a and z is K.

$$A = \frac{a_1 + c_1 x + e_1 x^2 + g_1 x^3}{1 + b_1 x + d_1 x^2 + f_1 x^3 + h_1 x^4},$$

$$B = \frac{a_2 + c_2 x + e_2 x^2 + g_2 x^3}{1 + b_2 x + d_2 x^2 + f_2 x^3 + h_2 x^4},$$

$$C = \frac{a_3 + c_3 x + e_3 x^2 + g_3 x^3}{1 + b_3 x + d_3 x^2 + f_3 x^3 + h_3 x^4},$$

$$D = \frac{a_4 + c_4 x + e_4 x^2 + g_4 x^3}{1 + b_4 x + d_4 x^2 + f_4 x^3 + h_4 x^4},$$

$$E = \frac{a_5 + c_5 x + e_5 x^2 + g_5 x^3}{1 + b_5 x + d_5 x^2 + f_5 x^3 + h_5 x^4},$$

$$F = \frac{a_6 + c_6 x + e_6 x^2 + g_6 x^3}{1 + b_6 x + d_6 x^2 + f_6 x^3 + h_6 x^4},$$

where x is f / f_c. See Table A.3.

Table A.3 Parameters in d/a - K equations

Subscript	1	2	3	4	5	6
a_n	2.0451796	-0.0591621	0.4878665	-0.08685	0.0313142	-0.0113595
b_n	-0.2760113	-1.1680638	-1.111949	-1.189865	-0.947577	-0.0042601
c_n	-2.766195	0.29744964	-0.826611	0.1719651	-0.041375	0.0135913
d_n	-1.3815257	-0.2582745	-0.303509	-0.23652	-0.368788	-0.0102162
e_n	0.3672732	-0.3323612	0.3642847	-0.100822	0.0098689	-0.0106391
f_n	0.5735396	0.46306445	0.4945821	0.5003465	0.4701527	-0.0177907
g_n	0.2157775	0.10222825	-0.038665	0.0189386	0.0015968	0.0033689
h_n	0.0098732	-0.0986822	-0.107601	-0.115664	-0.097278	-0.0122064

A.2.2 Phase ϕ - d/a

$$y = A + Bz + Cz^2 + Dz^3 + Ez^4 + Fz^5 + Gz^6,$$

where y is ϕ and z is d/a.

$$A = a_1 + b_1 x + \frac{c_1}{x} + d_1 x^2 + \frac{e_1}{x^2} + f_1 x^3 + \frac{g_1}{x^3} + h_1 x^4 + \frac{i_1}{x^4} + j_1 x^5,$$

$$B = a_2 + b_2 x + \frac{c_2}{x} + d_2 x^2 + \frac{e_2}{x^2} + f_2 x^3 + \frac{g_2}{x^3} + h_2 x^4 + \frac{i_2}{x^4} + j_2 x^5,$$

$$C = a_3 + b_3 x + \frac{c_3}{x} + d_3 x^2 + \frac{e_3}{x^2} + f_3 x^3 + \frac{g_3}{x^3} + h_3 x^4 + \frac{i_3}{x^4} + j_3 x^5,$$

$$D = a_4 + b_4 x + \frac{c_4}{x} + d_4 x^2 + \frac{e_4}{x^2} + f_4 x^3 + \frac{g_4}{x^3} + h_4 x^4 + \frac{i_4}{x^4} + j_4 x^5 ,$$

$$E = a_5 + b_5 x + \frac{c_5}{x} + d_5 x^2 + \frac{e_5}{x^2} + f_5 x^3 + \frac{g_5}{x^3} + h_5 x^4 + \frac{i_5}{x^4} + j_5 x^5 ,$$

$$F = a_6 + b_6 x + \frac{c_6}{x} + d_6 x^2 + \frac{e_6}{x^2} + f_6 x^3 + \frac{g_6}{x^3} + h_6 x^4 + \frac{i_6}{x^4} + j_6 x^5 ,$$

$$G = a_7 + b_7 x + \frac{c_7}{x} + d_7 x^2 + \frac{e_7}{x^2} + f_7 x^3 + \frac{g_7}{x^3} + h_7 x^4 + \frac{i_7}{x^4} + j_7 x^5 ,$$

where x is f / f_c. See Table A.4.

Table A.4 Parameters in ϕ - d/a equations

Subscript	1	2	3	4	5	6
a_n	-16.9797488	174.7064157	-842.8761	2029.9431	-2503.656	1436.1446
b_n	18.65774093	-174.9360363	727.87732	-1336.867	778.09589	561.17776
c_n	-24.8033523	244.6231458	-1095.334	2335.894	-2252.263	564.84407
d_n	21.5573	-216.4179527	1011.5903	-2320.171	2618.7425	-1221.4543
e_n	6.897119043	-71.07678683	369.86173	-982.5025	1396.3241	-1013.4384
f_n	-27.0479628	250.6517436	-1017.557	1762.1506	-731.5841	-1249.2933
g_n	32.61932707	-323.3510177	1488.8647	-3327.78	3560.4457	-1412.2354
h_n	8.870172837	-68.92119827	199.96687	-0.039131	-1015.975	1759.9611
i_n	-19.1126863	185.2706067	-874.5709	2026.8856	-2317.718	1116.6653
j_n	-0.60879237	0.352413736	28.331252	-178.5724	454.79076	-532.79992

A.3 One rod filter with variable diameter:

A.3.1 r/a - K

$$y = A + B\ln z + \frac{C}{\ln z} + D(\ln z)^2 + \frac{E}{(\ln z)^2} + F(\ln z)^3 ,$$

where y is r/a and z is K.

$$A = a_1 + \frac{b_1}{\ln x} + \frac{c_1}{(\ln x)^2} + \frac{d_1}{(\ln x)^3} + \frac{e_1}{(\ln x)^4} + \frac{f_1}{(\ln x)^5},$$

$$B = a_2 + \frac{b_2}{\ln x} + \frac{c_2}{(\ln x)^2} + \frac{d_2}{(\ln x)^3} + \frac{e_2}{(\ln x)^4} + \frac{f_2}{(\ln x)^5},$$

$$C = a_3 + \frac{b_3}{\ln x} + \frac{c_3}{(\ln x)^2} + \frac{d_3}{(\ln x)^3} + \frac{e_3}{(\ln x)^4} + \frac{f_3}{(\ln x)^5},$$

$$D = a_4 + \frac{b_4}{\ln x} + \frac{c_4}{(\ln x)^2} + \frac{d_4}{(\ln x)^3} + \frac{e_4}{(\ln x)^4} + \frac{f_4}{(\ln x)^5},$$

$$E = a_5 + \frac{b_5}{\ln x} + \frac{c_5}{(\ln x)^2} + \frac{d}{(\ln x)^3} + \frac{e_5}{(\ln x)^4} + \frac{f_5}{(\ln x)^5},$$

$$F = a_6 + \frac{b_6}{\ln x} + \frac{c_6}{(\ln x)^2} + \frac{d_6}{(\ln x)^3} + \frac{e_6}{(\ln x)^4} + \frac{f_6}{(\ln x)^5},$$

where x is f / f_c. See Table A.5.

Table A.5 Parameters in r/a - K equations

Subscript	1	2	3	4	5	6
a_n	0.2447249	-0.0742662	0.1886796	-0.02096	0.0414294	-0.0023311
b_n	-0.2870123	0.01028808	-0.191547	0.0179941	-0.042117	0.0024974
c_n	0.1181198	-0.0036029	0.0822641	-0.007815	0.0207812	-0.001138
d_n	-0.0277783	-0.000195	-0.020841	0.0015752	-0.00594	0.0002489
e_n	0.0032802	0.00014159	0.002597	-0.000152	0.0007957	-0.0000264
f_n	-0.0001518	-0.0000113	-0.000125	0.0000056	-0.0000403	0.00000109

A.3.2 Phase ϕ - r/a

$$y = A + Bz + Cz^2 + Dz^3 + Ez^4 + Fz^5 + Gz^6,$$

where y is ϕ and z is r/a.

$$A = a_1 + b_1 x + \frac{c_1}{x} + d_1 x^2 + \frac{e_1}{x^2} + f_1 x^3 + \frac{g_1}{x^3} + h_1 x^4 + \frac{i_1}{x^4} + j_1 x^5 ,$$

$$B = a_2 + b_2 x + \frac{c_2}{x} + d_2 x^2 + \frac{e_2}{x^2} + f_2 x^3 + \frac{g_2}{x^3} + h_2 x^4 + \frac{i_2}{x^4} + j_2 x^5 ,$$

$$C = a_3 + b_3 x + \frac{c_3}{x} + d_3 x^2 + \frac{e_3}{x^2} + f_3 x^3 + \frac{g_3}{x^3} + h_3 x^4 + \frac{i_3}{x^4} + j_3 x^5 ,$$

$$D = a_4 + b_4 x + \frac{c_4}{x} + d_4 x^2 + \frac{e_4}{x^2} + f_4 x^3 + \frac{g_4}{x^3} + h_4 x^4 + \frac{i_4}{x^4} + j_4 x^5 ,$$

$$E = a_5 + b_5 x + \frac{c_5}{x} + d_5 x^2 + \frac{e_5}{x^2} + f_5 x^3 + \frac{g_5}{x^3} + h_5 x^4 + \frac{i_5}{x^4} + j_5 x^5 ,$$

$$F = a_6 + b_6 x + \frac{c_6}{x} + d_6 x^2 + \frac{e_6}{x^2} + f_6 x^3 + \frac{g_6}{x^3} + h_6 x^4 + \frac{i_6}{x^4} + j_6 x^5 ,$$

$$G = a_7 + b_7 x + \frac{c_7}{x} + d_7 x^2 + \frac{e_7}{x^2} + f_7 x^3 + \frac{g_7}{x^3} + h_7 x^4 + \frac{i_7}{x^4} + j_7 x^5 ,$$

where x is f / f_c. See Table A.6.

Table A.6 Parameters in ϕ - r/a equations

subscript	1	2	3	4	5	6	7
a_n	-5.110218	269.62985	-5114.286	40156.08	-132811.7	154001.36	219700.02
b_n	10.03031	-474.21337	8555.9757	-66050.905	216276.59	-238895.5	-345494.8
c_n	-10.95823	530.47506	-9680.056	75067.135	-246485.21	276671.14	398306.57
d_n	7.5658361	-387.17781	7250.784	-56629.031	186716.73	-212462.3	-304690.2
e_n	0.567431	-57.55465	1313.661	-10820.966	36717.24	-46698.45	-64991.2
f_n	-15.56967	727.32606	-13041.8	100561.59	-329027.08	363345.39	525521.03
g_n	12.359701	-624.86493	11635.633	-90804.017	299220.47	-340838.4	-488655.3
h_n	7.5211831	-343.08569	6067.9326	-46547.759	151763.05	-165127.9	-239853.2
i_n	-5.41811	310.18088	-6077.117	48027.133	-159334.68	185155.69	263976.22
j_n	-1.190582	53.686586	-945.5064	7245.5926	-23596.91	25407.113	37016.448

APPENDIX B

B.1 Waveguide ($b/a = 0.5$) filter with irises

B.1.1 w/a - J

$$y = \frac{A + Cz + Ez^2 + Gz^3 + Iz^4}{1 + Bz + Dz^2 + Fz^3 + Hz^4 + Jz^5},$$

where y is w/a and z is J.

$$A = a_1 + b_1 x + c_1 x^2 + d_1 x^3 + e_1 x^4 + f_1 x^5 + g_1 x^6,$$

$$B = a_2 + b_2 x + c_2 x^2 + d_2 x^3 + e_2 x^4 + f_2 x^5 + g_2 x^6,$$

$$C = a_3 + b_3 x + c_3 x^2 + d_3 x^3 + e_3 x^4 + f_3 x^5 + g_3 x^6,$$

$$D = a_4 + b_4 x + c_4 x^2 + d_4 x^3 + e_4 x^4 + f_4 x^5 + g_4 x^6,$$

$$E = a_5 + b_5 x + c_5 x^2 + d_5 x^3 + e_5 x^4 + f_5 x^5 + g_5 x^6,$$

$$F = a_6 + b_6 x + c_6 x^2 + d_6 x^3 + e_6 x^4 + f_6 x^5 + g_6 x^6,$$

$$G = a_7 + b_7 x + c_7 x^2 + d_7 x^3 + e_7 x^4 + f_7 x^5 + g_7 x^6,$$

$$H = a_8 + b_8 x + c_8 x^2 + d_8 x^3 + e_8 x^4 + f_8 x^5 + g_8 x^6,$$

$$I = a_9 + b_9 x + c_9 x^2 + d_9 x^3 + e_9 x^4 + f_9 x^5 + g_9 x^6,$$

$$J = a_{10} + b_{10} x + c_{10} x^2 + d_{10} x^3 + e_{10} x^4 + f_{10} x^5 + g_{10} x^6,$$

where $x = f / f_c$. See Table B.1.

Table B.1 Parameters in w/a - J equations ($b/a = 0.5$)

Subscript	a_n	b_n	c_n	d_n	e_n	f_n	g_n
1	0.05192835	-0.089860091	0.013127602	0.061416224	-0.048345998	0.013725506	-0.001305012
2	-14.71463074	21.86733988	-7.429558066	-16.52894891	18.23285504	-7.038078124	0.968257971
3	-1.164201693	1.745226186	-0.02023812	-1.088747858	0.688154844	-0.148776791	0.007541997
4	35.32742747	-57.22807755	15.69805989	42.68199357	-40.24933283	13.53884912	-1.617200852
5	0.043565745	3.217871258	-3.879651807	-3.206117625	6.307614583	-3.067036615	0.490781698
6	-8.86511736	-6.776031823	20.83890334	6.65156021	-36.06058916	21.61539218	-3.878646490
7	8.214079843	-23.22557455	12.80956645	18.49760403	-25.41617336	10.87740990	-1.606004887
8	-43.4771855	118.5366988	-66.90173141	-91.36327312	138.2034891	-62.63464891	9.653797846
9	-9.89044835	24.51160938	-11.16430924	-18.89354777	23.53550139	-9.540115721	1.348960006
10	24.57254492	-62.60200555	32.82300134	48.10121286	-68.71412435	30.32074410	-4.586122893

B.1.2 Phase ϕ - w/a

$$y = A + Bz + Cz^2 + Dz^3 + Ez^4 + Fz^5 + Gz^6,$$

where y is ϕ and z is w/a.

$$A = a_1 + b_1x + c_1x^2 + d_1x^3 + e_1x^4 + f_1x^5 + g_1x^6,$$

$$B = a_2 + b_2x + c_2x^2 + d_2x^3 + e_2x^4 + f_2x^5 + g_2x^6,$$

$$C = a_3 + b_3x + c_3x^2 + d_3x^3 + e_3x^4 + f_3x^5 + g_3x^6,$$

$$D = a_4 + b_4x + c_4x^2 + d_4x^3 + e_4x^4 + f_4x^5 + g_4x^{6^7},$$

$$E = a_5 + b_5x + c_5x^2 + d_5x^3 + e_5x^4 + f_5x^5 + g_5x^6,$$

$$F = a_6 + b_6x + c_6x^2 + d_6x^3 + e_6x^4 + f_6x^5 + g_6x^6,$$

$$G = a_7 + b_7x + c_7x^2 + d_7x^3 + e_7x^4 + f_7x^5 + g_7x^6,$$

where x is f / f_c. See Table B.2.

Table B.2 Parameters in ϕ - w/a equations ($b/a = 0.5$)

Subscript	a_n	b_n	c_n	d_n	e_n	f_n	g_n
1	4.811219473	-9.819491538	3.197915425	7.153330635	-7.804622880	3.019244854	-0.420155777
2	290.1492988	-390.1064951	-11.13632755	249.4258659	-122.0466568	8.228771911	3.645254234
3	-8079.724583	14699.301	-3366.48691	-10340.90124	9723.087021	-3359.441126	419.0071437
4	60294.46744	-112863.2239	27775.6744	79966.24796	-77046.85469	27094.78759	-3436.7573
5	-208781.4058	388486.2977	-91799.34499	-274580.1487	259163.7356	-89201.79806	11018.9081
6	354537.3628	-648819.8752	141349.8597	455991.3846	-415144.9210	137688.1882	-16226.15136
7	-240101.2729	431059.2811	-85067.33374	-300947.2226	262941.9570	-83365.49552	9229.227079

B.2. Waveguide ($b/a = 0.4444$) filter with irises

B.2.1. w/a - J

$$y = \frac{A + Cz + Ez^2 + Gz^3}{1 + Bz + Dz^2 + Fz^3},$$

where y is w/a and z is J.

$$A = a_1 + b_1 x + c_1 x^2 + d_1 x^3 + e_1 x^4 + f_1 x^5 + g_1 x^6,$$

$$B = a_2 + b_2 x + c_2 x^2 + d_2 x^3 + e_2 x^4 + f_2 x^5 + g_2 x^6,$$

$$C = a_3 + b_3 x + c_3 x^2 + d_3 x^3 + e_3 x^4 + f_3 x^5 + g_3 x^6,$$

$$D = a_4 + b_4 x + c_4 x^2 + d_4 x^3 + e_4 x^4 + f_4 x^5 + g_4 x^{6^7},$$

$$E = a_5 + b_5 x + c_5 x^2 + d_5 x^3 + e_5 x^4 + f_5 x^5 + g_5 x^6,$$

$$F = a_6 + b_6 x + c_6 x^2 + d_6 x^3 + e_6 x^4 + f_6 x^5 + g_6 x^6,$$

$$G = a_7 + b_7 x + c_7 x^2 + d_7 x^3 + e_7 x^4 + f_7 x^5 + g_7 x^6,$$

where x is f / f_c. See Table B.3.

Table B.3 Parameters in w/a - J equations ($b/a = 0.4444$)

Subscript	a_n	b_n	c_n	d_n	e_n	f_n	g_n
1	0.126656649	-0.239913905	0.058725244	0.167617068	-0.166400262	0.061121736	-0.008191976
2	0.273850357	-7.245561427	2.688643691	5.132810062	-5.667859768	2.163030459	-0.295370881
3	-2.030894069	3.482247427	-0.625588869	-2.318089676	2.210098476	-0.800531064	0.106411294
4	-4.674863063	17.075630410	-6.350660860	-12.47502422	13.99328292	-5.370101432	0.735041653
5	3.545024503	-5.734135309	0.795816027	3.713622648	-3.402465847	1.208508201	-0.158155305
6	3.461408702	-9.907453642	3.651877618	7.272358342	-8.219179793	3.199082268	-0.443590786
7	-1.622893600	2.487832554	-0.271082865	-1.580228173	1.409353369	-0.473994192	0.058233928

B.2.2. Phase ϕ - w/a

$$y = \frac{A + Cz + Ez^2 + Gz^3}{1 + Bz + Dz^2 + Fz^3},$$

where y is ϕ and z is w/a.

$$A = a_1 + b_1x + c_1x^2 + d_1x^3 + e_1x^4 + f_1x^5 + g_1x^6,$$

$$B = a_2 + b_2x + c_2x^2 + d_2x^3 + e_2x^4 + f_2x^5 + g_2x^6,$$

$$C = a_3 + b_3x + c_3x^2 + d_3x^3 + e_3x^4 + f_3x^5 + g_3x^6,$$

$$D = a_4 + b_4x + c_4x^2 + d_4x^3 + e_4x^4 + f_4x^5 + g_4x^{67},$$

$$E = a_5 + b_5x + c_5x^2 + d_5x^3 + e_5x^4 + f_5x^5 + g_5x^6,$$

$$F = a_6 + b_6x + c_6x^2 + d_6x^3 + e_6x^4 + f_6x^5 + g_6x^6,$$

$$G = a_7 + b_7x + c_7x^2 + d_7x^3 + e_7x^4 + f_7x^5 + g_7x^6,$$

where x is f / f_c. See Table B.4.

Table B.4 Parameters in ϕ - w/a equations ($b/a = 0.4444$)

Subscript	a_n	b_n	c_n	d_n	e_n	f_n	g_n
1	-1.737765215	3.72786574	-1.208036726	-2.712754914	2.929092041	-1.122807892	0.155006606
2	704.4381983	-1401.323746	421.3903208	1009.521708	-1067.903447	405.7732784	-55.72234852
3	1089.03015	-2143.739601	642.6081687	1544.683068	-1632.522672	620.0566948	-85.12586075
4	-4302.334476	8535.053696	-2578.730461	-6155.436129	6521.114947	-2479.717591	340.6990232
5	-6581.29321	13003.20086	-3923.165062	-9377.888388	9931.842909	-3776.298057	518.8196787
6	7361.584854	-14712.83931	4529.115793	10638.4392	-11346.78103	4331.295986	-596.8077671
7	11140.17989	-22219.31457	6833.141449	16064.30187	-17132.35832	6540.092337	-901.2313607